LUND UNIVERSITY

Charge Transport in Semiconductor Nanowire Quantum Devices: From Single Quantum Dots to Topological Superconductors

Deng, Mingtang

2013

Charge Transport in Semiconductor Nanowire Quantum Devices:

From Single Quantum Dots to Topological Superconductors

MINGTANG DENG

Division of solid state physics|Department of physics|Lund University
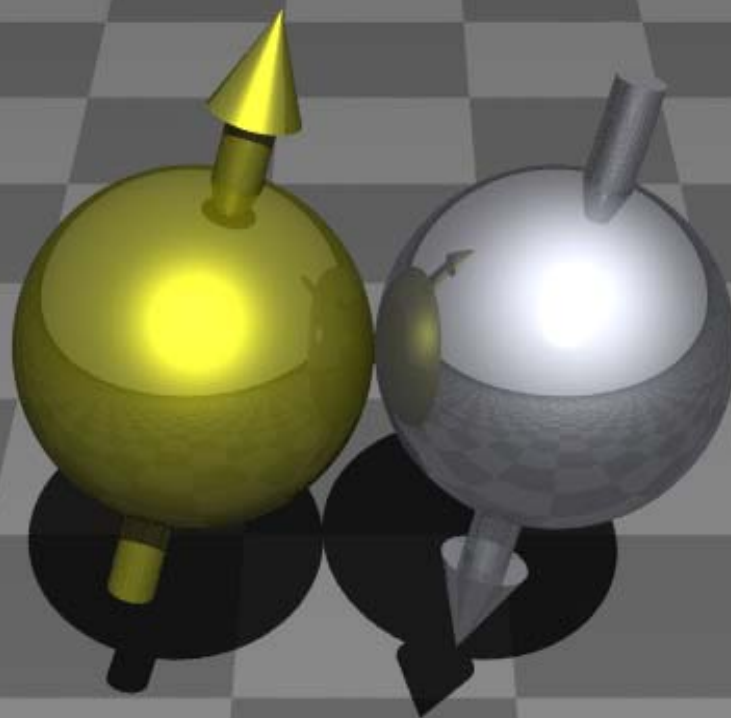
Charge Transport in Semiconductor Nanowire Quantum Devices:

From Single Quantum Dots to Topological Superconductors

Doctoral Thesis

Mingtang Deng

Principal Supervisior
Prof. Hongqi Xu

Faculty Opponent
Prof. Kazuhiko Hirakawa
University of Tokyo
Japan

LUND
UNIVERSITY

Division of Solid State Physics
Deparment of Physics
Lund University
Sweden, 2013

Organization	Document name
Division of solid state physics, **LUND UNIVERSITY**	**DOCTORAL DISSERTATION**
	Date of issue
Author(s) **Mingtang Deng**	Sponsoring organization

Title and subtitle

Charge Transport in Semiconductor Nanowire Quantum Devices:

From Single Quantum Dots to Topological Superconductors

Abstract

This thesis focuses on charge transport in semiconductor InSb nanowire quantum devices, including the electron transport, the hole transport, and the Cooper pair transport. Devices in which InSb semiconductor nanowire quantum dots are coupled with normal metals, superconductors or the proximity effect induced topological superconductors are fabricated and measured.

Firstly, we have fabricated and measured normal metal contacted InSb nanowire devices. In each of these devices, a quantum dot is formed in the InSb nanowire between the contacts. We report on the magnetotransport measurements performed to these quantum dot devices, and reveal several novel transport features. First, we demonstrate the ambipolar quantum dot devices in which the quantum dots can be tuned from the n-type regime to the p-type regime. The transport measurements in both of the n-type regime and the p-type regime are performed. We also show that two methods can be used to estimate the effective g-factor of the quantum dot, but they can give very different estimation in the presence of a Kondo effect. In the p-type regime of an ambipolar quantum dot, we observe conductance peaks in the stability diagram which can be attributed to the quasi-1D lead states.

Secondly, we have fabricated and characterized the superconductor coupled InSb nanowire quantum dots. We probe the density of states of the quasi-particles in the superconductor contacts, via a weakly coupled InSb quantum dot. In the strongly coupled InSb nanowire-superconductor junctions, dissipationless Josephson currents are observed. A SQUIDS device is also fabricated and measured, in which an anomalous modulation of the Josephson current in the magnetic field is observed. In the medium coupling regime, we observe the signatures of the multiple Andreev reflections, the sub-gab bound states, and the Josephson current, interplaying with the Kondo effect. By adjusting the gate voltages, we can control the dot-lead coupling strength and asymmetry. Here, we report the quantum phase transition induced by tuning the dot-lead coupling and the quantum phase transition induced by a magnetic field. We have also found the coupling asymmetry is very important for the observation of the Josephson current. In the magnetic field, the evolution of the Kondo effect enhanced Josephson current is found to be strongly dependent on the energy ratio of Kondo energy and superconducting gap. Finally, an anomalous low-field suppression of the zero-bias conductance peak in the Kondo regime is observed.

In the last part of the thesis, we report on our efforts to search for Majorana fermions in solid state systems. Nb-InSb nanowire quantum dot-Nb hybrid devices were fabricated and the transport measurements were performed at low temperatures for these devices. We have observed anomalous zero-bias conductance peaks emerging in finite magnetic fields in the Nb-InSb nanowire quantum dot-Nb hybrid devices as a signature of the Majorana bound states in such hybrid devices. We have also found that the zero-bias conductance peak are independent of the even-odd parity of the quasi-particle number in the quantum dots and are associated with interesting fine structures. As a validation, a Au-InSb nanowire quantum dot-Nb device is fabricated and measured. Here, signatures of Majorana bound states, i.e., the zero-bias conductance peaks in finite magnetic fields are also observed. In addition, we analyze several other mechanisms that can lead to the emergence of zero-bias conductance peaks in finite magnetic fields, and discuss the results in comparison with the signatures of Majorana bound states.

Key words:

Nanowires, Transport, InSb, Quantum dot, the Zeeman effect, the Kondo effect, Cooper pair, the Josephson effect, Proximity effect, SQUID, Multiple Andreev reflection, Andreev bound state, Yu-Shiba-Rusinov state, Majorana bound state

Classification system and/or index terms (if any)

Supplementary bibliographical information:	Language: **English**
ISSN and key title:	ISBN: **978-91-7473-689-2**

Recipient's notes:	Number of pages: **247**	Price:
	Security classification:	

Distribution by (name and address)

I, the undersigned, being the copyright owner of the abstract of the above-mentioned dissertation, hereby grant to all reference sources permission to publish and disseminate the abstract of the above-mentioned dissertation.

Signature_____ Date_2013-09-05__

Charge Transport in Semiconductor Nanowire Quantum Devices:

From Single Quantum Dots to Topological Superconductors

Doctoral Thesis

Mingtang Deng

Division of Solid State Physics
Deparment of Physics
Lund University
Sweden, 2013

In memory of my grandmother, Mrs. Zhang Qiuling (1936-2012).

Abstract

This thesis focuses on charge transport in semiconductor InSb nanowire quantum devices, including the electron transport, the hole transport, and the Cooper pair transport. Devices in which InSb semiconductor nanowire quantum dots are coupled with normal metals, superconductors or the proximity effect induced topological superconductors are fabricated and measured in a dilution refrigerator.

Firstly, we have fabricated and measured normal metal contacted InSb nanowire devices. In each of these devices, a quantum dot is formed in the InSb nanowire between the contacts. We report on the magnetotransport measurements performed to these quantum dot devices, and reveal several novel transport features. First, we demonstrate two ambipolar InSb nanowire quantum dot devices. In each of the ambipolar devices, the quantum dot can be tuned from an n-type regime to a p-type regime. The transport measurements in both of the n-type regime and the p-type regime are performed. We also show that two methods can be used to estimate the effective g-factor of the quantum dot, but they can give very different estimations in the presence of a Kondo effect. In the p-type regime of an ambipolar quantum dot, we observe conductance peaks in the stability diagram which can be attributed to the quasi-1D lead states.

Secondly, we have fabricated and characterized the superconductor coupled InSb nanowire quantum dots. We probe the density of states of the quasi-particles in the superconductors contacts, via a weakly coupled InSb quantum dot. In the strongly coupled InSb nanowire-superconductor junctions, dissipationless Josephson currents are observed. A SQUIDS device is also fabricated and measured, in which an anomalous modulation of the Josephson current in the magnetic field is observed. In the medium coupling regime, we observe the signatures of the multiple Andreev reflections, the sub-gab bound states, and the Josephson current, interplaying with the Kondo effect. By adjusting the voltages that are applied to the back gate and the side gates of the device, we can control the dot-lead coupling strength and the coupling asymmetry. Here, we report the quantum phase transition induced by tuning the dot-lead coupling and the quantum phase

current is found to be strongly dependent on the energy ratio of $T_K/\Delta(B)$. Finally, an anomalous low-field suppression of the zero-bias conductance peak in the Kondo regime is observed.

In the last part of the thesis, we report on our efforts to search for Majorana fermions in solid state systems. Nb-InSb nanowire quantum dot-Nb hybrid devices were fabricated and the transport measurements were performed at low temperatures for these devices. Due to the proximity effect, the InSb nanowire segments covered by the superconductor Nb contacts become superconductors at low temperatures. Under an applied magnetic field of a sufficient strength, the proximity effect induced superconducting InSb nanowire segments turn to topological superconductors in which Majorana fermion bound states can exist. In our transport measurements, we have observed anomalous zero-bias conductance peaks emerging in finite magnetic fields in the Nb-InSb nanowire quantum dot-Nb hybrid devices–a signature of the Majorana bound states in such hybrid devices. We have also found that the zero-bias conductance peak are independent of the even-odd parity of the quasi-particle number in the quantum dots and are associated with interesting fine structures. As a validation, a Au-InSb nanowire quantum dot-Nb device is fabricated and measured. Here, signatures of Majorana bound states, i.e., the zero-bias conductance peaks in finite magnetic fields are also observed. In addition, we analyze several other mechanisms that can lead to the emergence of zero-bias conductance peaks in finite magnetic fields, and discuss the results in comparison with the signatures of Majorana bound states.

Acknowledgements

In the past four years, the most frequent words I have used were "Hej" and "Thanks". But now, I lack words with which to express my gratitude to those who have been offering me their helps since I came to Lund.

First of all I would like to thank my main supervisor, Prof. Hongqi Xu, for giving me the opportunity to do my PhD in the exciting field. I am grateful for his support and encouragement in my study, research and life in Sweden over the past four years. His enthusiasm and knowledge in the field of electron transport and physics in general have greatly inspired me.

I would like to thank Dr. Ivan Maximov and Dr. Kimberly Dick Thelander for their co-supervising. Thank Ivan for his supports on nano-fabrication technology and sharing his knowledge, and thank Kimberly for the semiconductor material support and the nice summer BBQs.

I would like to express my deepest thanks to Dr. Henrik Nilsson for teaching me everything in this field, from device fabrication, measurement techniques, to cryogenics. His help and guidance were invaluable to me. He and Jennie Borglin also offered me the most wonderful Christmas dinners and friendship. Also the deepest thanks to Dr. Marcus Larsson who helped me a lot on measurement techniques, and Dr. Philippe Caroff who supported me most of the semiconductor materials that I have used during my PhD study.

I would like to thank Dr. Jianing Chen, Dr. Gang Luo, Dr. Fantao Meng, Dr. Jie Sun, and Dr. Claes Thelander for their help on teaching me to use nano-fabrication and electrical measurement equipments.

I am grateful to all of my colleagues in the division. Thanks to Dr. Nicklas Anttu and Guang-Yao Huang for accompanying in the late nights. Thanks to Magnus Heurlin, Dr. Kenichi Kawaguchi, and Dr. Kristian Storm for creating a friendly office environment. Thanks to Daniel Jacobsson, Mercy Lard, Gustav Nylund, and other happy skiers for the exciting skiing journey in France. Thanks to Anil Dey, David Lindgren, Kilian Mergenthaler, Neimantas Vainorius, and other FTF innebandy players, for the weekly innebandy playing. Thanks to Dr. Zhaoxia Bi, Sofia F. Svensson, Richard

List of Papers

I. InSb nanowire field-effect transistors and quantum-dot devices
H.A. Nilsson, **M.T. Deng**, P. Caroff, C. Thelander, L. Samuelson, L-E Wernersson, H.Q. Xu
IEEE Journal of Selected Topics in Quantum Electronics 2011, **17(4)**, pp: 907-914;
I participated in the device fabrication, measurements and data analysis.

II. Anomalous zero-bias peak in a Nb-InSb nanowire-Nb hybrid device
M.T. Deng, C.L. Yu, G.Y. Huang, M. Larsson, P. Caroff, and H.Q. Xu
Nano Letters, 2012, **12 (12)**, pp: 6414-6419;
I led and participated the device fabrication, performed the measurements, and data analysis, and participated in the physics model developing and manuscript writing.

III. Parity independence of the anomalous zero-bias conductance peak in a superconductor-coupled nanowire quantum device
M. T. Deng, C. L. Yu, G. Y. Huang, M. Larsson, P. Caroff, and H. Q. Xu
Manuscript to be submitted, 2013
I performed the measurements and data analysis, led and participated in the device fabrication, physics model developing, and manuscript writing.

IV. Superconductor-Nanowire Devices from Tunneling to the Multichannel Regime: Zero-Bias Oscillations and Magnetoconductance Crossover
H. O. H. Churchill, V. Fatemi, K. Grove-Rasmussen, **M. T. Deng**, P. Caroff, H. Q. Xu, C. M. Marcus
Physical Review B **87**, 241401(r), 2013
I participated in the device fabrication and the discussion of manuscript.

V. Ambipolar InSb nanowire quantum dot devices with superconductor contacts

M.T. Deng, H.A. Nilsson, P. Caroff, and H.Q. Xu
Manuscript to be submitted, 2013.
I fabricated the devices, performed the measurements and data analysis, did the simulation, and participated in manuscript writing.

VI. Low-field suppression of Cooper pair cotunneling in Josephson quantum dots with Kondo effect
M.T. Deng, H.A. Nilsson, C.L. Yu, K.D. Kimberly, P. Caroff, and H.Q. Xu
Manuscript in process, 2013.
I fabricated the devices, performed the measurements and data analysis, wrote the manuscript, and participated in the physics model developing.

Contents

1

Introduction

Electrons in a vacuum space can move freely without any constraint or scattering, and they can take on continuous values of energy. However, the electron in an atom is bounded to the positively charged atom nucleus, and can only take on certain discrete values of energy. In some of the macroscopic solid state objects with crystal structures at micro level (e.g., metals), the valence electron, i.e., the electron that is unbounded or less bounded by the nuclei, can move in a periodic lattice potential. Under the assumption of the effective mass, it behaves like a free electron in the vacuum but with an effective electron mass m^* that is different from the electron rest mass m_e. In this free electron model, the density of states of the valence electrons in bulk materials, as a function of the energy E, is given by Eq. 1.1 (1). The distribution of the density of states of bulk materials is illustrated in Fig. 1.1 (a).

$$\begin{cases} n_{3D}\left(E\right) = \frac{m^*\sqrt{2m^*E}}{\pi^2\hbar^3} & (1) \\ n_{2D}\left(E\right) = \frac{m^*}{\pi\hbar^2} & (2) \\ n_{1D}\left(E\right) = \frac{1}{\pi\hbar}\sqrt{\frac{2m^*}{E}} & (3) \end{cases} \qquad (1.1)$$

The electron density of states will be modified in low-dimensional solid systems, due to the fact that the motion of the electron is quantized on at least one of the dimensions. Equations 1.1 (2) and (3) give the density of states of a 2D and a 1D solid systems, corresponding to Figs. 1.1 (b) and (c), respectively. With all the three dimensions get constrained, electrons in a 0D object can only occupy discrete energy levels, shown as in Fig. 1.1 (d). In this case, this 0D object is an analogue of an atom, and therefore is referred to as an artificial atom or a
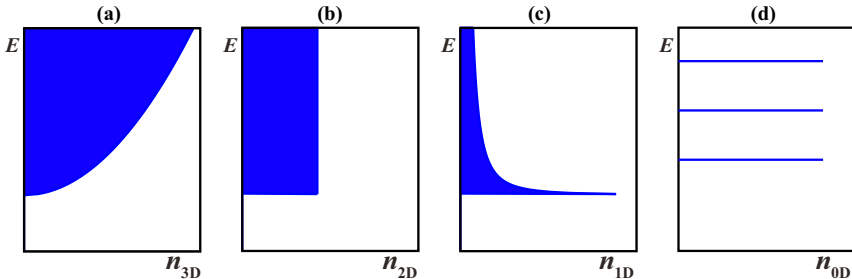
Figure 1.1: (a) The density of states (DOS) (n_{3D}) of a 3D object as a function of particle energy E. (b) DOS (n_{2D}) of a 2D object as a function of particle energy E. (c) DOS (n_{1D}) of a 1D object as a function of particle energy E. (d) DOS (n_{0D}) of a 0D object as a function of particle energy E.

quantum dot (1, 2).

The quantum dot supplies us a useful platform to study the electron behavior in a mesoscopic scale. Besides, it is also a promising candidate of the basic computing unit for the next generation computers. To explain why and how the quantum dot can be used as a new type of computing unit, we give a brief overview on the development of the modern transistor.

The rapid development of transistor revolutionized our society and daily lives because it is the fundamental building block of electronic devices, such as computers and mobile phones. The development of the semiconductor device fabrication technology has been remaining the down-scaling of the transistor size for last 50 years. As we know, the down-scaling of the transistor is well described by the so-called Moore's law, which points out that the density of transistors on integrated circuits doubles approximately every two years (3). This allows more and more transistors are assembled in a single chip. In 2012, the typical half-pitch for a transistor was down-scaled to a remarkable 22 nanometers (1 nanometer $= 10^{-9}$ m) and one single CPU contained 5 billion transistors. However, the down-scaling cannot continue forever. When the transistor size approaches the wavelength of the electrons in the material, quantum properties arise and thereby degrade transistor performance. Besides, the increasing of the transistor density exacerbates the power consumption and the over-heating problems.

To solve the problems mentioned above, researchers are now trying manufacturing electronic components at nanoscale that can take advantage of new phys-

ical principles exploiting the quantum properties rather than being constrained by them. As we mentioned, quantum dots, especially semiconductor quantum dots, are promising candidates among these new electronic components because they exhibit distinct quantum properties.

Firstly, the semiconductor quantum dot is an implication of the single electron transistor (SET), which allows electrons go through the device one by one in the form of tunneling (4). The SET is thereby very promising for solving the overheating and power consumption problems.

Second, the quantum dot is a strong candidate for the realization of the quantum bit (i.e., the qubit), which is the basic unit of the so-called quantum computer (5). Quantum computers can theoretically be used to solve certain types of problems significantly faster than today's classical computers. The spins of electrons on the discrete energy levels of a quantum dot can be used as the basic information storing and operation units, and they are therefore called the spin qubit. Besides, if the quantum dot is contacted by two superconductors, a Josephson junction is formed. The Josephson junction is also a powerful platform for quantum computing, in which the qubit can be realized in the form of a charge qubit or a flux qubit (6), or Andreev bound states based qubit (7). Moreover, when the superconductors in the Josephson quantum dot are p-wave superconductors, the system becomes a topological quantum computing platform, which is intrinsically immune to local noise from which other quantum computing systems suffer a lot (8, 9).

The InSb semiconductor nanowire that we used in this thesis is a promising material to make a quantum dot. The high electron mobility of InSb makes it an ideal SET material, and we can also take the advantage of its narrow band gap to make ambipolar SET circuits. Besides, the unique properties of InSb nanowire make it a perfect component of quantum computing system. It has large spin-orbit interaction, which is favored by the spin qubit system. It shows good coupling to superconductors and can be used to fabricate high quality Josephson junctions for superconducting quantum computation system. Moreover, a superconductor coupled InSb nanowire could host Majorana fermion states when the system is exposed to a magnetic field of a moderate strength. Majorana fermion is an exotic type of particle which is its own antiparticle. The Majorana fermionic bound state in solid state system is crucial for building topological quantum computer.

Therefore, a comprehensive understanding about the charge transport through an InSb nanowire quantum dot is necessary and critical. In this thesis, we have explored the charge (including electrons, holes, and Cooper pairs) transport phenomena in normal metal coupled quantum dots, superconductor coupled quantum dots, and the quantum dots coupled by induced topological superconductors.

This thesis is organized as follows:

Chapter 2 gives a description of the growth of the materials that are used in this thesis, and the fabrication processes of the measurement substrates and InSb nanowire devices.

Chapter 3 gives an introduction to the electron transport model in a single quantum dot, including sequential tunneling process, elastic/inelastic cotunneling process, the Zeeman effect and the Kondo effect. We have discussed the measurements performed to the ambipolar InSb quantum dot devices and based on a simple theoretical model. We also show that two methods can be used to estimate the effective g-factor of the quantum dot, but they can give very different estimations in the presence of a Kondo effect. In the p-type region of an ambipolar quantum dot, we observe conductance peaks in the stability diagram which can be attributed to the quasi-1D leads states. These measurements are based on Papers I and V.

Chapter 4 gives a brief introduction to the superconductivity and the Josephson effect in InSb nanowire based junctions. We have studied the probing of the density of states of the quasi-particles in the superconductors contacts, via a weakly coupled InSb quantum dot. We then comes to a strong coupling regime, where dissipationless Josephson currents through the InSb nanowire-superconductor junctions are observed. A SQUIDS device is also fabricated and measured, in which an anomalous modulation of the Josephson current in the magnetic field is observed. We then discussed the transport in the medium coupling regime. We discussed the signatures of the multiple Andreev reflections, the sub-gab bound states, and the Josephson current, interplaying with the Kondo effects. By adjusting the voltages that are applied to the back gate and the side gates of the device, we can control the dot-lead coupling strength and the coupling asymmetry. We report the quantum phase transition induced by tuning the dot-lead coupling and the quantum phase transition induced by a magnetic field. We also found the coupling asymmetry is very important for the observation of the Josephson current. In the magnetic field, the evolution of the Kondo effect

enhanced Josephson current is found strongly dependent on the energy ratio of $T_K/\Delta(B)$. Finally, an anomalous low-field suppression of the zero-bias conductance peak in the Kondo regime of the Josephson quantum dot is discussed. The measurements discussed in this chapter are based on Papers V and VI.

Chapter 5 gives an introduction of Majorana bound states in solid state systems and reports the observation of the anomalous zero-bias conductance peaks emerging in finite magnetic fields in the InSb nanowire-superconductor hybrid devices, as a signature of the Majorana bound states. The zero-bias conductance peak is found to be independent of the even-odd parity of the quasi-particle number in the quantum dot. In addition, we analyze several other mechanisms that can lead to the emergence of zero-bias conductance peaks in finite magnetic fields, in comparison with the signature of the Majorana bound states. The measurements discussed in this chapter are based on Papers II, III, and IV.

1. INTRODUCTION

2

Material Growth and Device Fabrication

In this chapter, the methods of material growth, the fabrication process of low temperature measurement substrates, and the fabrication of electric contacts to nanowires are described.

2.1 III-V semiconductor nanowire self-assemble methods

All the samples discussed in this thesis were made from self-assembled indium antimonide (InSb) and indium arsenide (InAs) heterostructure nanowires [Fig. 2.1 (a)]. The growth of semiconductor nanowires starts by depositing catalyst seeds on a growth substrate. For InSb/InAs heterostructure nanowires, catalyst seeds are nanoscale gold particles ($20 \sim 80$ nm of diameters), and the growth substrate is an InAs or indium phosphide (InP) semiconductor substrate. In a closed growth environment, appropriate source materials are added to the surface of the growth substrate. If the conditions are suitable, the Au particles will act as local catalysts for crystal growth, and nanowires begin to grow on the surface of the substrate. The InSb/InAs heterostructure nanowires can be grown by two different epitaxy methods. One is the metal-organic vapor phase epitaxy (MOVPE) (10, 11) and the other is the molecular beam epitaxy (MBE) (12).

In the MOVPE growth method, the InAs/InSb nanowire heterostructures were grown on InAs(111)B or InP(111)B substrates decorated with small gold aerosol particles. The growth was performed in a two-stage process. First, the InAs segment was grown by adding trimethylindium (TMIn) and arsine into the

MOVPE reactor. After the growth of a segment of InAs stems, the arsine was then switched off and trimethylantimony (TMSb) was switched on to grow the InSb segment. The growth was terminated by shutting off the TMIn and TMSb sources simultaneously, and cooling down was performed under hydrogen flow only. Both segments were grown at 460 °C for a few minutes each. Differing from the MOVPE method, MBE growth has to be performed in a ultra-high vacuum chamber. However, the gold seed-assisted wire-on-wire growth process is fundamentally analogous to MOVPE growth.

Figure 2.1(b) shows a scanning electron microscope (SEM) image of MOVPE grown InSb/InAs heterostructure nanowires, while Fig. 2.1(c) shows an SEM image of MBE grown InSb/InAs nanowires. In both growth processes, the InAs segments are pure wurtzite structure, and InSb segments have pure zinc blende structure. Contrary to most other III-V nanowires, the InSb nanowire segments are free of any extended structural defects and do not show any tapering [Fig. 2.1(d)].

The growth of the InSb/InAs heterostructure nanowires using MOVPE was performed by Dr. Philippe Caroff and Dr. Kimberly. D. Thelander. All the MBE growth of the InSb/InAs heterostructure nanowires was performed by Dr. Philippe Caroff.

2.2 Device fabrication

2.2.1 Fabrication of substrates for low-temperature measurements

Nanowires are grown on their growth substrates. However, the growth substrates are not suitable for fabricating or measuring devices. Sample fabrications and measurements have to be performed on other substrates according to different experimental requirements. In this thesis, we need to measure electric properties of samples at an ultra-low temperature and therefore substrates for low temperature measurement are essential.

The low temperature measurement substrates were made from a degenerately-doped (n-type) silicon wafer [Fig.2.2(a)]. The wafer was first dry-oxidized to form 90∼120 nm thick SiO_2 layers on the top (the polished side) and the bottom (the unpolished side) surfaces. The polished side of the wafer was then spin-coated with a thin layer of S-1813 optical resist at a spinning speed of 3000 revolutions per minute (RPM) for 60 seconds. Subsequently, the wafer was baked on a hotplate at 180°C for 3 minutes. To remove the unintended resist on the bottom
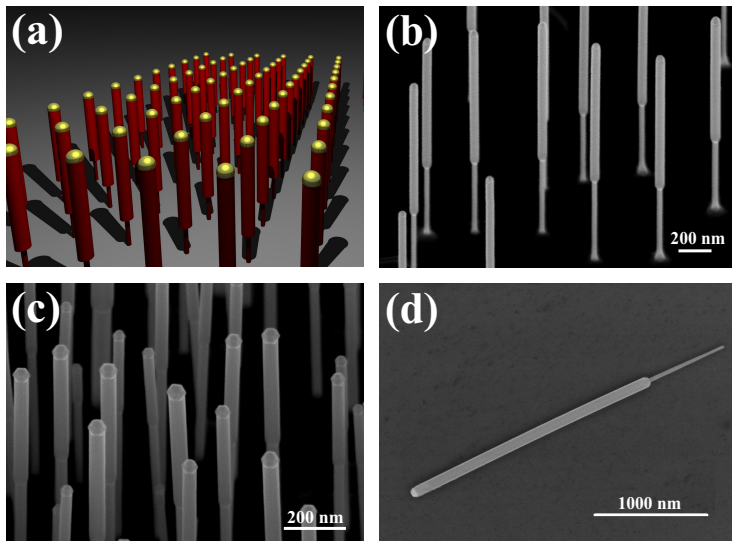
Figure 2.1: Self-assembled InSb/InAs heterostructure nanowires. (a) Schematic of self as-sembled InSb/InAs heterostructure nanowires arrays. The catalytic gold seed is illustrated by the golden-colored particle on the top of each nanowire. (b) SEM image of InSb/InAs heterostructure nanowires arrays grown by MOVPE. (c) SEM image of InSb/InAs het-erostructure nanowires arrays grown by MBE. (d) SEM image of a single InSb/InAs het-erostructure nanowire on a silicon chip. Panels (b) and (c) are reproduced by courtesy of Dr. Philippe Caroff.

surface, it was carefully cleaned by using a clean room tissue rinsed with acetone, followed by a 2-minute oxygen plasma ashing. After that, hydrofluoric acid (HF) was applied on the backside of the wafer to etch away the SiO_2 layer, followed by rinsing the wafer in deionized water and drying in a N_2 flow. Then 50 Å Ti and 1000 Å Au were evaporated by utilizing the physical vapor deposition (PVD) on the backside of the wafer and the wafer was washed in hot acetone to remove the S-1813 on the polished side. Afterwards, the wafer was cleaned in acetone for 3 minutes and isopropanol (IPA) for 3 minutes, all in an ultrasonic bath. Finally, the wafer was dried in a N_2 flow.

We need to provide a coordinate system and alignment markers for the wafer [Fig.2.2(b)]. Firstly, the wafer was spin-coated with ZEP 520 A7 electron-beam sensitive resist at a spinning speed of 6000 RPM for 120 seconds. It was then baked on a hotplate at 180°C for 5 minutes. The wafer was then exposed by an electron-beam to create the pattern of the coordinates and markers. The development was performed in O-xylene for 5 minutes, followed by rinsing in IPA and drying in a N_2 flow. To remove the resist residues, the wafer was cleaned with an oxygen plasma asher for 45 seconds. Then PVD was used to evaporate 30 Å Ti and 300 Å Au. The lift-off process was then performed in a hot remover-1165 solution in a ultrasonic bath.

The preparation of the measurement wafer was finalized by fabricating bonding pads [Fig.2.2(c)]. The wafer first was spin-coated with LOR 7B resist and baked on a hotplate at 180°C for 5 minutes. The wafer was then spin-coated with S-1813 and baked on a hotplate at 115°C for 90 seconds. Ultraviolet (UV) light was used to expose the patterns, and then the wafer was developed in MF-319 solution, rinsed in deionized water and dried in a N_2 flow. After 45 seconds of oxygen plasma ashing, 50 Å Ti and 1000 Å Au metal layers were deposited using PVD. Then the metal was lifted-off in a hot remover S-1165 solution, followed by rinsing in water and drying in a N_2 flow. After cleaving the wafer into small silicon chips, the fabrication of low temperature measurement substrates was finished.

2.2.2 Fabrication of electric contacts to nanowires and local gates

So far we have got highly n-doped silicon substrates with SiO_2 insulating layers, coordinate systems and bonding pads on their polished sides, and Ti/Au metal layers on their backsides as global gates. They are ready to be deposited by nanowires.
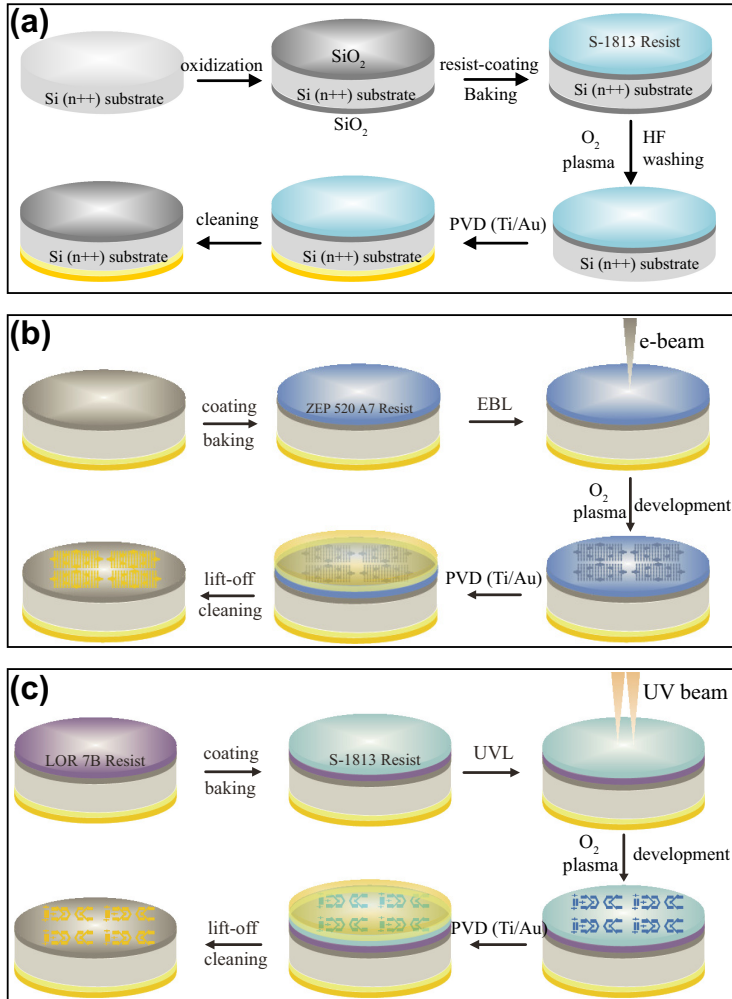
Figure 2.2: Preparation of the low temperature measurement substrates. (a) Chip oxidization, and back gate fabrication. (b) Fabrication of alignment markers. (c) Fabrication of the bonding pads. Figures are reproduced by courtesy of Chunlin Yu.
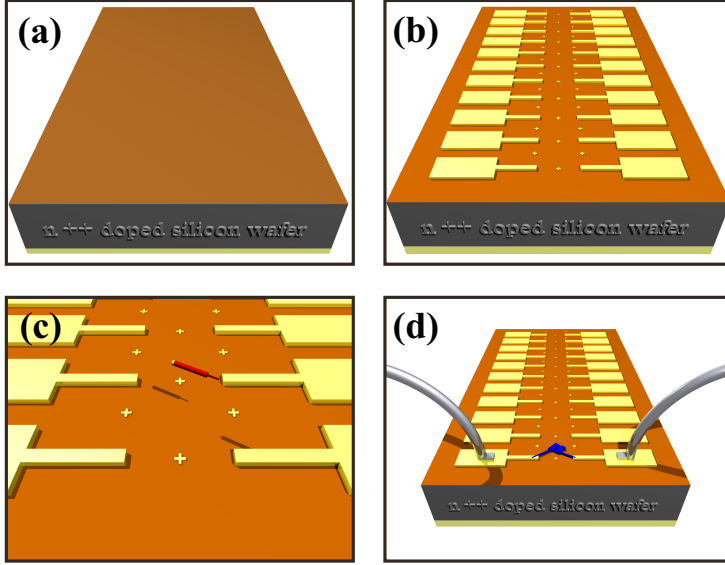
Figure 2.3: Schematics of fabrication process of nanowire-based device. (a) A highly n-doped silicon chip with a 100 nm SiO_x insulator layer on one side and a Ti/Au (5/120 nm) metal layer on the other side as a back gate. (b) Ti/Au (5/100 nm) bonding pads and Ti/Au (5/45 nm) alignment markers are made on the substrate. (c) Nanowires are deposited at the target region on the substrate. (d) Nanowires are contacted to metals and the bonding pads are bonded to aluminum wires.

The nanowires were dry-transferred to the measurement substrate from their growth substrate by using a clean room tissue. An optical microscope was used to record the positions of the nanowires. With the assistance of the pre-defined coordinate system on the substrate, we can select and locate well-positioned nanowires. In order to define the electric contacts, the sample was first spin-coated with Poly(methyl methacrylate) (PMMA) 950K A4 (or A5) at a spinning speed of 5000 RPM for 60 seconds, followed by baking on a hotplate at 180°C for 3-10 minutes. The contact patterns were written directly by an electron beams machine. Afterwards the sample was developed in MIBK for 90 seconds, and then rinsed in IPA for 60 seconds, followed by drying in a N_2 flow. Before any metal deposition, 15 seconds of oxygen plasma ashing was performed, in order to remove the residual polymers.

Before the metallization step, an essential chemical treatment is needed in

order to get good metal-semiconductor contacts. This is because there is a thin native oxide layer on the surface of each InSb/InAs nanowire, which will insulate the nanowire from the metal contacts. To achieve reliable contacts to nanowires, the surface oxides must be removed by etching and the resulting dangling chemical bonds should be immediately passivated to prevent the surface reoxidation (13). For InSb/InAs nanowires, the oxide layer etching and the surface passivation can be done simultaneously by using an ammonium polysulfide $[(NH_4)_2S_x]$ bath. The wet-etching/sulfur-passivation is performed in the diluted $(NH_4)_2S_x$ solution [the original solution was $(NH_4)_2S_x:H_2O = 1:10$] at 40°C for 1∼3 minutes. The passivated sample should be transferred into the evaporator chamber or the sputter chamber quickly and the chamber should be pumped to high vacuum for metallization.

Metal deposition can be performed in the thermal evaporation machine or sputtering machine, depending on the target materials. Deposition of Ti/Au layer or Ti/Al layer in this thesis was performed in a thermal evaporator, while Ti/Nb/Ti layer and Ti/Nb/Al layer were deposited in a sputter machine. The lift-off for thermal evaporated or sputtered metal layers was performed in hot acetone or hot remover S-1165 followed by IPA rinsing and N_2 drying. Then the device can be bonded to a measurement chip holder by aluminum wires and ready for electric measurements [Fig. 2.3].

Besides the global back gate (the Ti/Au layer on the backside of each substrate), local gates can also be added to the substrates as side gates, top gates or bottom gates [Fig. 2.4]. Local side gates can be fabricated with the metal contacts in the same process. Top gates can be made after the nanowire metallization. A dielectric layer is needed to insulate the nanowires from the top gates. The device shown in Fig. 2.4(c) used a 10 nm HfO_2 thin film as the dielectric layer, which is achieved by atomic layer deposition (ALD) at 100°C. For the bottom gated devices, local gate arrays have to be made ahead of the nanowire deposition. To insulate the nanowires from the gates, a dielectric layer is also required. The nanowires are then deposited on top of the local gate arrays and followed the same localization and metallization procedure described above.
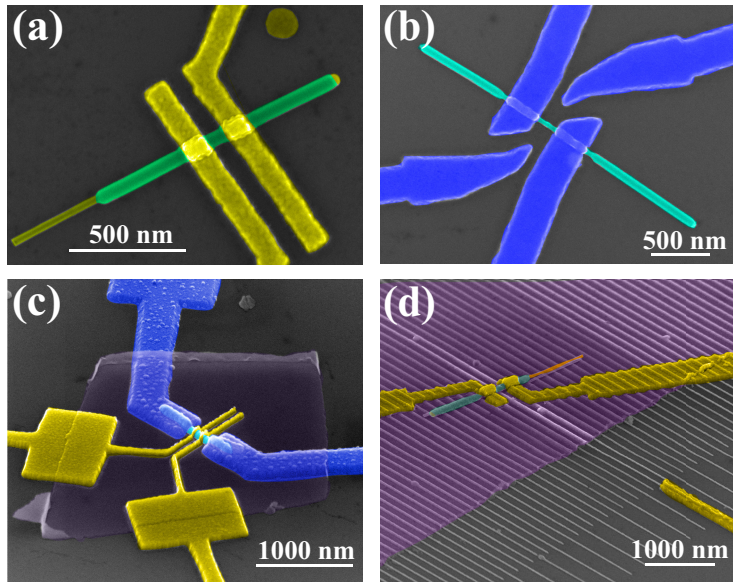
Figure 2.4: SEM images of several fabricated devices with different geometries. (a) SEM image of a two-terminal nanowire device with only a global back gate. (b) SEM image of a two-terminal nanowire device with a global back gate and two side gates. (c) SEM image of a two-terminal nanowire device with a global back gate and two local top gates. (d) SEM image of a two-terminal nanowire device with local bottom gates.

3

InSb Nanowire Quantum Dots

In this chapter, we first give a brief review on some fundamental conceptions related to quantum dots and basic properties of electron transport through single quantum dots. Several novel electron transport features in InSb nanowire quantum dots are also discussed.

3.1 Single quantum dot model

A single quantum dot is also referred to as an artificial atom due to its intrinsic charge and energy quantization that is analogous to an atom. The quantum dot system has been proven to be very useful to studies of a wide range of physical phenomena. A lot of theoretical and experimental work has been done to describe and understand the transport property through a quantum dot. In this section, we briefly introduce the most fundamental phenomena, and the electron transport mode of a single quantum dot. A more systematic physics analysis and detailed mathematical derivation of the transport model of quantum dots can be found in Refs. (1, 2) and references therein.

3.1.1 Charge quantization and energy quantization in a quantum dot

In 1897, J. J. Thomson discovered electrons from cathode ray experiments. A few years later, Robert Millikan did the famous oil drop experiment. Since then we have known that the electric charge is quantized with the elementary charge $e = 1.5924 \times 10^{-19}$ C, and the elementary electric charge e is the charge that is carried by an electron. In 1913, Niels Bohr proposed his Bohr model in which electron
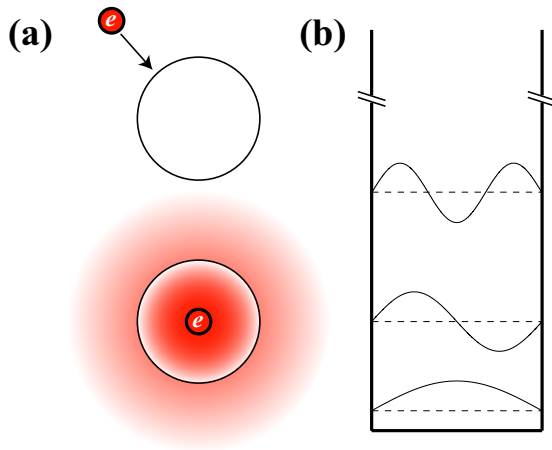
Figure 3.1: Schematic of charge quantization and electron energy level quantization. (a) Adding an extra electron onto a dot increases the dot energy by a charging energy. (b) Electron wave functions of the first three energy levels in an infinitely deep square well.

orbits and electron energies in atoms were believed to be quantized. The energy quantization of constrained electrons has been observed in many confined systems for the last century. Usually, the charge quantization and energy quantization are hardly seen in macroscopic systems. However, when the dimensions of an object are down-scaled below a few hundred nanometers, the charge quantization and energy quantization effect become non-negligible.

We start the discussion from an isolated small piece of conductor/semiconductor (a dot) with a capacitance C as depicted in Fig. 3.1 (a). Note that the capacitance C here is the *self-capacitance*, and thereby the electrostatic energy of the dot with charge Q is $U = Q^2/2C$ (taking infinity as the reference zero-energy point). We also assume the dot temperature is zero for all the discussion below except in some cases when the temperature is specified.

Suppose that the dot is originally electrically neutral. If we take an external electron from the infinity and add it onto the dot, the added electron will break the electric neutrality of the dot and generate a Coulomb repulsion force to other external electrons. From the energy point of view, the extra electron increased the total energy of the dot. Therefore, adding more external electrons onto the dot will cost more energy. This phenomenon is the so-called *Coulomb blockade*.

The electrostatic energies of the dot with $N-1$ and N electrons on the dot are $U(n-1) = [(n-1)e]^2/2C$ and $U(n) = (ne)^2/2C$, respectively. Therefore, the energy needed to add the Nth electron onto the dot is

$$\mu(N) = U(N) - U(N-1) = \frac{e^2}{C}(N - \frac{1}{2}) \tag{3.1}$$

The difference between $\mu(N)$ and $\mu(N-1)$ is called the *addition energy*, which means the energy that is further needed to add the Nth electron to the dot, based on the total required energy for adding the $(N-1)$th electron $\mu(N-1)$. That is

$$\Delta\mu(N) = \mu(N) - \mu(N-1) = \frac{e^2}{C} \tag{3.2}$$

We will see the reason why we introduce the concept of the addition energy when we discuss the measurements of quantum dot energy spectrums in the next subsection. In this case, the addition energy here only contains the item e^2/C which is referred to as the *charging energy*.

$$E_C = e^2/C \tag{3.3}$$

The analysis above does not consider the quantization of electron energy levels. However, energy quantization has to be considered when the dot is sufficiently small. As an example, the eigen energies of a 1D infinitely-deep square-well [Fig. 3.1 (b)] are

$$\epsilon_n = \frac{(\hbar\pi)^2}{2} \cdot \frac{n^2}{m_e^* L^2} \tag{3.4}$$

in which L is the length of the square well, m_e^* is the effective mass of the electron and $n = 1, 2, 3, ...$ We can see that the smaller the dot size is, the larger the level separation is. The potential profile of a real dot is usually not an ideal infinitely-deep square-well shape, but the energy quantization obeys the same principle, i.e., it correlates inversely with the dot size.

According to the Pauli exclusion principle, one quantum state can only hold one fermion. A single energy level (or an orbit state) can only hold two electrons with opposite spins. For a dot with an infinitely-deep square-well shaped potential-profile, the first added electron occupies the lowest energy level. The second added electron can also occupy the lowest energy level but it requires that the electron has an opposite spin to the spin of the first added electron. Therefore, the addition energy for the second electron is $\Delta\mu_2 = E_C$. However, the next
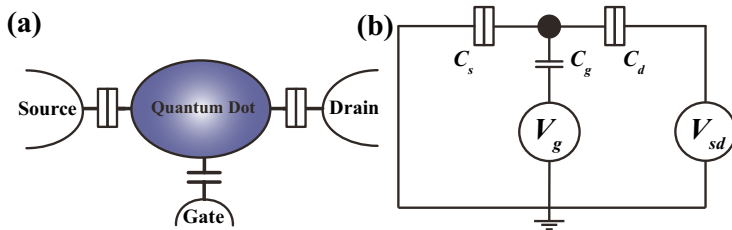
Figure 3.2: (a) Schematic of a single quantum dot. (b) Schematic of the electric circuit equivalent to a single quantum dot in the constant interaction model.

electron has to occupy the second lowest energy level, because the lowest one is fully occupied. Therefore, it needs more energy to add the third electron onto the dot, i.e., the addition energy for the third electron is $\Delta\mu_3 = \epsilon_3 - \epsilon_2 + E_C$. Generally, when considering electron energy level quantization, the addition energy of the Nth electron is:

$$\Delta\mu(N) = \Delta\epsilon_N + \frac{e^2}{C} \tag{3.5}$$

in which $\Delta\epsilon_N = \epsilon_N - \epsilon_{N-1}$ is the energy difference between the level energy of the Nth electron and the $(N-1)$th level energy. For the dot with an infinitely-deep square-well potential-profile, $\Delta\epsilon_2 = 0$, $\Delta\epsilon_3 = \frac{5}{2}(\hbar\pi)^2/m_e^*L^2$, $\Delta\epsilon_4 = 0$, $\Delta\epsilon_5 = \frac{7}{2}(\hbar\pi)^2/m_e^*L^2$, ... Because of the energy quantization, the dot is called a *quantum dot*.

The main difference between the quantum model discussed above and a real quantum dot is that a real quantum dot is not an isolated system. Instead, the quantum dot is generally embedded in a non-vacuum environment. In the context of transport, a quantum dot is a part of an electrical circuit. Figures 3.2 (a) and (b) show a schematic of an electric circuit equivalent to a quantum dot model. In this model, the quantum dot is coupled to the source and drain leads through tunnel barriers and it is capacitively coupled to a gate electrode. In the next subsection, we will see the source-drain leads serve as electron-reservoirs for the dot, and the gate is used to adjust the electrostatic energy of the dot. The source/drain and the gate also modify the total electrostatic energy of the dot by capacitive coupling:

$$U(N) = \frac{(Ne)^2}{2C_\Sigma} + eN\sum_{j=1}^{m}\frac{C_{0j}}{V_j} \tag{3.6}$$

where C_{0j} is the mutual capacitance of the electrode j (source/drain leads or

gate electrodes) and the dot, V_j is the electrostatic potential on the electrode j. Here, we rewrite the dot self-capacitance C as C_Σ because $C = C_\Sigma = -\sum_{j=1}^{m} C_{0j}$. Accordingly, the energy required to add the Nth electron to the dot should be modified to:

$$\mu_N = \epsilon_N + \frac{e^2}{C_\Sigma}\left(N - \frac{1}{2}\right) - e\sum_{j=1}^{m}\alpha_j V_j \qquad (3.7)$$

in which $\alpha_j = -C_{0j}/C_\Sigma$ is called the lever arm of electrode j. α_j is used in experiments to relate the gate voltage change to the dot potential change. It can be seen from Eq. 3.7 that the addition energy for the Nth electron remains in the form $\Delta\mu_n = \Delta\epsilon_n + e^2/C$ as Eq. 3.5.

3.1.2 Coulomb oscillations and charge stability diagram

In the dot model shown in Figs. 3.2 (a) and (b), the dot is separated from the source and drain leads by tunnel barriers. In fact, the quantum dot is *defined* by these barriers. Below we will discuss how the current flows through the quantum dot and typical transport-methods of studying a quantum dot.

Classically, if the energy of an incident electron, E, is smaller than the barrier height V_0, the electron will be reflected backward with a probability of 100%. However, in quantum mechanics, the electron has a non-zero probability to go through the barrier even with $E < V_0$. This process is called *tunneling*. For a 1D square-barrier [Fig. 3.3 (a)], the *electron transmission coefficient* (i.e., the probability of the electron to tunnel through the barrier) is given by:

$$T = \left[1 + \frac{V_0^2}{4E(V_0 - E)}\sinh^2\left(a\sqrt{2m_e^*(V_0 - E)}/\hbar\right)\right]^{-1} \qquad (3.8)$$

where a is the barrier width. Figure 3.3 (b) shows the plot of T of a square-barrier as a function of the incident electron energy E ($a = 20$ nm, $V_0 = 0.5$ eV, and $m_e^* = 0.015m_0$). In contrast, the dashed-line corresponds to the classical $T - E$ relation.

If there are two tunnel barriers in series [Fig. 3.3 (c)], a 1D finitely-deep square-well is formed in between the two barriers. Electrons are confined in the well. Unlike the square-well shown in Fig. 3.3 (d), the quantum states in the tunnel-barrier defined well are not real bound states. Because the electrons on these states could tunnel out of the well, these states are referred to as *quasi-bound states*.
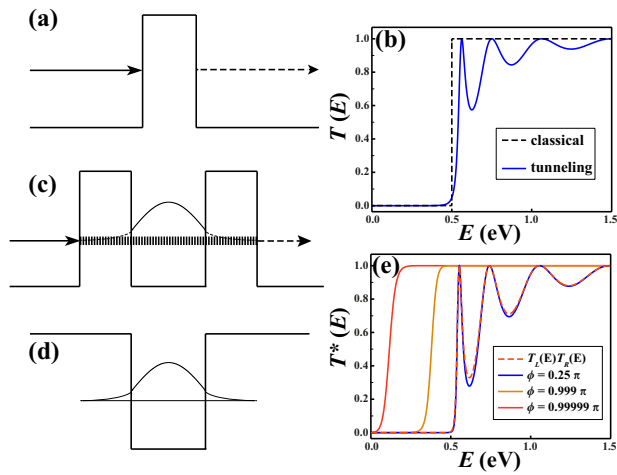
Figure 3.3: Electron tunneling through potential barriers. (a) A 1D square barrier. (b) Transmission coefficient of the square barrier shown in (a), as a function of the energy of the incident electron. (c) A quantum well formed by two square barriers. (d) A quantum well with infinitely-thick square barriers. (e) Transmission coefficient of the quantum well shown in (c) as a function of the energy of the incident electron, with different ϕ values.

One might think that the net transmission coefficient of the well shown in Fig. 3.3 (c) would be the product of the left-barrier coefficient and the right-barrier coefficient $T^* = T_L T_R$. T^* indeed approximately equal to $T_L T_R$ in some cases. However, when the energy of the incident electron approaches the energy of a quasi-bound state in the well, T^* increases significantly. This is because the electron will experience a perfectly coherent bouncing back and forth process between the two barriers at a quasi-bound state. Therefore, the quasi-bound state is also called the *resonant state*. In the symmetrical case $T_L = T_R = T$, the net transmission coefficient of the well is given by:

$$T^* = \frac{T^2}{T^2 + 4\,(1 - T)\sin^2\phi} \tag{3.9}$$

where ϕ is the picked-up phase in each bounce. Figure 3.3 (e) shows a few $T^* - E$ curves with different ϕ values. The dashed line represents the product $T_L T_R$. One has to note that in most quantum well systems, ϕ is interrelated with k-vector and therefore interrelated with E. It can be seen that T^* peaks to unity even with $E < V_0$ when $\phi = n\pi$. The condition of $\phi = n\pi$ is also the condition for the forming of the electron standing-wave in the potential well. In the case of quantum dots, the quantum dot is most electrically transparent when the energy of the incident electron is equal to a quantized electron level. The electron tunneling through the quantum level is therefore called the *resonant tunneling*.

Now we link the single electron-tunneling-event with the current through a quantum dot. Without any high-order co-tunneling event, three conditions have to be met to have a net-current flowing through a quantum dot: a non-zero transmission coefficient, a non-empty electron reservoir on one side, and empty states that can accept the tunneled electrons on the other side. The latter two conditions can easily be satisfied by applying a bias-voltage V_{sd} to the source-drain leads of the quantum dot. An energy window is then formed between the chemical potential of the source lead μ_s and the chemical potential of the drain lead $\mu_d = \mu_s - eV_{sd}$. Electrons can flow through the quantum dot when one or more resonant states are lying in the energy window $\mu_s - \mu_d$.

Figure 3.4 shows schematic energy diagrams of a quantum dot. In Fig. 3.4 (a), there is no resonant state in the bias window and thereby no net-current through the quantum dot. In Fig. 3.4 (b), a current can flow through the dot via the bridging of a resonant level. The two different states in Figs. 3.4 (a) and (b) are
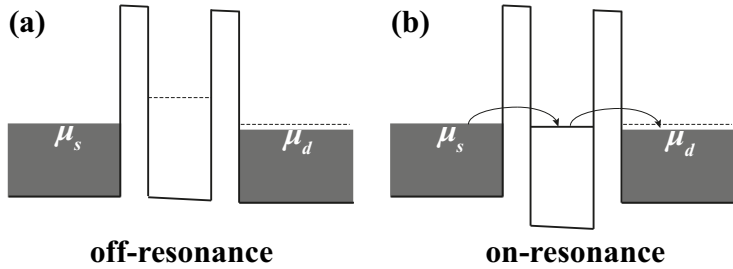
Figure 3.4: The off-resonance and on-resonance states. (a) The resonant level is out of the energy window between μ_s and μ_d. The quantum dot is in an off-resonance state and no current flows through the quantum dot. (b) The resonant level is in the energy window between μ_s and μ_d. The quantum dot is in an on-resonance state and a non-zero current flows through the quantum dot.

called *off-resonance* and *on-resonance* states, respectively. The resonance on/off switching in Figs. 3.4 (a) and (b) is performed by adjusting the chemical potential of the quantum dot. This adjustment is achieved via a voltage V_g applied to its gate. If we fix V_{sd} at a small value and sweep V_g continuously, the conductance of the quantum dot will oscillate significantly due to the alternation of on/off resonance. The conductance oscillation with V_g is called the *Coulomb oscillation*.

Figure 3.5 shows an example of Coulomb oscillation. The data is taken from the measurement results of a Au-InSb NW-Au device (Dev. *AuInSbAu#1*). Shown as the SEM image in the inset of Fig. 3.5 (a), two Ti/Au (5/90 nm) leads are contacted to the MOVPE-grown InSb nanowire with a 330 nm separation in-between. The diameter of the nanowire is 75 nm. The measurements were performed in a $^3He/^4He$ dilution refrigerator with a base temperature of 25 mK. A quantum dot is formed in the InSb nanowire segment between the contacts. The quantum dot is defined by the barriers that are induced by the metal-semiconductor contacts. Figure 3.5 (a) displays the measured source-drain current I_{sd} as a function of the voltage applied to the global back gate V_{bg}. The source-drain bias voltage V_{sd} is fixed at 25 μV which is much smaller than the charging energy E_C and the quantization energy difference $\Delta\epsilon$. It can be seen that in most cases I_{sd} is very small, except near the arrow-marked points where I_{sd} peaks. The current peaks are due to the alignment of one electron energy level in the dot and the small source/drain energy window. As V_{bg} increases, the chemical potential of the quantum dot drops, and therefore electrons near
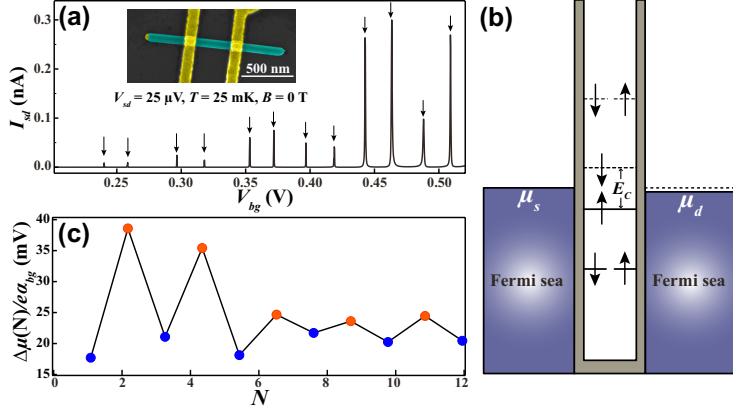
Figure 3.5: Coulomb oscillations. (a) The source-drain current I_{sd} measured for a single quantum dot device as a function of back gate voltage V_{bg} at $T = 25$ mK and $B = 0$ T. The source-drain bias voltage V_{sd} is fixed at 25 μV. The Coulomb oscillations occur in the form of repeated conductance peaks. The inset is the SEM image of the measured device. (b) Schematic energy diagram of a quantum dot. (c) Distances V_{add} (in the scale of V_{bg}) between adjacent peaks in panel (a) as a function of the number of electrons in the dot. V_{add} alternates between large value and small value due to spin degeneracy of the quantum levels in the dot.

the Fermi level of the contacts have higher energy relative to the dot. Quantum levels in the dot successively fall into the source/drain energy window and increase the tunneling current by resonance. After passing the energy window, the quantum level is off resonance and the current drops back to a low level. Then, the quantum state is occupied by an electron. The energy separation between peak $N-1$ and peak N is exactly the addition energy of the Nth electron $\Delta\mu(N)$ according to its definition, as discussed above.

If we consider the spin degeneracy, one orbit state can only hold two electrons with opposite spins. Therefore, once one of the two spin-states of an orbit level is occupied, the addition of an electron to another spin-state just needs an increase in the incident electron energy by a charging energy E_C[Fig. 3.5 (b)]. In this case, the addition energy is equal to E_C. Otherwise, the addition energy is $E_C + \Delta\epsilon$. Figure 3.5 (c) shows the distance of adjacent peaks in Fig. 3.5 (a) in the scale of V_{bg} (i.e., $\Delta\mu(N)/e\alpha_{bg}$), as a function of the number of electrons in the dot. We can see that $\Delta\mu(N)/e\alpha_{bg}$ has larger values when N is an even number and

has smaller values when N is odd. This is called even-odd alternation behavior, which results from the spin degeneracy.

The current peaks in Fig. 3.5 (a) supply us with the information of the quantum levels in the dot and is therefore sometimes referred to as the *spectrum* of the quantum dot.

Besides adjusting the chemical potential of the quantum dot via gate(s), increasing the bias energy window can also switch the on/off-resonance state of the quantum dot. The combination of gate adjustment and bias variation will give several different conductance states. The quantum dot has different conductance at different combinations. If we plot the differential conductance dI_{sd}/dV_{sd} as a function of V_{sd} and V_g, we get a 2D diagram which is called the *charge stability diagram*. Figure 3.6 shows a schematic of the charge stability diagram and several typical combinations, corresponding to different places in the stability diagram. We can see that the stability diagram is separated into diamond-blocks, which are called the *Coulomb diamonds*. The borders between different Coulomb diamonds represent conductance thresholds of the quantum dot, and the dI_{sd}/dV_{sd} reaches maxima on the borders.

The charge stability diagram can help us characterize and analyze a quantum dot. For instance, we can directly get a very accurate estimation of the addition energy from the half-width (along the V_{sd} axis) of the corresponding diamond (V_{sd}^{HW} in Fig. 3.6). The addition energy $\Delta\mu$ is approximately equal to eV_{sd}^{HW}. We can also calculate the lever arm of the gate:

$$\alpha_g = V_{sd}^{HW}/V_g^{FH} \tag{3.10}$$

in which V_g^{FH} is the full height (along the V_g axis) of the corresponding diamond as shown in Fig. 3.6.

In Fig. 3.7, we show three charge stability diagrams measured for InSb nanowire quantum dot devices. Figure 3.7 (a) displays the charge stability diagram measured for Dev. *AuInSbAu#2* whose SEM image is shown in Fig. 3.7 (b). The nanowire in this device was grown by MBE with a diameter of 95 nm. It is contacted by two Ti/Au(5/90 nm) leads with a spacing of 360 nm. A clear Coulomb diamond structure can be seen from the diagram. We can extract the addition energies to be 1.2∼2 meV in this given V_{bg} region. Figures 3.7 (c) and (d) are the charge stability diagrams for Dev. *AuInSbAu#1* at different temperatures. The addition energies of Dev. *AuInSbAu#1* are about 4∼8 meV and are much
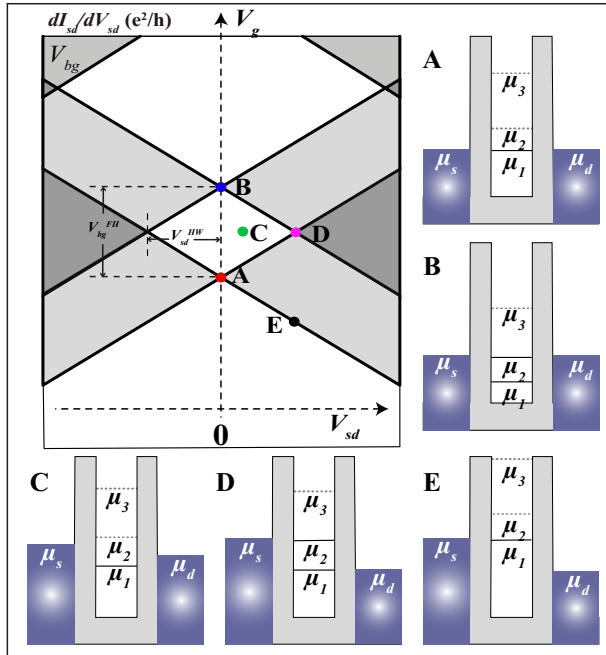
Figure 3.6: A sketch of the charge stability diagram of a single quantum dot. Different configurations of source/drain chemical potentials and the dot energy levels at points *A-E* are illustrated separately in schematic energy diagrams.
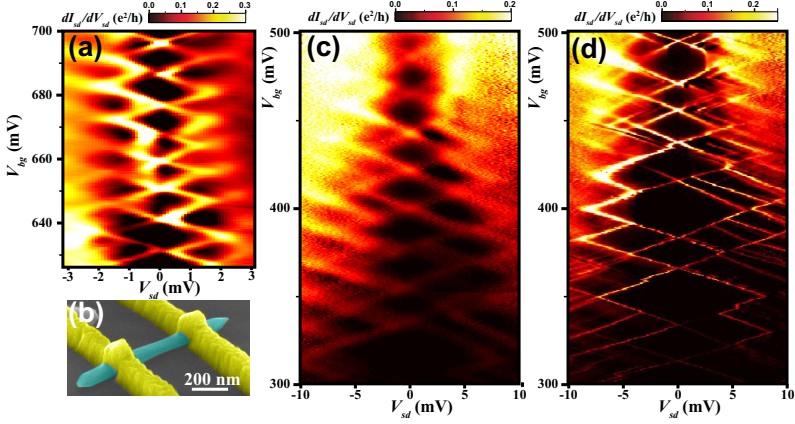
Figure 3.7: Charge stability diagrams. (a) The charge stability diagram measured for a Au-InSb NW-Au device (Dev. *AuInSbAu#2*). The measurements are performed at $T = 25$ mK and $B = 0$ T. (b) The SEM image of Dev. *AuInSbAu#2*. (c)-(d) The charge stability diagrams measured for Dev. *AuInSbAu#1*. The diagram in panel (c) is taken at $T = 4.2$ K, while (d) is taken at $T = 25$ mK.

larger than the ones of Dev. *AuInSbAu#2*. The reason for this is that the dot size of Dev. *AuInSbAu#2* is larger than Dev. *AuInSbAu#1* in terms of contacts spacing and nanowire diameters. Another reason is that Dev. *AuInSbAu#2* is in a many-electron transport regime for the V_{bg} region in Fig. 3.7 (a). In this regime, the effective quantum dot volume expands largely as a result of global gating and the electric field-retroaction to the barriers from electrons in the dot. The increase of the dot volume leads to a decrease of the charging energy and quantum level separations.

As expected, the Coulomb diamond borders are broader at $T = 4.2$K [Fig. 3.7 (c)] than at $T = 25$ mK [Fig. 3.7 (d)]. If the temperature increases until the thermal energy is larger or comparable to the charging energy ($k_BT \geq E_C$), Coulomb oscillation features and Coulomb diamond structures will be smeared out.
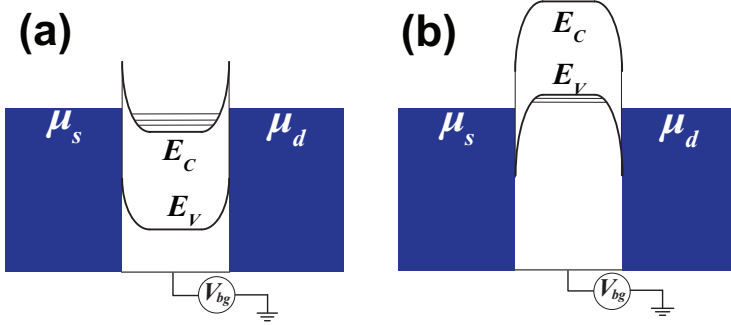
Figure 3.8: Schematic energy diagrams of an ambipolar quantum dot. (a) An n-type quantum dot. (b) A p-type quantum dot.

3.2 Ambipolar InSb nanowire quantum dot

So far, we have discussed the electron tunneling through a quantum dot. We have also shown measured Coulomb oscillations and charge stability diagrams for InSb nanowire-based quantum dots. We assume the quantum dot is "n-type", i.e., the quantum well is assumed to be formed above the bottom of the conductance band of the InSb nanowire. Moreover, the quantum state of the dot is called *occupied* if there is an electron on the level. Likewise, a "p-type" quantum dot can be formed if there is a potential well for holes in the valance band. The potential well for holes is a reversed potential well for electrons, and holes are constrained in the potential well. In this context, a quantum state is hole-occupied if there is no electron on that state. Since InSb is a narrow band gap [$E_g = 0.235$ eV at $T = 0$ K (14)] material, it is possible to tune an InSb quantum dot from n-type to p-type by gating, as shown in Fig. 3.8.

We show a typical ambipolar quantum dot device (Dev. *AlInSbAl#1*) in Fig. 3.9. The InSb nanowire in Dev. *AlInSbAl#1* is contacted by two Ti/Al(5/75 nm) contacts[1] with a separation of 100 nm. Figure 3.9 (a) shows the source-drain current I_{sd} as a function of back gate voltage V_{bg}, measured for Dev. *AlInSbAl#1* under a source-drain bias voltage of $V_{sd} = 0.2$ mV. The measurements show clear

---

[1]Al is a superconductor at the temperature where the measurements are performed. The superconductivity modifies the transport features in a certain way (see Chapt. 4), however, the main observation for the physics of the ambipolar quantum dot effect remains consistent with a normal metal-contacted quantum dot.

ambipolar quantum dot behavior. Two strong current peaks seen at $V_{bg} \sim -0.7$V are the Coulomb oscillation peaks rising from the electron transport through the quantum dot. Therefore, the quantum dot is n-type in this V_{bg} region. As V_{bg} goes toward to more negative values, a non-current region appears after the last electron is emptied from the dot. However, as V_{sd} becomes sufficiently negative ($V_{bg} < -4$ V), a region with sharp current peaks appears. These current peaks resemble the hole transport through quantum states in the InSb nanowire quantum dot. These observed current peaks are much sharper and have a height of at least 3 orders of magnitude smaller than the observed current peaks in the electron transport region. This implies that the tunneling barriers in the hole transport regime of the device are much higher than the barriers in the electron transport regime.

Figures 3.9 (b) and (c) show the charge stability diagrams of a selected many-hole and a selected few-hole transport region, respectively. Figure 3.9 (d) shows the charge stability diagram in the electron transport region with mainly a single electron occupation in the dot. Here, we note that the measurements in the electron transport region are performed in an applied magnetic field of 1.5 T, in order to suppress the superconductivity-induced features (see Chapt. 4).

Figure 3.10 shows Coulomb oscillations of another ambipolar quantum dot device (Dev. *NbInSbNb#1*). In this device, the InSb nanowire is contacted by two Ti/Nb/Al(3/80/5 nm) contacts with a separation of 150 nm. In the electron transport regime of the device, the Coulomb oscillation is clearly seen in Fig. 3.10 (a) with the conductance peaks as high up as $\sim 0.6e^2/h$ in this region. The addition energy is extracted from Fig. 3.10 (a) and summarized in Fig. 3.10 (b). Note that the addition energy is calculated according to $\Delta(N) = e\alpha_{bg}\Delta V_{bg}$ where α_{bg} is the lever arm of the back gate and ΔV_{bg} is the distance (in the scale of V_{bg}) between adjacent peaks. We can see that the addition energy shows a very clear even-odd alternation behavior. The alternation of $\Delta(N)$ indicates that the electron energy quantization in this regime is pronounced and is comparable to the charging energy for the n-type quantum dot regime. The charging energy can be estimated from the addition energy of the Coulomb diamond with an odd-occupation, which gives $E_C^e = 2.5 \sim 4$ meV. If we take $\Delta E(n) = \frac{1}{2}[\Delta\mu(2n+1) + \Delta\mu(2n-1) - \Delta\mu(2n)]$ as an estimation of the quantum energy difference $\Delta\epsilon(n)$. This gives a $\Delta_E(n)$ ranging from 0.5 meV to 7 meV.

However, when a negative back gate voltage ($V_{bg} \sim -10$ V) is applied to the
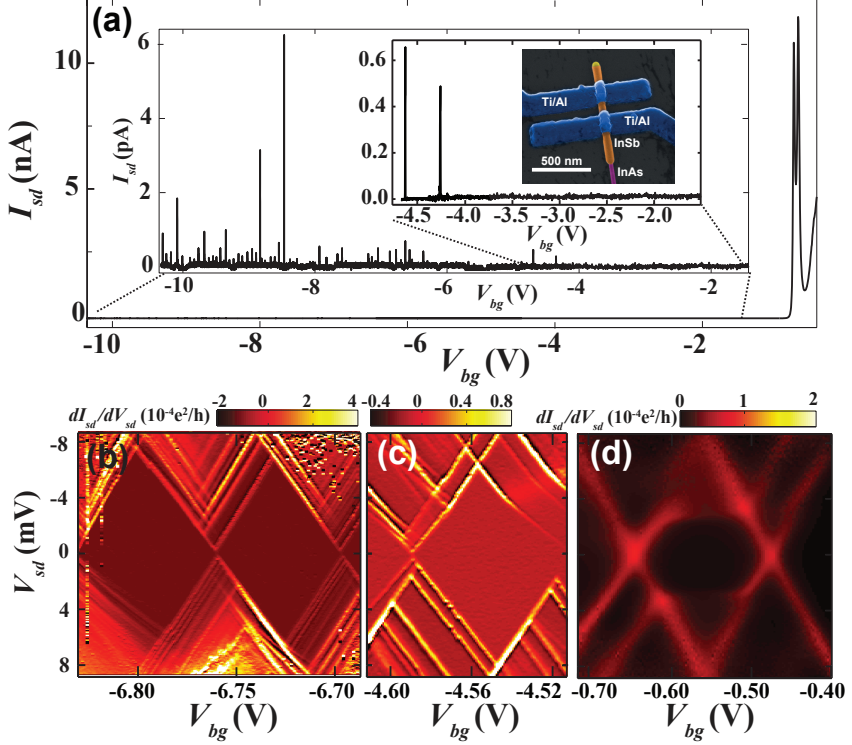
Figure 3.9: Measurements of an ambipolar quantum dot device. (a) The measured I_{sd} as a function of V_{bg} with an applied $V_{sd} = 0.2$ mV at $T = 25$ mK and $B = 0$ T. Current peaks in the electron transport regime appear at around $V_{bg} = -0.7$ V, while the Coulomb oscillation of the hole transport regime occurs when $V_{bg} < -4$ V. The inset curve is a close-up view of the few-hole regime. The inset SEM image is taken from the measured device. (b) and (c) are the charge stability diagrams measured in the hole transport regime at $B = 0$ T. (d) is the charge stability diagram measured in the electron transport regime at $B = 1.5$ T.

device, the dot is tuned to the p-type regime. Figure 3.10 (c) shows the Coulomb oscillation of the hole transport regime. Just like Dev. *AlInSbAl#1*, the quantum dot is much more electrically opaque in the p-type regime than in the n-type regime. The addition energy for the V_{bg} region shown in Fig. 3.10 (c) is extracted and shown in Fig. 3.10 (d). In contrast to the n-type region, the addition energy does not show an even-odd alternation and is almost constant here. This implies the energy quantization is small for the p-type regime and the addition energy is approximately equal to the charging energy $E_C^h \approx \Delta\mu(N) \approx 4.5$ meV.

The energy quantization difference between the n-type quantum dot regime and the p-type regime is pronounced. According to Eq. 3.4, one might think this is because the selected p-type region is in the many-hole regime (having a larger effective dot size), while the selected n-type region is in the few-electron regime (having a smaller effective dot size). According to the relation $E_C = e^2/C_\Sigma$, we can deduce the dot self-capacitances for the n-type region $C_\Sigma^n \approx 50$ aF and for the p-type region $C_\Sigma^p \approx 35$ aF. If we assume that the geometry of the quantum dot is a solid-cylinder with a radius of 30 nm, we can estimate that the lengths of the dot are $\sim$30 nm and $\sim$10 nm for the n-type and p-type regions, respectively[1]. Although the calculated dot lengths are not very consistent with the assumption of a cylinder-dot geometry, the effective volume of the p-type dot is likely to be smaller than the volume of the n-type dot. We have to consider the difference between the effective mass of the conductance-band electron m_e^* and of the valance-band hole m_h^*. For InSb bulk material, we have $m_e^* = 0.0135m_0$, $m_{hh}^* = 0.44m_0$ (heavy hole[2]) and $m_{lh}^* = 0.016m_0$ (light hole) (14, 15). Because the heavy hole band is above the light hole band in the band structure of InSb and $m_{hh}^* \gg m_{lh}^*$, the p-type quantum dot favors populating itself with heavy holes at the low-energy regime. Therefore, according to Eq. 3.4, the heavy holes have a much smaller quantization effect than electrons for the same dot size.

With both n-type and p-type properties, the InSb quantum dot could simplify the design and assembling of single electron/hole transistors circuits significantly. In addition, the p-type quantum dot has some unique properties. For example, the quantum dot has a strong spin-orbit interaction (see the introduction of spin-orbit interaction in later sections) in the hole transport regime. Moreover, hole

---

[1]The calculation was performed using the self-capacitance of a solid cylinder on *WolframAlpha*.

[2]Heavy-hole effective masses of InSb: $m_{hh}^*[100] = 0.32m_0$, $m_{hh}^*[110] = 0.42m_0$ and $m_{hh}^*[111] = 0.44m_0$
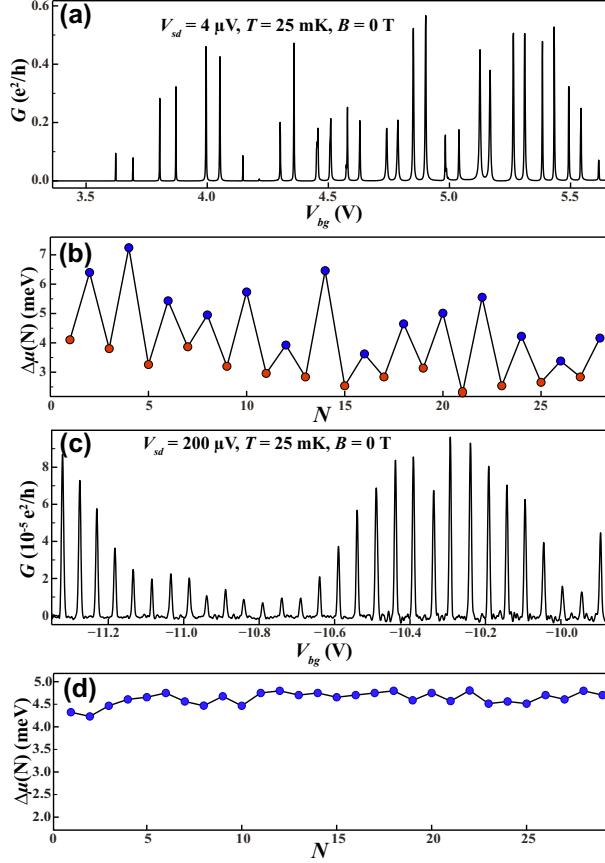
Figure 3.10: Coulomb oscillations of an ambipolar InSb quantum dot device. (a) The linear-response conductance G measured for the device as a function of V_{bg} at $T = 25$ mK and $B = 0$ T. V_{sd} is fixed at 4μV. The Coulomb oscillations occur in the form of repeated conductance peaks. The dot is in the electron transport regime in this selected V_{bg} region. (b) The addition energy for panel (a) as a function of the number of electrons in the dot. The even-odd alternation behavior of the addition energy is clearly seen. (c) The linear-response conductance G measured for the same single quantum dot device as the one in panels (a) and (b) (in different V_{bg} region), as a function of V_{bg} at $T = 25$ mK and $B = 0$ T. V_{sd} is fixed at 200μV. The conductance peaks are due to the Coulomb oscillation in the hole transport regime. (d) The addition energy for panel (c) as a function of the number of holes in the dot. No obvious even-odd alternation behavior is visible.

spins have weak coupling to nuclear spins. This leads to a longer spin-coherence time and better spin-controllability. Therefore, p-type quantum dots may bring some advantages for the realization of spin qubits(16).

3.3 Zeeman effect

At zero magnetic field, each of the orbit states of the quantum dot has two different spins states ($s = \pm 1/2$). In finite fields, however, the spin states will split in energy and the spin degeneracy is lifted. This field-induced spin states splitting is called the *Zeeman effect* (17, 18). According to the Zeeman effect, the energy shifting of a spin state within a magnetic field is given by:

$$E_z(B) = |sg^*\mu_B B|, \quad s = s_\uparrow, s_\downarrow \tag{3.11}$$

in which μ_B is the Bohr magneton, g^* is the effective g-factor and $s_\uparrow = \frac{1}{2}, s_\downarrow = -\frac{1}{2}$ are the spins for the up-spin and down-spin states. Since $s_\uparrow$ and $s_\downarrow$ have opposite signs, the magnetic field shifts one spin state to a lower energy while shifting the other spin state to a higher energy. Therefore, the difference of the energies associated with the two spin states will increase as the magnetic field increases, and results in the splitting of the corresponding spectrum line of the quantum dot. The splitting is thereby referred to as the *Zeeman splitting*. The energy splitting is given by $\Delta E_z(B) = |(s_\uparrow - s_\downarrow)g^*\mu_B B|$.

In Fig. 3.11 (a), we display the linear-response conductance on a color scale measured for Dev. *AuInSbAu#1* as a function of V_{bg} and magnetic field B, with a small fixed source-drain bias voltage $V_{sd} = 25~\mu V$. The dark lines on the color scale represent the current peaks and imply the quantum dot is on a resonance state at these $V_{bg} - B$ points. At zero-field region, we can see that an even-odd alternation behavior of the addition energy. Therefore, we can identify the four levels as $|n, \uparrow\rangle$, $|n, \downarrow\rangle$, $|n+1, \uparrow\rangle$ and $|n+1, \downarrow\rangle$, from lower energy to higher energy. As the magnetic field increases, the spin degeneracy is lifted and the quantum levels begin to shift. The levels $|n, \uparrow\rangle$ and $|n+1, \uparrow\rangle$ bend to lower energy, while levels $|n, \downarrow\rangle$ and $|n+1, \downarrow\rangle$ bend to higher energy. Figure 3.11 (b) shows the schematic energy diagrams of the device at the points labeled as A, B and C in Fig. 3.11 (a). Due to the Zeeman effect, the quantum level $|n, \downarrow\rangle$ is shifted above the level $|n+1, \uparrow\rangle$ at point C. That means there is a crossover[1] that occurs

---

[1]Strictly speaking, there is an anti-crossing when they approach each other because of the spin-orbit
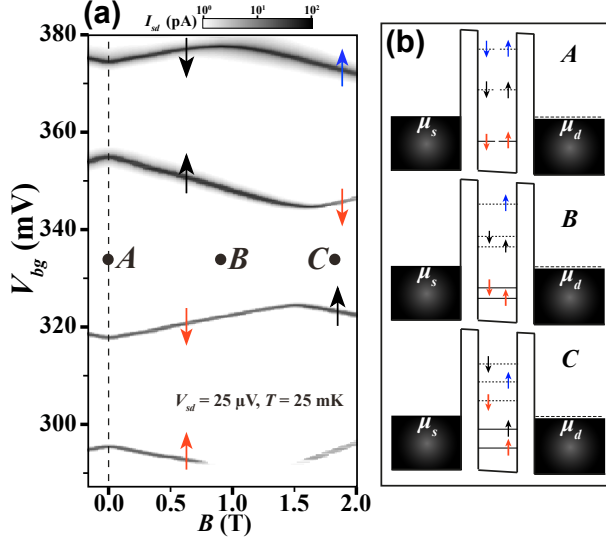
Figure 3.11: The Zeeman effect of a InSb quantum dot devce. (a) The linear-response conductance measured for Dev. *AuInSbAu#1* as a function of V_{bg} and magnetic field B. Arrows indicate spins of corresponding resonant levels. (b) Schematic energy diagrams of the device at the point labeled with A, B and C in panel (a).

between $|n, \downarrow\rangle$ and $|n + 1, \uparrow\rangle$ from point B to point C.

If no other interactions are taken into account, the magnitude of the Zeeman splitting is linearly proportional to the external magnetic field, i.e., g^* is constant and independent of the dot size, the orbital state, and the external field orientation. The electron spin g-factor g for free electrons is approximately equal to 2.002319, but the effective g-factor g^* in semiconductors varies a lot. Due to the modification of the crystal periodic potential, the effective electron g-factor varies significantly for different semiconductor materials (19). Additionally, due to orbit interactions and other mechanisms, the effective g-factor of a nanoscale object shows level dependence (20), magnetic field orientation dependence (21), and electrical field dependence (22).

The effective g-factor of bulk InSb is as high as 51 (23) which is the largest among all III-V semiconductors. For InSb quantum dots, the g-factor fluctuates greatly for different quantum levels and varies from device to device. Thereby,

interaction which will be introduced later.
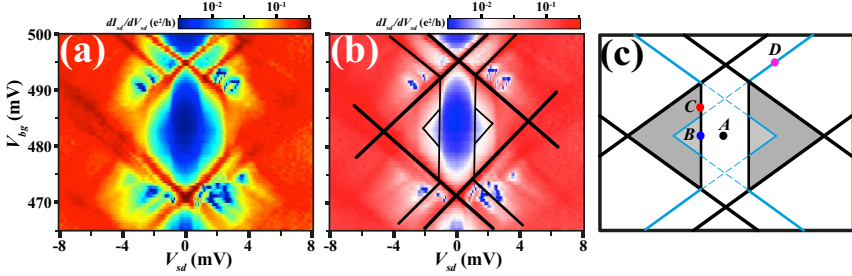
Figure 3.12: Electron co-tunneling induced conductance in the Coulomb blockade region. (a) A close-up view of part of the charge stability diagram in Fig. 3.7 (c). The conductance in the Coulomb blockade region is not zero due to electron co-tunneling processes. (b) The same with panel (a) but with guiding lines for transport thresholds, which indicate onsets of different transport processes. (c) A sketch of panels (a) and (b).

the effective g-factor g^* is usually written as g_n^* for the quantum state $|n\rangle$. The effective g-factor of a quantum level can be derived according to its level evolution in a magnetic field as shown in Fig. 3.11 (a). We give a detailed g-factor derivation in a later section, where other g-factor derivation methods are also discussed.

3.4 Electron co-tunneling of InSb nanowire quantum dot devices

So far, we have discussed the *sequential tunneling* of electron through a single quantum dot. In the sequential tunneling process, electrons tunnel through the quantum dot one by one. The tunneling is only allowed to happen around the resonant levels and is forbidden when the electron is far from the resonant levels, i.e., in Coulomb blockade regions. However, we see the tunneling current in Fig. 3.7 is not zero even in the Coulomb blockade regions. Figure 3.12 shows a zoomed-in view of part of Fig. 3.7 (d), in which the non-zero conductance in the Coulomb blockade region is shown clearer. To interpret the non-zero tunneling current in the energetically forbidden regime, we have to introduce the concept of *electron co-tunneling*.

3.4.1 Elastic co-tunneling in InSb quantum dots

The electron co-tunneling transport refers to an electron-tunneling process in which several tunneling events are related and several electrons are involved. Co-tunneling involves tunneling through energetically forbidden states, or so-called *virtual states*. It is a high order application of the Heisenberg uncertainty principle. Tunneling through virtual states is possible if the timescale of the process is short enough to be allowed by the uncertainty principle. It is therefore essential to have strong source and drain tunnel coupling so that the tunneling times are of the same order as the timescale defined by the uncertainty principle.

We start the discussion from the lowest order co-tunneling process, namely the *elastic co-tunneling*. In Fig. 3.13, schematic energy diagrams of a quantum dot are shown. Since the quantum dot is in a Coulomb blockaded configuration (the source-drain bias voltage is small and resonant levels are out of the bias energy window), no first order tunneling current will flow through the dot in the picture of sequential tunneling. However, following the Heisenberg uncertainty principle, the electron on the ground state of the quantum dot can potentially escape from the dot in a timescale of $\sim \hbar/|\varepsilon_0|$. This intermediate and energetically forbidden state is a virtual state. If another electron in the contacts tunnel into the dot and turn the dot back to its initial charge state, the total energy is conserved in the whole process (24). Because of the energy conservation in this co-tunneling event, it is therefore called *elastic co-tunneling*. Elastic co-tunneling can happen at any source-drain bias voltage as long as the coupling between the dot and contacts is strong enough. In Fig. 3.12, the non-zero conductance around point A can be attributed to the elastic co-tunneling.

3.4.2 Inelastic co-tunneling in InSb quantum dots

As shown in Fig. 3.12 (a) and by the guiding lines in Fig. 3.12 (b), the conductance profile contains more features and indicates that there are other transport mechanisms. Figure 3.14 displays the schematic energy diagrams for another form of co-tunneling process. This co-tunneling also starts from the tunneling out of the electron on the ground state via a virtual state. However, the subsequent tunneling-in electron tunnels into the excited state instead of the ground state. Finally, the quantum dot ends up in an excited state and therefore this co-tunneling is called the *inelastic co-tunneling* (25). Inelastic co-tunneling results
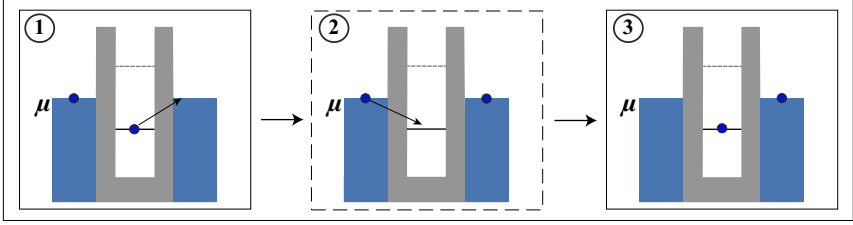
Figure 3.13: The schematic energy diagrams of elastic co-tunneling process. In the sequential tunneling blockade region, two electrons can tunnel in and out of the dot simultaneously via the virtual state and an elementary charge is transferred from source (drain) to drain (source). This co-tunneling leads a small conductance in the Coulomb blockade region.

in a conductance enhancement inside the Coulomb blockade region. In contrast to the elastic co-tunneling, the inelastic co-tunneling requires a source-drain bias voltage $V_{sd} \geq \Delta\varepsilon/e$ in order to conserve the energy of the total system. An inelastic co-tunneling process can happen in the gray region of Fig. 3.12 (c).

The subsequent transport for the final state of the inelastic co-tunneling depends on the dot configuration. In Fig. 3.14 (a), the excited state is out of the bias energy window and the first order tunneling is still forbidden. If the dot does not decay to its ground state by releasing phonons/photons, electrons in the contacts can only go through the dot in the form of co-tunneling (elastic or inelastic). However, in Fig. 3.14 (b), the excited state is in the bias energy window and thereby the electron can tunnel directly out of the dot in the form of first order tunneling. This sequential tunneling is thereby called the *co-tunneling assisted sequential tunneling* (CAST) (26, 27). The CAST leads to a further conductance enhancement compared to the configuration in Fig. 3.14 (a). Point B and the small split-diamond structure (surrounded by blue lines in the diamond) in Fig. 3.12 (c) correspond to the configuration as in Fig. 3.14 (a), while point C and its nearby region correspond to the CAST case.

3.4.3 Sequential tunneling via excited state

Along the extension lines of the inner thresholds of the CAST region (the dashed blue lines), high conductance lines show up outside of the Coulomb diamond and are parallel to the diamond borders. As shown in Fig. 3.14 (c), this can
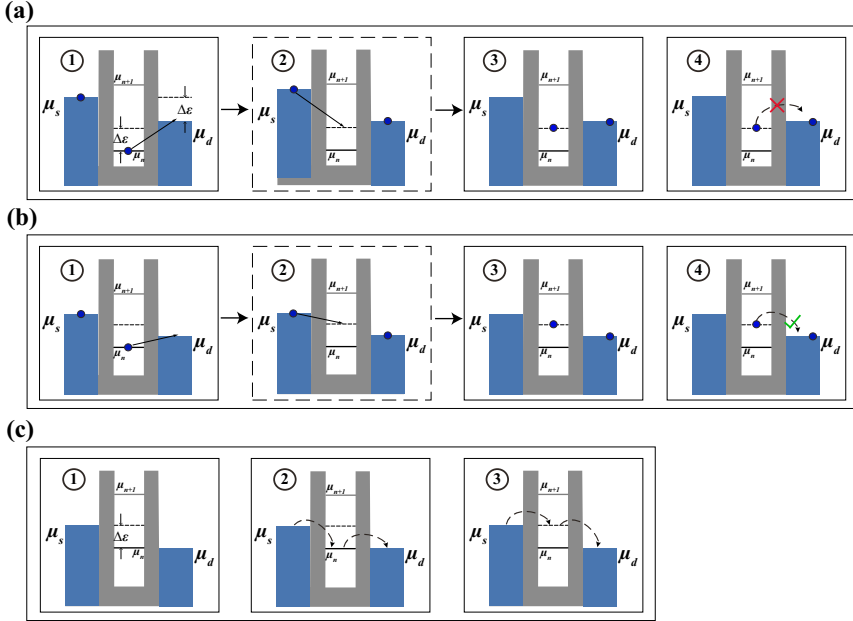
Figure 3.14: The schematic energy diagrams of the inelastic co-tunneling process. In the Coulomb blockade region, inelastic co-tunneling can occur under a certain bias voltage. Two electrons tunnel in and out of the dot simultaneously via a virtual state, the same as the elastic co-tunneling. The tunneling-out electron is from the ground state and the tunneling-in electron tunnels into the excited state. This leaves the dot in an excited state. The inelastic co-tunneling gives further conductance enhancement. (a) shows the inelastic co-tunneling that is not followed by CAST, while (b) shows the one followed by CAST. (c) displays the schematic energy diagrams corresponding to point D, where sequential electron tunneling via an excited state occurs.

be attributed to the sequential electron tunneling via the excited states of the quantum dot. In this case, both the ground state and the excited state are in the bias energy window, and thereby the incident electrons have two tunneling channels. Note that the tunneling is still sequential, i.e., electrons can only tunnel in/out of the dot one at a time. However, the presence of additional transport paths through excited states results in a differential conductance peak.

3.4.4 Spin-orbit interaction derived by inelastic co-tunneling spectrum

One of the important applications of the inelastic co-tunneling and the excited state spectroscopy is to analyze quantum levels of the dot. As an example, Fig. 3.15 displays the analysis of quantum level evolution in a magnetic field via the inelastic co-tunneling spectrum.

Figure 3.15 (a) shows the charge stability diagram measured for Dev. *NbInSbNb#1*. The inelastic co-tunneling differential conductance thresholds (blue lines) are evident in the Coulomb diamond between $V_{bg} = 4.05 \sim 4.15$ V (the dashed rectangle). From the above discussion, we know the onset of the inelastic co-tunneling is at $V_{sd}^T = \pm\Delta\epsilon/e$, in which $\Delta\epsilon$ is the excited state energy relative to the ground state or the energy difference between the two quantum levels. The linear-response conductance of the device is measured as a function of V_{bg} and the magnetic field B, as shown in Fig. 3.15 (b). The resonant levels corresponding to the squared Coulomb diamond are indicated by the two horizontal high conductance lines. They are from different orbital states and with opposite spins. Due to the Zeeman splitting, the ground state resonant levels shift significantly. We label the level spins using the arrows and denote the two levels by $|n, \downarrow\rangle$ and $|n + 1, \uparrow\rangle$, respectively. It is evident that state $|n, \downarrow\rangle$ and state $|n + 1, \uparrow\rangle$ shift toward each other from $B = 0$ T to $B = 1.3$ T, and swap their positions after $B = 1.3$ T. We cannot decide whether the two states cross or anti-cross at the swapping point because of the existence of the charging energy. However, the inelastic co-tunneling spectrum can avoid the influence of the charging energy. Figures 3.15 (c) and (d) show the differential conductance as a function of V_{sd} and B, on a color scale and line-cut plots, respectively. The V_{bg} is fixed at 4.1 V as indicated by the dashed lines in Figs. 3.15 (a) and (b). It can be seen that $\left|V_{sd}^T(B)\right|$ decreases from $B = 0.6$ T to $B = 1.3$ T and increases again when $B > 1.3$ T. However, $\left|V_{sd}^T(B)\right|$ never reaches zero, i.e., the two states $|n, \downarrow\rangle$ and $|n + 1, \uparrow\rangle$ do
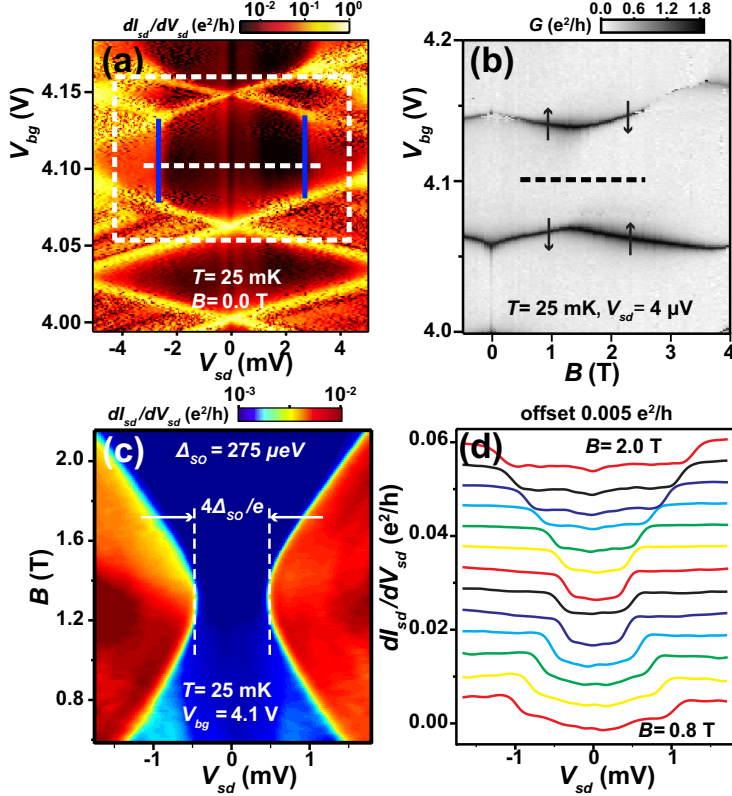
Figure 3.15: Inelastic co-tunneling spectrum in a magnetic field. (a) The charge stability diagram measured for Dev. *NbInSbNb#1*. The conductance thresholds corresponding to the onset of inelastic co-tunneling can be clearly seen in the Coulomb diamond between $V_{bg} = 4.05 \sim 4.15$ V. (b) The linear-response conductance measured for Dev. *NbInSbNb#1* as a function of V_{bg} and the magnetic field B. (c) Differential conductance measured for Dev. *NbInSbNb#1* as a function of V_{sd} and B, at $V_{bg} = 4.1$ V [the dashed line in panels (a) and (b)]. The shift of the inelastic co-tunneling threshold implies the evolution of quantum levels in the magnetic field. (d) Line-cut plot corresponding to panel (c).

not crossover at the swapping point. The minima of $\left|V_{sd}^T(B)\right|$ is around 550 μV.

The anti-crossing in Fig. 3.15 (c) is due to the *spin-orbit interaction* (28, 29). When an electron moves in an electric field, it will experience a magnetic field in its own rest reference frame according to the relativity theory. This magnetic field will act on the spin of the electron and induce the so-called spin-orbit interaction. In III-V semiconductors, both asymmetric crystal potential in materials (the Dresselhaus type) and the asymmetry of the electrical potential (the Rashba type) can cause the spin-orbit interaction. In Chapt. 5, we will see the spin-orbit interaction plays a critical role in the research of Majorana bound states. In Fig. 3.15 (c), the state $|n, \downarrow\rangle$ and the state $|n+1, \uparrow\rangle$ hybridize at $B = 1.3$ T and form an avoided level crossing. This anti-crossing indicates a mixing of the two orbitals stemming from spin-orbit interaction in the dot. The spin-orbit energy Δ_{so} can be estimated from the anti-crossing gap according to the relation $V_{sd}^T(B = 1.3T) \approx 2\Delta_{so}$. For the case in Fig. 3.15, Δ_{so} is about 275 μeV.

3.4.5 The Kondo effect in InSb nanowire quantum dot

The elastic co-tunneling or the inelastic co-tunneling is not spin-sensitive transport mechanism. However, when the spin is included, a new type of co-tunneling process can happen in the quantum dot system.

In the 1930s, researchers found that the resistance of metals containing some magnetic impurities increased below a critical temperature. The phenomenon was not explained until 1964 by Jun Kondo, who proposed it was caused by the scattering of the spins of the conducting electrons via the magnetic impurities (30). The effect is therefore called the *Kondo effect*. In the quantum dot system, the dot also behaves like a magnetic impurity when there is at least one unpaired spin on the dot (like the odd charged states for the cases above) (31). If the coupling between the dot and leads is strong enough, the interaction between the localized unpaired spin in the dot and the delocalized spin in the lead starts playing an important role [Figs. 3.16 (a) and (b)]. Since this interaction is similar to the spin-scattering interaction in the dilute magnetic alloys, it is also referred to as the Kondo effect.

Figures 3.16 (c)-(d) show schematic energy diagrams of a quantum dot which is in the Coulomb blockade configuration. A spin-degenerate quantum level of the dot is populated by a single spin. If the dot is strongly coupled to at least one of the surrounding leads, a correlation can occur between the unpaired spin
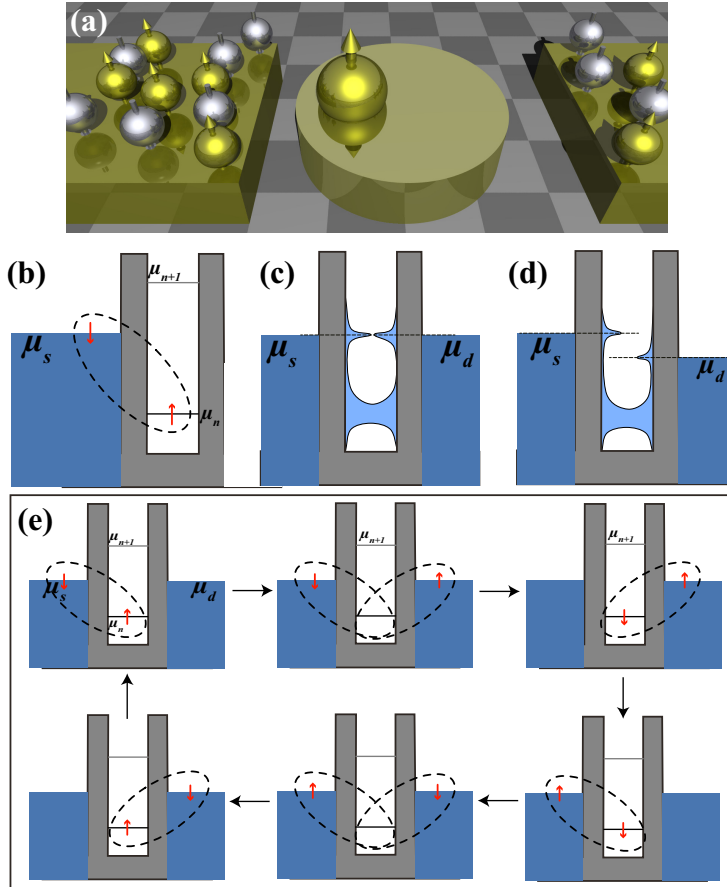
Figure 3.16: The Kondo effect in quantum dot systems. (a) A concept map showing the singlet state formed between the unpaired spin in the quantum dot and the delocalized spins in the leads. (b) Schematic energy diagram showing the formation of the Kondo singlet state in the quantum dot system. (c) and (d) reveal that the Kondo effect results in DOS peaks at the Fermi energies of the contacts at zero-bias voltage and finite-bias voltage, respectively. (e) Schematic energy diagrams show the spin-flip process in the quantum dot system caused by the Kondo effect.

on the dot and the delocalized spins on the leads, and form a spin-singlet state. From the point of view of the density of states (DOS), an extra DOS peak is formed in the dot at the Fermi energy of the contact (32, 33). These DOS peaks are illustrated in Figs. 3.16 (c) and (d).

In order to form the Kondo singlet state in the quantum dot system, two conditions have to be met. Firstly, the coupling between the dot and at least one of the surrounding leads has to be sufficiently strong to allow the correlation to occur. Secondly, the temperature has to be low enough to avoid destroying the spin singlet. The critical temperature below which the Kondo effect is visible is referred to as the *Kondo temperature* T_K. When a quantum dot is strongly coupled to contacts and is occupied by an unpaired spin, its conductance in the Coulomb blockade region will increase as the temperature drops down below T_K. This can be attributed to the formation of a DOS peak in the metal-dot system via magnetic-exchange coupling. Another transport feature of the Kondo effect in the quantum dot system is the emergence of a zero-bias differential conductance peak. At zero-bias voltage, the system gains greater density of states from the Fermi levels of both contacts and the two contacts get bridged with each other via the density of states. When the applied voltage is large, separating the Fermi levels in the two leads, the electrons at the Fermi level in the higher energy lead can no longer tunnel resonantly into the enhanced density of states in the lower energy lead. Therefore, a zero-bias differential conductance peak emerges at the Kondo regime.

The low-bias conductance enhancement mechanism can also be interpreted as the spin-flip assisted co-tunneling process (34). As shown in Fig. 3.16 (e), the localized electron may tunnel out of the dot to form an energetically forbidden virtual state for a short time. Simultaneously, a spin-down electron on the leads may tunnel into the dot. This co-tunneling process results in a coherent spin-flip of the localized electron on the dot. Actually, the spin-flip is indeed the physical manifestation of the time-averaged singlet state. At a small applied bias voltage, electrons can tunnel through the dot, mediated by the spin-flip process among the dot and two contacts. As a result, the Kondo effect leads to a much greater conductance enhancement than the normal elastic co-tunneling around zero-bias voltage. However, at a finite applied bias voltage, the source-dot spin-flip and drain-dot spin-flip become incoherent due to the energy difference. Again, a zero-bias differential conductance peak is developed.
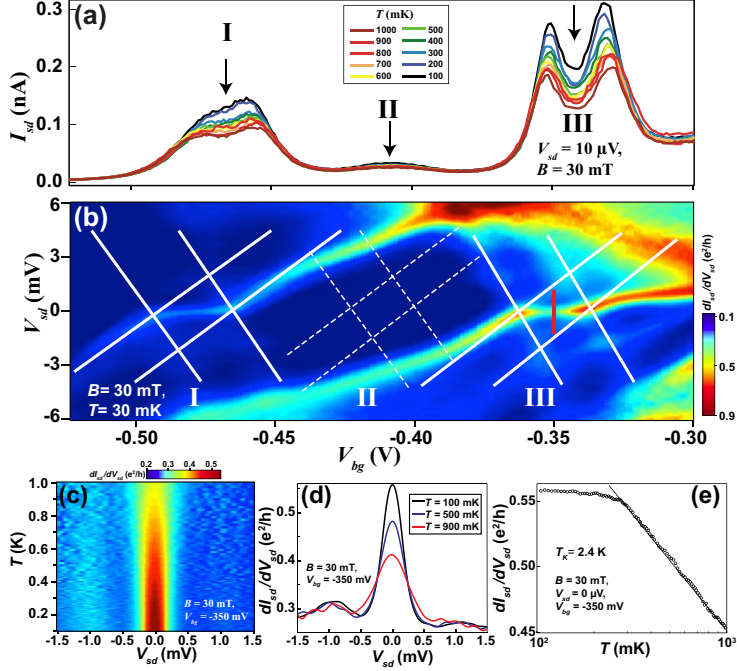
Figure 3.17: The Kondo effect in an Al-InSb nanowire quantum dot-Al device. (a) The measured source-drain current, I_{sd}, as a function of V_{bg}, at $V_{sd} = 10\mu V$ and $B = 30$ mT, measured for Dev. *AlInSbAl#2*. The temperature is varied between 100 mK to 1000 mK. It is evident that the current at the region indicated by arrows is higher at low temperature than at high temperature. (b) The charge stability diagram measured for the same device in the same V_{bg} region. The Coulomb diamonds structure is blurred because of the strong dot-leads coupling (life-time broadening). Solid lines are guiding lines indicating Coulomb diamond borders for diamonds **I** and **III**, and the dashed lines represent an estimated position for diamond **II** which is not visible due to the ultra low conductance there. According to the addition energies, we know diamonds **I-III** are odd-occupied diamonds. Zero-bias conductance peaks in diamonds **I** and **III** are clearly seen. (c) Differential conductance on a color scale as a function of V_{sd} and temperature T, at $V_{bg} = -350$ mV, measured for the device. (d) Three $dI_{sd}/dV_{sd} - V_{sd}$ line cuts taken from panel (c) at $T = 100, 500$ and 900 mK. From (c) and (d), we can see that the zero-bias conductance peak gets lower and broader as the temperature increases. (e) Zero-bias differential conductance as a function of T extracted from panel (c). The zero-bias conductance decreases as the temperature increases and shows a negative linear slope on the logarithmic temperature scale.

In Fig. 3.17, we show some transport features of the Kondo effect measured for an InSb nanowire quantum dot coupled to Al leads (Dev. *AlInSbAl#2*). Figure 3.17 (a) shows the measured source-drain current I_{sd} for the device, as a function of V_{bg}, at $V_{sd} = 10\mu$V and $B = 30$ mT[1]. The temperature is varied between 100 mK to 1000 mK. And Fig. 3.17 (b) displays the charge stability diagram corresponding to Fig. 3.17 (a). Due to the strong dot-leads coupling, Coulomb oscillation peaks and diamond structures are blurred. We use solid lines in Fig. 3.17 (b) as guiding lines for diamond structures. Regions **I-III** can be identified as odd-occupied diamonds according to their addition energies. Note that the conductance in diamond **II** is too weak to be seen and therefore we depict an estimated diamond using dashed lines. It is evident in Fig. 3.17, that the current in the Coulomb blockade regions of diamonds **I**, **II** and **III** decreases as the temperature increases. It is contradictory to the fact that the conductance in the blockade region should increase with rising temperature because of the thermal broadening of the resonant peaks. This anomalous temperature dependence can be attributed to the Kondo effect. As we mentioned above, due to the formation of a Kondo singlet state, the conductance of the quantum dot is enhanced at low temperature. However, the singlet state is gradually destroyed as the temperature increases and then the conductance decreases.

Besides the anomalous temperature dependence, the zero-bias conductance anomalies in diamonds **I** and **III** in Fig. 3.17 are also manifestations of the Kondo effect. The zero-bias anomaly is therefore called the Kondo peak or Kondo ridge. In Figs. 3.17 (c) and (d), we can see that the height of the Kondo ridge is lowered by increasing the temperature. In the logarithmic temperature scale, the zero-bias conductance shows a negative linear slope with temperature. This logarithmic temperature dependence is a typical feature of the Kondo effect. Note that there is a saturated region at the low temperature part, which is probably caused by a saturation of the electron temperature in the device.

The Kondo effect will be suppressed under the application of an external magnetic field. This is because the spin degeneracy is lifted by the Zeeman effect. As shown in Fig. 3.18 (a), the applied magnetic field splits the unpaired localized electron state into a Zeeman doublet separated by the energy $|g^*\mu_B B|$.

---

[1]At $B \geq 30$ mT or $T \geq 1$ K, the superconductivity of Al leads is suppressed and the device behaves just like normal metals coupled to the quantum dot. All the data concerned in this chapter for this device is taken either at $B \geq 30$ mT or $T \geq 1$ K
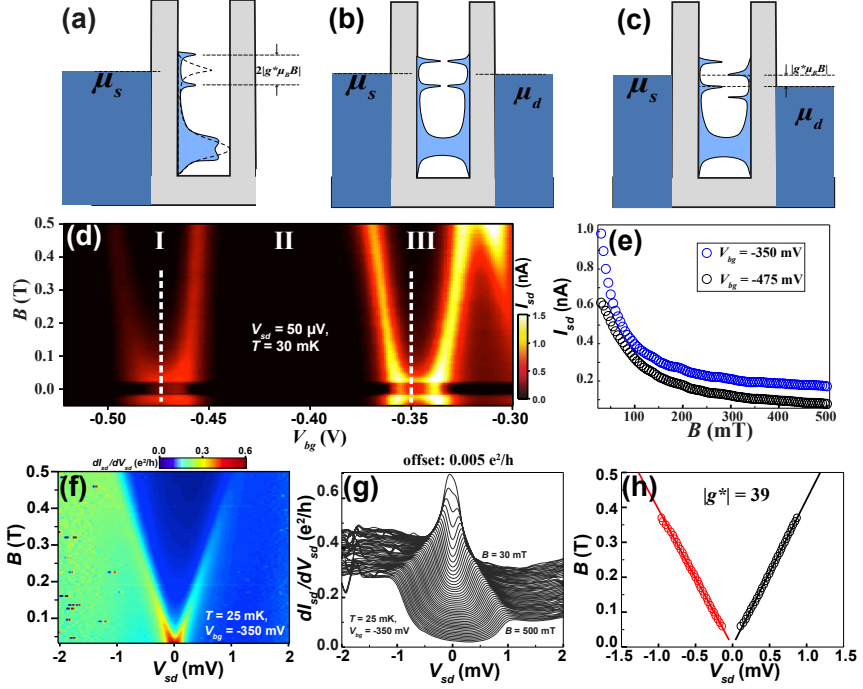
Figure 3.18: The Kondo effect in a magnetic field. (a) Schematic energy diagram of a quantum dot with split Kondo DOS peaks at the Fermi level. (b) The Kondo effect in the equilibrium regime in a magnetic field. The Kondo effect contributes very little to the conductance in linear-response regime. (c) The Kondo effect in the non-equilibrium regime. The Kondo effect induces two conductance peaks at $\pm eV_{sd} = |g^*\mu_B B|$ where the bias energy window covers one of the split Kondo DOS peak of each spin. (d) The low-bias source-drain current on a color scale, as a function of V_{bg} and magnetic field B. The resonant level shifting direction in the magnetic field proves diamonds **I** and **III** have odd-occupation, which is consistent with Fig. 3.17 (b). (e) The $I_{sd} - B$ relation taken from panel (d) along the dashed lines. From panels (d) and (e), it can be seen that the equilibrium conductance in diamonds **I** and **III** vanishes gradually in the magnetic field. (f) Differential conductance on a color scale as a function of V_{sd} and B at $V_{bg} = -350$ mV measured for the device. (g) The same with (f) but represented by a line-cut plot. The Kondo ridge splits into two peaks in the finite magnetic field separated by $2|g^*\mu_B B|/e$. (h) The linear fitting for the split Kondo peaks which gives the effective g-factor $|g^*| = 39$.

This also splits the enhanced density of states at the Fermi level into two peaks with energies $|g^*\mu_B B|$ above and below the Fermi level (35). The conductance enhancement in the equilibrium regime is then reduced. However, when the Fermi level of one lead is raised by a voltage $|g^*\mu_B B|/e$ relative to the other lead, the current-carrying window can cover one of the split Kondo DOS peaks of each spin, and thereby electrons can tunnel through the quantum dot.

Figure 3.18 (d) displays the low-bias source-drain current on a color scale, as a function of V_{bg} and magnetic field B. From the shifting direction of the resonant levels in the magnetic field, we can also decide that diamonds **I** and **III** have odd-occupations, which is consistent with Fig. 3.17 (b). Note that there is a sharp low-conductance gap in the low field region, which is caused by the superconductivity in Al leads and will be discussed in Chapt. 4. In Fig. 3.18 (e), two $I_{sd}-B$ curves are shown, which are taken from Fig. 3.18 (d) where the Kondo effect occurs at a low magnetic field (along the dashed lines). It is clear that the conductance enhancement induced by the Kondo effect in the equilibrium regime decreases as the magnetic field increases. In Fig. 3.18 (f) and (g), two conductance peaks at $\pm V_{sd} = |g^*\mu_B B|/e$ emerge. These are the split Kondo peaks in the non-equilibrium regime, and they are separated by $2|g^*\mu_B B|/e$. By linear fitting of the split Kondo peaks, the effective g-factor can be calculated. Fig. 3.18 gives the effective g-factor here as about -39.

At high magnetic fields, the Kondo effect will almostly disappear, and the Kondo peak will evolve smoothly into a co-tunneling threshold (36).

3.5 Derivation of effective g-factor for InSb quantum dot with Kondo effect

So far, we have discussed two methods that can be employed for estimating effective g-factors of InSb quantum dot devices. They are the electron addition spectroscopy based g-factor derivation (Fig.3.11) and the Kondo splitting based derivation. However, both methods could give a wrong estimation of the g-factor of an InSb quantum dot in the presence of a strong Kondo effect.

Figure 3.19 (a) displays linear fittings for resonant level positions on the scale of V_{bg}, for the state $|1, \uparrow\rangle$ and the state $|1, \downarrow\rangle$ of Dev. *AlInSbAl#1*. The inset is the linear-response conductance on a color scale as a function of V_{bg} and B. As we discussed in the section of the Zeeman effect, the two resonant levels

Figure 3.19: The electron addition spectroscopy based g-factor derivation may lead an over-estimated g-factor. Experimental data is taken from measurement results of Dev. *AlInSbAl#1*. (a) The linear fits for the two resonant levels, corresponding to spin-states for the range $B = 0.2 \sim 0.5$ T. The inset is the linear-response conductance on a color scale as a function of V_{bg} and B. The two resonant levels split due to the Zeeman effect, and the g-factor can be calculated to be $|g^*| = 72$ according to Eq. 3.11. (b) The differential g-factor as a function of B, derived from the electron addition spectroscopy. (c) The linear-response conductance as a function of V_{bg} at different temperatures. The inset is the corresponded colormap. It is evident that the resonant levels show a visual splitting tendency as the temperature rises. (d) Schematic diagrams show how a Kondo DOS peak complicates the derivation of correct addition energy.

split due to the Zeeman effect, and the g-factor can be calculated according to $E_z(B) = |g^*| \mu_B B$. The Zeeman energy is determined by the change of the addition energy $E_z(B) = \Delta E(B) - \Delta E(0)$. The addition energy can be extracted by $\Delta E(B) = \alpha_{bg} \Delta V_{bg}(B)$, in which ΔV_{bg} is the peak separation on the scale of back gate voltage and α_{bg} is the lever arm. For the range of $B = 0.2 \sim 0.5$ T, the g-factor is decided to be $|g^*| = 72$.

We can also derive the effective g-factor differentially, using $|g'| = \frac{1}{\mu_B} dE_z(B)/dB$. Figure 3.19 (b) shows $|g'|$ as a function of B, derived from the electron addition spectroscopy. Surprisingly, the differential g-factor varies greatly with the change of magnetic field, instead of being a constant.

To explain this result, we plot a T-version electron addition spectroscopy in Fig. 3.19 (c), i.e., the linear-response conductance as a function of V_{bg} and
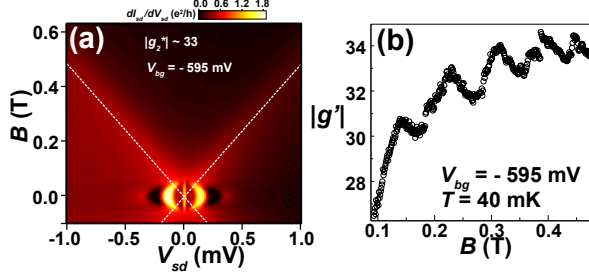
Figure 3.20: The Kondo splitting based g-factor derivation may lead to an underestimated g-factor. (a) Differential conductance on a color scale as a function of V_{sd} and B. The split Kondo peaks are indicated by the dashed lines. (b) The differential g-factor as a function of B, derived from the Kondo splitting.

temperature T. One may predict that the resonant levels will get broader but keep their positions on the scale of V_{bg} if only considering thermal broadening effect. However, it is evident that the resonant levels show a visual splitting tendency as the temperature rises. We propose a possible interpretation as shown in Fig. 3.19 (d). With a large Kondo DOS peak at the Fermi level, the conductance maxima points do not align with the intrinsic charging levels. In the vicinity of the Kondo DOS peak, the probed conductance peak shifts towards the Fermi level and gives a false addition energy ΔE^* that is smaller than ΔE. Once the Kondo effect is suppressed by the temperature rising or the application of a magnetic field, this conductance peak will shift back to the intrinsic charging level position and thereby ΔE^* approaches ΔE. This will cause a visual level splitting as T rises and causes an extra splitting beside the Zeeman splitting in the magnetic field. The extra splitting of the conductance peaks results in an overestimated g-factor.

Compared to the addition energy spectroscopy, the Kondo splitting or inelastic co-tunneling method is more precise than electron addition spectroscopy. This is because the co-tunneling spectrum is independent of chemical potential of the dot, making the splitting immune to small charge fluctuations near the quantum dot. The g-factor measurements can be done in the regime far away from charging levels and therefore avoid the above mentioned problem. Additionally, the Kondo splitting or co-tunneling method is inherently more precise because the intrinsic width of the Kondo peak is smaller than the width of the charging peak.

Figure 3.20 shows the Kondo splitting based g-factor calculation, derived for

the same device as in Fig. 3.19. The split Kondo peaks can be seen in Fig. 3.20 (a) (indicated by the dashed lines). By linear fitting of the Kondo peaks, the effective g-factor can be decided to be $|g^*| = 33$. We can also derive the differential g-factor as we have done in Fig. 3.19 (b). The results are shown in Fig. 3.20 (b). Again, the differential g-factor is not constant, but shows an increase with small fluctuations in the range of $B = 0.1 \sim 0.5$ T. This g-factor puzzle results from the non-linear splitting of the Kondo peak. This is consistent with the theoretical literature which predicts that the low-field Kondo splitting can be reduced down to $4/3 \, |g^*| \, \mu_B B$ due to the attraction of the Kondo resonance to the Fermi level (37, 38). Reference (39) shows a similar observation.

Above all, the derivation of the effective g-factor for a quantum dot with a strong Kondo effect can be very delicate. For the cases in Fig. 3.19, the calculated effective g-factor can be twice as high as the one derived in Fig. 3.20. Although the differential g-factors from both derivation methods will converge to the correct value at high field, the risk of field induced orbital effects grow.

3.6 Features of quasi-1D DOS of the reservoirs

As discussed earlier, the bias spectroscopy needs charge carriers on both sides of the dot in order to probe the quantum states in the dot. The properties of these reservoirs will strongly influence the behaviour of the device, and in some cases manifest themselves as the origin of some transport features.

In the above discussion, contacts of quantum dots are all assumed to be metallic leads with constant and large DOS at their Fermi levels. However, in some cases, the carrier reservoirs can not be treated as a vast Fermi sea. Instead, nonlinear leads DOS of the leads with singularities could rise up from dimensionality, superconductivity or surface state topology. As an example, here we discuss a transport feature in the tunneling spectroscopy of an InSb quantum dot device, induced by quasi-1D dimensionality of leads induced . Tunneling features related to superconductivity and surface state topology will be studied in Chapt. 4 and Chapt. 5, respectively.

For some quantum dots, confined in 2D semiconductor inversion layers (2 dimensional electron gas, 2DEG), their source/drain reservoirs are electrostatically induced two-dimensional charge layer. Due to the small effective electron mass in the semiconductor and the 2D confinement, the DOS of the source/drain

reservoirs are modulated into sub-band structures. These singularities of the lead states will induce additional densely spaced peaks and dips in the differential conductance in the charge stability diagrams (40). One might think that for nanowire quantum dots contacted by metal leads, these lead states are not visible due to the non-fluctuating density of states of the metal contact. However, we observed evident lead state features in the measurements shown below.

Figure 3.21 shows charge stability diagrams measured for the p-type region of Dev. *NbInSbNb#1*, corresponding to Fig. 3.10 (c). The full-scale diagram is split into two parts and are displayed in Figs. 3.21 (a) and (b) respectively. It can be seen that the Coulomb diamond structures are sharp and have regular sizes. All the diamonds have almost the same addition energies around 4.5 meV. This is consistent with the Coulomb oscillation in Fig. 3.10 (c). The close-up views in Figs. 3.21 (c) and (d) show that there is an extra high differential conductance line outside of each diamond [labeled by black solid circles in Figs. 3.21 (c) and (d)]. These high conductance lines are similar to the sequential tunneling via excited states. However, as we have discussed, the quantization energies of the dot in this V_{bg} region are much smaller than the energy derived from the excited states. Figure 3.21 (e) shows a differential conductance line-cut taken in Fig. 3.21 (d) along the dashed line, in which the anomalously high conductance line corresponded to dI/dV peak is high and sharp.

The transport features shown in Fig. 3.21 are similar to the lead state features of the quantum dot confined in the 2DEG. Actually, the anomalously high conductance lines in the p-type InSb nanowire quantum dot have been reported by Pribiag et al (16). In Ref. (16), the origin of this conductance was decided to be lead-states instead of the excited states of the dot, relying on the large difference between the effective g-factors of InSb electrons and holes.

Figure 3.22 (a) shows the SEM image of Dev. *NbInSbNb#1*, and Fig. 3.22 (b) depicts the schematic band diagram of the device. It can be seen that the real, or direct, carrier reservoirs of the quantum dot are the InSb nanowire segments covered by the metal. Due to different electric field screening effects from metal electrodes, the metal covered nanowire segments are still in the n-type region, although the dot is already tuned to p-type. The tunneling barriers of the p-type dot are formed by the bent band gap of InSb semiconductor nanowire. Therefore, the carrier reservoirs have quasi-1D DOS as shown in Figs. 3.22 (c) and (d). When the resonant-tunneling window of the dot is aligned with the DOS singularities
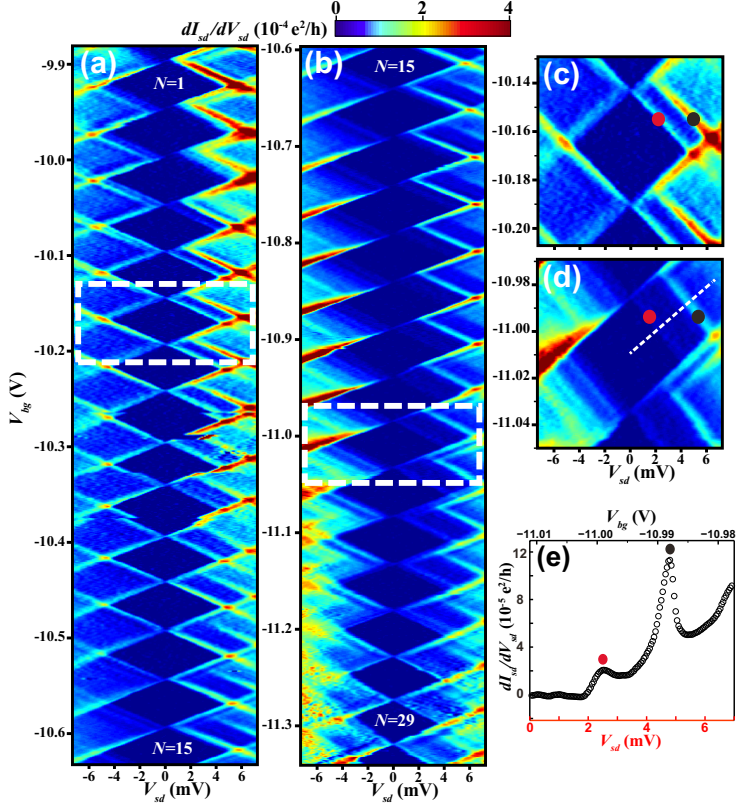
Figure 3.21: The lead states in an InSb nanowire quantum dot device. (a)-(d) Charge stability diagrams measured for Dev. *NbInSbNb#1*. The full-scale diagram is split into two parts that are shown in panels (a) and (b). (c) and (d) are close-up views of the dashed rectangles in panels (a) and (b), respectively. (e) The differential conductance line-cut along the dashed line in panel (d).

in the n-type nanowire leads, a high conductance peak will develop.

Although the potential tuning efficiency of the back gate to n-type leads is much weaker than the tuning efficiency to the p-type dot, the Fermi levels of the nanowire leads can still be tuned by the back gate [Fig. 3.22 (e)]. That means the DOS singularity energy ΔE_N of the Nth sub-band relative to the Fermi level will change from diamond to diamond, and ΔE_N can be deduced from the peak distances as in Fig. 3.21 (e). Figure 3.22 (f) shows the extracted average values of ΔE_N in each diamond, as a function of order number of the dot [assigned as in Fig. 3.21 (a) and (b)]. We can see that ΔE_N does indeed change linearly with hole numbers and therefore with V_{bg}. Moreover, it is evident that there are two DOS singularity features in diamonds 9∼16. By linear fitting for ΔE_N and ΔE_{N-1}, the energy difference between the Nth sub-band and the $(N-1)$th sub-band can be determined to be about 2.1±0.1 meV. The linear change of the position of the anomalous conductance peak provides a strong evidence of lead states. It also proves the chemical potential of leads can be adjusted by back gate voltage inspite of electrical field screening from metal electrodes.
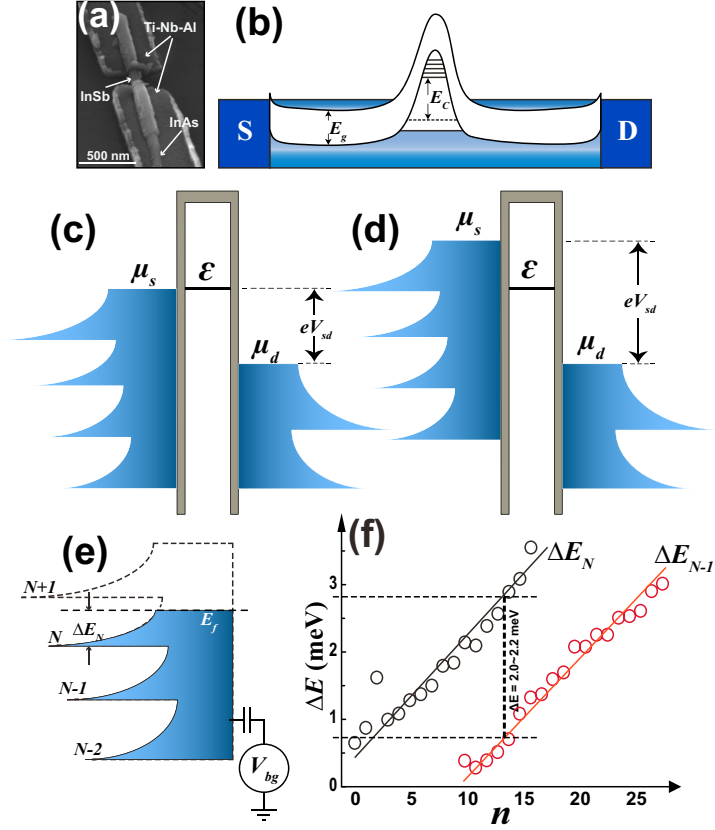
Figure 3.22: Quasi 1D density of states in the leads of the InSb nanowire quantum dot. (a) SEM image of Dev. *NbInSbNb#1.* (b) Schematic band diagram for p-type region of Dev. *NbInSbNb#1.* The potential barriers of the quantum dot are formed by the bent band gap of the InSb nanowire. (c) and (d) Schematic energy diagrams of the device with quasi 1D DOS in the leads. (e) The chemical potential of the leads can be tuned by the gate. (f) The energy of the DOS singularity relative to the Fermi level as a function of the order number of the diamonds.

4

Superconductor Coupled InSb Nanowire Quantum Dots

In Chapt. 3, we discussed the transport features of InSb quantum dots with normal metal leads (or with superconductor leads but in their normal state). Superconductor coupled quantum dot systems are also interesting and have promising application in building quantum computers. In this chapter, we will discuss several new transport phenomena that rise in the superconductor-InSb nanowire quantum dot-superconductor systems.

4.1   Introduction of superconductivity

Superconductivity was discovered by H. K. Onnes in 1911 (41), when he measured the resistance of mercury (Hg). Onnes found that the mercury resistance suddenly dropped to zero when the temperature was below 4 K. Soon afterwards, Onnes and other researchers found that the sharp resistance drop also occured for some other metals when they were cooled below certain temperatures. These metals are called *superconductors*. In Fig. 4.1, we show the resistance measured for a small piece of TiNbAl (3/85/5 nm) metal as a function of temperature. The metal resistance drops to zero at $T \approx 7$ K, indicating TiNbAl transform to a superconducting state. The temperature at which the transition between the normal state and the superconducting state occurs is called the *critical temperature* of the superconductor, and is denoted by T_c. For example, T_c of Hg is 4 K and T_c of the TiNbAl thin layer in Fig. 4.1 is 7.5 K. Normally, the values of T_c are significantly lower than room temperature. However, with the continuous
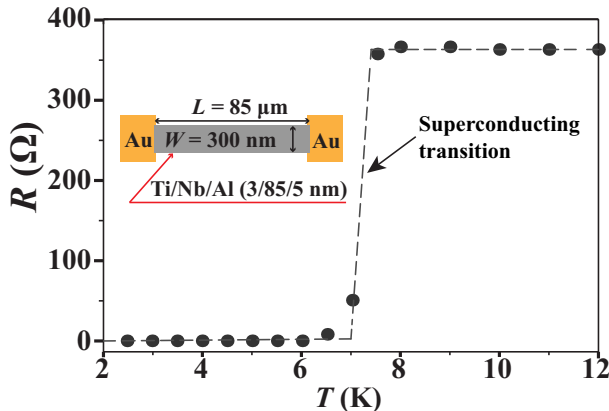
Figure 4.1: Resistance measured for a piece of TiNbAl (3/85/5 nm) metal as a function of temperature. The metal resistance drops to zero at $T \approx 7.5$ K because it transforms to a superconducting state when $T < T_c$. The inset is the schematic layout of the measured metal piece.

efforts spent on searching for high-T_c superconductor materials, the records of the highest T_c have over the decades been frequently broken and T_c is gradually approaching the room temperature (42).

Besides the zero resistance, a superconductor has another important property, which is described as an expulsion of a magnetic field from the superconductor during its transition to the superconducting state. This phenomenon is called the *Meissner effect* (43). Note that the Messiner effect is an intrinsic property of superconductors, and cannot be explained merely by zero resistance. However, the external magnetic field can also quench the superconductivity after it reaches a certain strength. The magnetic field at which the superconductivity vanishes is called the *critical magnetic field B_c*.

4.1.1 The BCS theory of superconductivity

Although the experimental studies and phenomenological understandings about superconductivity developed rapidly in the earlier days, no comprehensive microscopic theory was proposed until J. Bardeen, L.N. Cooper and J.R. Schrieffer suggested an electron pairing mechanism in 1957 (44). Their microscopic interpretation of superconductivity is referred to as the *BCS theory*.

We know the electrical resistance of a metal arises from the scattering of the conduction electrons. However, the BCS theory pointed out that the charge carriers in superconductors are electron pairs, or the so-called *Cooper pairs*. The Cooper pairs cannot be scattered unless the pairing is broken, and thereby the scattering-free motion of the Cooper pairs result in the zero resistance of superconductors. However, how can electrons be paired up with mutual Coloumb repulsion? The key point of the Cooper pair formation is the electron attraction mediated by the electron-phonon interaction. Shown in Fig. 4.2 (a), a conduction electron moving in a conductor will stir a charge fluctuation and ionic vibration of the lattice in the near vicinity of the electron. The positively charged ions tend to accumulate around the electron, forming a screening cloud of positive charge around the electron. A second electron nearby can be attracted into this region of higher positive charge density. With a coherent phase, the charge fluctuations and ionic vibrations can overwhelm the Coulombic repulsion between the two electrons and they are attracted to each other by their screening clouds. In the terms of quasi-particles, the two electrons are bonded together by exchanging virtual phonons: one emits a phonon and the other one absorbs it. The average maximum distance at which this phonon-coupled interaction takes place in the formation of a Cooper pair is called the *coherence length ξ*.

Because of the Pauli exclusion principle, only electrons with opposite spins can be paired together[1]. This means the pair has zero spin and is thereby a boson.

The electron pairing causes dramatic changes of conductor properties. Firstly, the bosonization of the electron pairing lowers the energy of the electrons into a giant quantum state with a macroscopic phase. Note that the pairing of two electrons is transient and transitions of electrons from pair to pair occur frequently. The fabric-like pairing bonds a huge number of electrons on a condensed state. This condensed bosonic state is immune to weak scattering, because the scattering of one single pair requires the change of the entire macroscopic state and needs a large energy. Secondly, the electron pairing opens up an energy gap Δ above and below the Fermi level, as shown in Fig.4.2 (b). Unbound electrons and holes, or the so-called *quasi-particles*, are separated from the macroscopic state of condensed Cooper pairs by Δ and can only exist outside the superconduct-

---

[1]Strictly speaking, either electrons with opposite spin momentums (s-wave superconductor) or opposite orbit momentums (p-wave superconductor) can be paired up.

ing gap. Therefore, an energy larger than 2Δ is required to split a Cooper pair and excite the electrons from the Fermi level to the next available state. Above all, the motion of the Cooper pair is dissipationless and therefore the electrical resistance of a superconductor is zero.

The superconducting energy gap in the DOS near the Fermi level is the critical feature of superconductivity. The magnitude of Δ represents how large the pairing potential is or how much energy is needed to break a Cooper pair. It also determines how high the critical temperature can be by the relation $2\Delta \approx 3.5 k_B T_c$. Δ decreases as T or B increases, and approximate estimations of $\Delta - T$ and $\Delta - B$ relations are given by equation group 4.1.

$$\begin{cases} \Delta\left(T\right) = \Delta_0 \sqrt{\cos\left[\frac{\pi}{2}(T/T_c)^2\right]} \\ \Delta\left(B\right) = \Delta_0 \sqrt{1 - (B/B_c)^2} \end{cases} \tag{4.1}$$

As shown in Fig. 4.2 (b), the DOS outside of Δ is no longer constant. Instead, there are two singularities near $E = \pm\Delta$. The DOS of a superconductor can be written as:

$$\frac{\mathcal{N}_s\left(E\right)}{\mathcal{N}_n\left(E\right)} = \begin{cases} \frac{E}{\sqrt{E^2 - \Delta^2}} & E > \Delta \\ 0 & E < \Delta \end{cases} \tag{4.2}$$

where $\mathcal{N}_n(E)$ is the DOS when the metal is in the normal state.

4.1.2 Superconductivity of Nb thin film

As an example, we discuss more details about the superconductivity of the TiNbAl thin film device shown in Fig.4.1. This device consists of a 85 μm long and 300 nm wide Ti/Nb/Al (3/85/5 nm) thin film connected to Au contacts. The device is measured in a ^4He cryostat with a base temperature of 2 K using a current bias setup. Although the device here is a trilayer thin film, its superconductivity is mainly decided by Nb. The thin Ti layer is used as the adhesion layer and the Al layer is used to protect Nb from oxidation.

Differing from Hg and Al, Nb is a *type-II superconductor*. Type II superconductors show two critical magnetic field values, one at the onset of a mixed superconducting and normal state (the *lower critical magnetic field B_{c1}*) and one where the superconductivity ceases (the *upper critical magnetic field B_{c2}*) (45). When the applied field is lower than B_{c1}, the superconductor behaves the same as type-I superconductor and repulses magnetic flux entry. In the mixed state,

(a)　　　　　　**(b)**
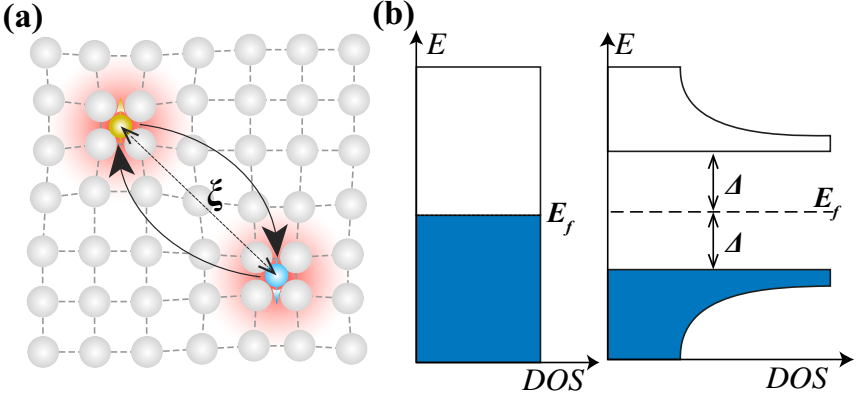
Figure 4.2: The BCS theory on superconductivity. (a) Schematic sketch of the formation of Cooper pairs in a superconductor. Two electrons with opposite momentums and spins are bonded together via electron-phonon-electron interaction. (b) The superconductivity modulation of the DOS of the metal. The electron pairing opens up an energy gap at the Fermi level.

magnetic fluxes can penetrate the superconductor through *vortices*. Each vortex carries a quantum of flux $\Phi_0 = h/2e$ and is concentrated toward its normal state center by circling Cooper pairs (46). Vortices are pinned to pinning centers (such as impurities, defects or geometry irregularities, note that each vortex is also constrained by the repulsion forces from neighboring vortices so that the overall lattice energy of the vortices is the lowest) at first, and therefore they cannot move or contribute any dissipative current. However, as the magnetic field increases, the density of vortices increases. The supercurrent is squeezed into a smaller space resulting in an increase of the local supercurrent density J. Therefore, the Lorenz force $f_L = J \times \Phi_0$ increases and finally conquers the pinning forces (47). Vortices then start moving and producing non-zero resistivity. The field at which vortices begin to move is called the *irreversibility field* B_{irr}. If the magnetic field increases further to B_{c2}, the overlapping of vortices occurs and the superconductivity is completely washed out.

Figure 4.3 (a) shows the measured source-drain voltage drop on the device V_{sd}, as a function of the applied source-drain current I_{sd}, at $T = 3$ K and $B = 0$ T. Here, the measured voltages for both current sweep directions are plotted, where the solid curve is for the upward current sweep (from negative I_{sd} to positive I_{sd})
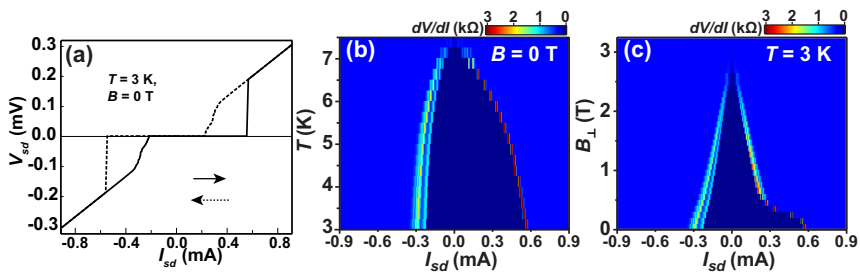
Figure 4.3: (a) Source-drain voltage V_{sd} measured for the device as a function of applied source-drain current I_{sd} at $T = 3$ K and $B = 0$ T. The solid curve is recorded in the upward current sweeping direction and the dashed curve in the downward current sweeping direction. (b) Differential resistance on a color scale measured for the device at zero magnetic field, as a function of I_{sd} and temperature T. (c) Differential resistance measured for the device at $T = 3$ K as a function of I_{sd} and a magnetic field $B_\perp$, applied perpendicularly (to the plane of the Nb thin film).

and the dashed curve is for the downward current sweep. It can be seen that there is a flat part in each of the curves, which indicates that the voltage drop is zero and the thin film is in a superconducting state. However, when the applied current is increased to a certain value, the current becomes dissipative. This is because the superconductor can only hold a disspationless supercurrent with limited magnitude. The upper limit of the supercurrent allowed to flow through the superconductor is called the *critical current* I_c. Beyond I_c, the kinetic energy of the superconducting carriers exceeds the binding energy of the Cooper pairs, and thereby quenches the superconductivity (48).

In Fig. 4.3 (a), the switching between the supercurrent branch and the dissipative branch shows a typical hysteretic behavior, i.e., the upward current sweep gives a different critical current from the downward current sweep. (49). The hysteretic I-V curve could be the result of phase instability normally found in a capacitively and resistively shunted nanoscale superconductor or Josephson junction (see definition later), or simply due to a heating effect.

Figure 4.3 (b) displays the differential resistance dV_{sd}/dI_{sd} on a color scale measured for the device, as a function of I_{sd} and temperature T. The bias current is swept from negative to positive values. The dark blue region corresponds to the region where the thin film is in the superconducting state and a supercurrent flows through the film. In the slightly lighter blue region, the thin film is in the normal,
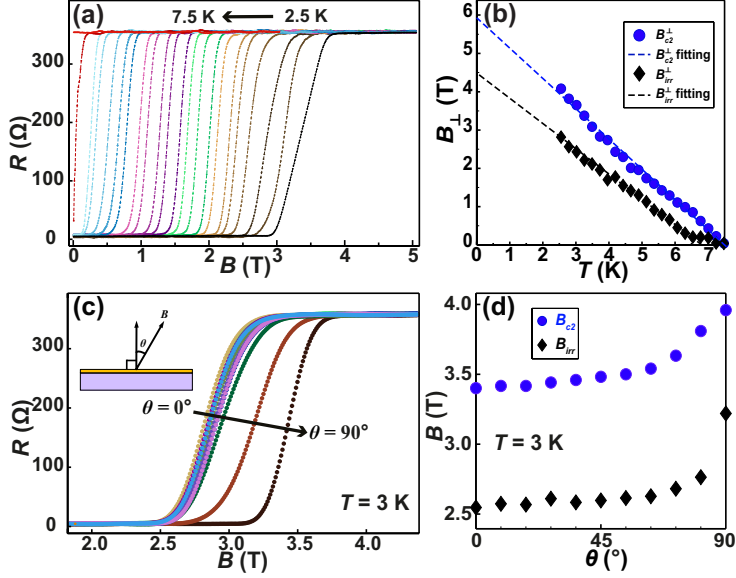
Figure 4.4: (a) Resistance measured for the device as a function of the perpendicularly applied magnetic field $B_\perp$ at different temperatures $T = 2.5 - 7.5$ K and at $I_{sd} = 5$ nA. (b) The upper critical magnetic field $B_{c2}^\perp$ and the irreversibility field $B_{irr}^\perp$ as a function of T, extracted from panel (a). (c) Resistance measured for the device as a function of the angle θ between the direction of the applied magnetic field and the axis normal to the substrate (indicated by the schematic inset), at $T = 3$ K and at $I_{sd} = 5$ nA. (d) The upper critical magnetic field B_{c2} and the irreversibility field B_{irr} as a function of θ, extracted from panel (c).

resistive state. The peak in the differential resistance at positive and negative bias currents signals a transition between the superconducting state and the normal state at the value of the critical supercurrent I_c. The temperature dependence measurements show that I_c decreases as T increases, and I_c vanishes around $T = 7.5$ K. Thereby, the critical temperature of the metal can be determined to be $T_c \approx 7.5$ K. Figure 4.3 (c) shows the dV_{sd}/dI_{sd} color scale as a function of I_{sd} and the perpendicularly applied magnetic field $B_\perp$. It can be seen that I_c decrease quickly with the increase of $B_\perp$, and I_c goes to zero around $B_\perp = 3$ T. Therefore, the upper critical magnetic field of the thin film at $T = 3$ K is 3 T.

Figure 4.4 (a) shows the resistance R measured for the device as a function of

$B_\perp$ at different temperatures from 2.5 K to 7.5 K and at $I_{sd} = 5$ nA. At $T = 2.5$ K, R remains around 0 below $B_\perp = 3$ T. R starts to increase at $B_\perp = 3$ T, indicating that the flux lines in the thin film begins to move. We take the transition magnetic field at which R jumps from 0 to finite value as the irreversibility field $B_{irr}^\perp$, and it can be used as the estimation of the upper-limit for the lower critical field $B_{c1}^\perp$ of type II superconductors. When the magnetic field exceeds $B_{irr}^\perp$, R increases steeply to a large value and then gradually approaches the normal state resistance value R_n. We define the magnetic field at which $R = R_n$ as the upper critical field value of $B_{c2}^\perp$, i.e., the thin film completely turns to its normal state when $B_\perp > B_{c2}^\perp$. For the $R - B_\perp$ curve measured at $T = 2.5$ K, we can deduce that $B_{irr}^\perp = 2.9$ T and $B_{c2}^\perp = 4.1$ T. As the temperature increases, both $B_{irr}^\perp$ and $B_{c2}^\perp$ decrease and finally become zero at the critical temperature $T_c = 7.5$ K. We extracted the values of $B_{irr}^\perp$ and $B_{c2}^\perp$ for all the curves in Fig. 4.4 (a) and plot them as a function of T (the $B_\perp - T$ phase diagram) in Fig. 4.4 (b). It can be seen that both $B_{irr}^\perp$ and $B_{c2}^\perp$ vary linearly as T changes, and this is consistent with the theoretical prediction for granular type II thin films and consistent with experimental results reported in ref (50). By linear fit for the $B_\perp - T$ phase diagram, we can extrapolate the values of $B_{irr}^\perp$ and $B_{c2}^\perp$ near zero temperature. The estimated $B_{irr}^\perp$ and $B_{c2}^\perp$ values at $T = 300$ mK are 4.2 T and 5.8 T respectively, and they are almost the same as the values measured for a Ti/Nb/Ti thin film device in ref (51).

We also performed magnetic field angle dependent measurements at $T = 3$ K. Figure 4.4 (c) shows the resistance R measured for the device as function of B at different field orientations (see the angle θ definition in the schematic inset of figure 4.4 (c) and at $I_{sd} = 5$ nA. The magnetoresistance measurements show that B_{irr} and B_{c2} are both anisotropic with respect to the magnetic field orientations. The values of B_{irr} and B_{c2} have their minimums at $\theta = 0°$ (perpendicular field) whereas they peak at $\theta = 90°$ (parallel field), and the differences between maximums and minimums are about 0.6 T and 0.5 T, respectively. The magnetoresistance anisotropy of B_{irr} and B_{c2} can be attributed to the anisotropy of diamagnetic energy for a given magnetic field (45). The anisotropy only occurs when the thickness of the thin film is smaller than or comparable with the penetration depth λ of the superconductor. Considering that the thickness of our device is $d = 93$ nm and the deduced penetration depth is $\lambda_L = 115$ nm (52), our measurement results are thereby reasonable.

4.2 Probing superconductor density of states with an InSb nanowire quantum dot

We have discussed the dissipationless supercurrent measurements through a superconductor in the previous section. Here, we show the direct probing of the superconductor DOS by transport measurements. The idea is similar to the probing of quasi-1D leads state in Chapt. 3, i.e., via the sharp resonant level of a quantum dot.

The device studied here is Dev. *AlInSbAl#1* which has been described in the previous chapter. Figure 4.5 (a) displays the schematic band diagram of this device. Under an applied negative global back-gate voltage, the quantum dot is inversed from n-type to p-type, while the metal covered nanowire segments remain n-type due to the electrical field screening from the Al electrodes. The barriers of the dot are formed by the bent band gap of the InSb nanowire.

We have shown the ambipolar transport features of this device in an earlier part. In the p-type transport region, some anomalous features arise due to the superconductivity of the Al contacts. As shown in Fig. 4.5 (b), there is a sharp current peak shooting up in each of the $I-V$ curves at the edges of the Coulomb staircase. These current spikes in $I-V$ curves can be explained as the BCS-DOS distribution $\mathcal{N}_s$ in the superconductor contacts[Fig. 4.5 (c)]. Because of the extremely weak coupling in the p-type dot region, the tunneling rate is the choke point of the current flow. The frequency of the tunneling event is proportional to the DOS of the quasi-particles in the reservoirs. Therefore, the tunneling current peaks when the resonant level in the quantum dot is aligned with one or two BCS-DOS singularities (53).

The current spikes result in a negative differential conductance (NDC) in the dI_{sd}/dV_{sd} charge stability diagram. This BCS-DOS singularity induced NDC has been observed in semiconductor nanowire quantum dots with superconductor leads by Doh et al (54). Differing from the smooth NDC hills in previous similar work, the current peaks here are much sharper and have a needle shape. The average full width at half maximum (FWHM) of the current peaks is only 40 μeV, while the maximum current can reach $2-3$ times higher than the flat part. This inspired us to make it a powerful BCS-DOS research method with ultra high resolution. Probed by the hyper-sharp resonant quantum level, BCS-DOS at different magnetic fields and various temperatures can be probed precisely and
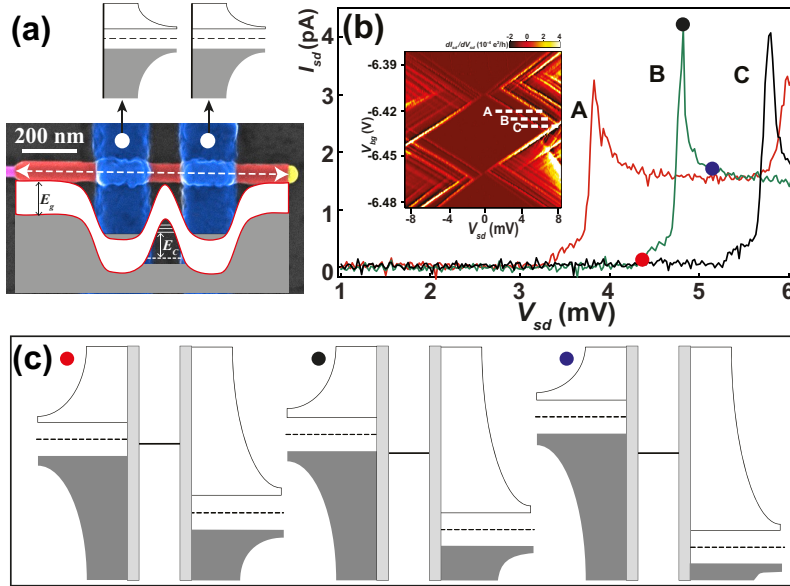
Figure 4.5: Anomalous current spikes in the $I - V$ curves of an Al coupled InSb nanowire quantum dot. (a) Schematic band diagram of Dev. *AlInSbAl#1*, including an SEM image. A p-type quantum dot is defined by the bent band gap of the InSb nanowire. Al is superconducting below 1 K. (b) The source-drain current in the hole transport region as a function of V_{sd}. Curves with different colors are taken at different V_{bg}. A very sharp current peak appears at each edge of the Coulomb staircase which can be attributed to the BCS density of state singularity in the superconductor contact. The inset is the corresponding Coulomb diamond in the charge stability diagram. (c) Schematic energy diagram of the device show the dot configuration at different source-drain bias voltages.
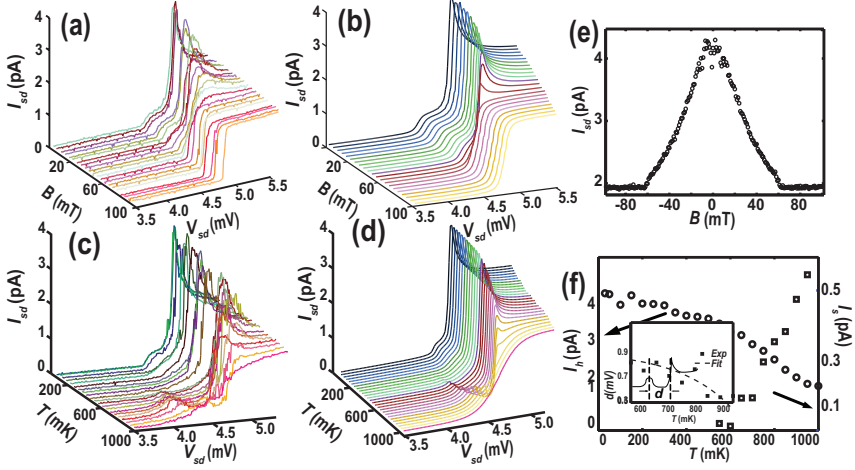
Figure 4.6: Probing the DOS of superconducting Al leads via an InSb nanowire quantum dot. (a) Source-drain current measured for Dev. *AlInSbAl#1*, as a function of V_{sd}, at $T = 40$ mK, $V_{bg} = -6.43$ V [the dashed line B in the inset of Fig. 4.5 (b)] and at different B. The current spikes at the edge of the Coulomb staircase gradually flatten as the applied field quenches the superconductivity of the Al contacts. (b) A simulation result of (a). (c) Source-drain current as a function of V_{sd}, at $B = 0$ mT, $V_{bg} = -6.43$ V and at different temperatures T. Rising temperature also flattens the DOS singularity features. (d) A simulation result of (c). (e) The current peak height as a function of magnetic field, extracted from panel (a). (f) The high peak height (circle) and the small peak height (square) caused by thermal excitation as functions of T. The subplot is the distance between the two peaks (defined by the inset schematic) as a function of T.

directly. According to the theoretical fit below, the energy resolution σ, i.e. the FWHM of the resonant level, is less than 5 μeV at the base temperature. Compared with the traditional scanning tunneling microscopy (STM) method [$\sigma \approx 15$ μeV (55)] and the photoemission spectroscopy method [$\sigma \approx 2.9$ meV (56)], this is really an ideal tool to investigate BCS-DOS of superconductor, especially for low dimensional materials.

Fig. 4.6 shows the magnetic field and temperature dependence measurements of the current spikes. In the magnetic field dependence measurements Fig. 4.6 (a), the temperature is fixed at 40 mK and V_{bg} is set at -6.43 V. As predicted by the relation in Eq. 4.1, the current peak is flattened gradually resulting from the field-induced gap suppression. The peak height as a function of magnetic field

is summarized in Fig. 4.6 (e). The current height has its maximum around the zero-B region and then fades as B increases. Finally, a transition point comes out at $B = 62$ mT, which indicates the disappearance of the superconductivity at the critical magnetic field $B_c = 62$ mT. We simulate the $I - V$ curves according to the model described later, and the simulation results are shown in Fig. 4.6 (b). Compairing Figs. 4.6 (a) and (b), it can be seen that the simulation fits very well with the measurement data.

The temperature evolution of the current peak shows the same tendency as the magnetic field dependency measurements. As shown in Fig. 4.6 (c), the peak is smeared as the superconductivity of the contacts are thermally washed out, which is consistent with Eq. 4.1. The temperature dependence of the peak height [Fig .4.6 (f), open circles] shows that the critical temperature T_c is about 1 K. Moreover, as the temperature rises, an additional current peak appears on the lower bias side of the main current peak. This is caused by the thermal excitation of quasi-particles over the superconductivity energy gap. On the one hand, Δ shrinks as the temperature goes up, and on the other hand the thermal energy of quasi-particles gets larger and larger. Therefore, more and more quasi-particles are excited over Δ, and therefore it will give another current peak when the resonant level in the quantum dot is aligned with these thermally excited quasi-particles. Simulation results for Fig. 4.6 (c) are shown in Fig. 4.6 (d). Fig. 4.6 (f) gives the height of the thermal current peak (open square) as a function of temperature. Contrary to the edge peak, the thermal peak height increases as the temperature increases. The distance d between the main current spikes and the thermal current peak [defined by the schematic in the subplot of Fig. 4.6 (f)], should be proportional to $4\Delta(T)/e$. Note that d is not determined by $2\Delta(T)/e$ as the bias voltage is applied symmetrically to the source/drain contacts. We can see that d decreases as the temperature increases, which is consistent with Eq. 4.1. The dashed line is the result of fit of d from Fig. 4.6 (d).

Figures 4.7 (a), (c), (e), (g), and (i) show the low-bias transport measurement near a resonant level. The main features here are consistent with Fig. 4.6: the NDC near the edge of the Coulomb steps, the DOS singularity induced sharp dI_{sd}/dV_{sd} peaks and the manifestation of $\Delta - B$ and $\Delta - T$ relations. However, a novel feature conflicting with our model arises. In our model, at small bias voltage $|V_{sd}| < 2\Delta/e$, there should be no net current through the dot in the presence of the quasi-particle DOS gap. In Fig. 4.7 (c), it is evident that high
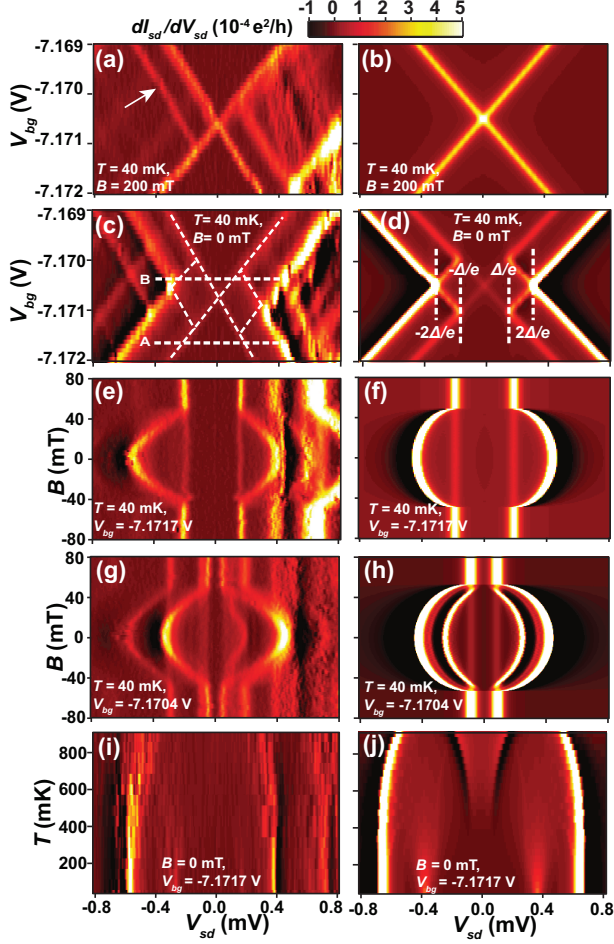
Figure 4.7: (a) A fine structure of the charge stability diagram around a resonant level. Al contacts are in the normal states at $B = 200$ mT. The high conductance line indicated by the arrow is attributed to the excited state, which is not included in the single level model. (b) A simulation result for panel (a). (c) The same as (a) but at $B = 0$ mT, and thereby the Al contacts are superconducting. (d) A simulation result for panel (c). (e) Differential conductance on a color scale as a function of B and V_{sd}, and V_{bg} is fixed at the position marked by the white dashed line A in panel (c). (f) A simulation result for panel (e). (g) and (h): The same as (e) and (f) respectively, but corresponding to the position marked by the white dashed line B in panel (c). (i) Differential conductance on a color scale, as a function of T and V_{sd}, and V_{bg} is settled at the position A. (j) A simulation result for panel (j).

dI_{sd}/dV_{sd} lines show up in the region $|V_{sd}| < 2\Delta/e$. These lines also extend out of the region $|V_{sd}| < 2\Delta/e$ and are parallel to the DOS singularity sharp peaks. In fact, these unexpected conductance lines also have homologous features at the large bias regime. By rechecking the current plots in Fig. 4.6 (b), we can find that a small current plateau lies on the lower bias side of each current spike. Additionally, the magnetic field measurements show that these weak dI_{sd}/dV_{sd} peaks do not change their positions as B changes.

These novel features can be interpreted by a non-zero DOS in the superconducting gap. Therefore, we can build the following model to simulate this system

Similar to the model in Ref. (57), the current tunneling from one side to another side, for example, from left to right, is given by

$$I_{l\rightarrow r} \propto \int\limits_{-\infty}^{+\infty} \mathcal{N}_S^l f\left(E, \mu_l\right) G\left(E\right) \mathcal{N}_S^r \left[1 - f\left(E, \mu_r\right)\right] dE \qquad (4.3)$$

where μ_l, μ_r are chemical potentials of left and right leads respectively, $f\left(E, \mu\right) = \left[1 + e^{(E-\mu)/k_B T}\right]^{-1}$ is the Fermi-Dirac distribution function. Therefore the net current is $I = I_{l\rightarrow r} - I_{r\rightarrow l}$. As we mentioned above, the BCS-DOS is given by Eq. 4.2. To be more precise, we update it by adding a constant item C (56) to represent the non-zero DOS in the gap, and replacing E with $E - i\gamma$, i.e., the Dynes model for non-ideal superconductor with grain, impurity or defects (58). We then get

$$\mathcal{N}_s\left(E, B, T\right) = \mathcal{N}_n\left(E\right) \frac{E - i\gamma}{\left[(E - i\gamma)^2 - \Delta(B, T)^2\right]^{1/2}} + C \qquad (4.4)$$

We use Lorentzian function to describe the broadened line-shape of the resonant level (59):

$$G_\epsilon\left(E\right) = \frac{\Gamma/2\pi}{(E-\epsilon)^2 + (\Gamma/2)^2} \qquad (4.5)$$

where ϵ is the energy of the quantum level related to the Fermi level and $\Gamma = \Gamma_L + \Gamma_R$ is the total coupling strength.

In the simulation, we take $\gamma = 1\mu eV$ and $\Gamma = 10\mu eV$ and let $C = 0.2\mathcal{N}_n$. The normalized simulation results are shown in Figs. 4.6 (b) and (d), and Figs. 4.7 (b), (d), (f), (h), and (j).

The model with a residual normal DOS item C in the superconducting gap fits well with measurement results. However, there is not a final conclusion about

where these normal states come from. The Dynes model itself can induce a non-zero DOS within Δ as long as γ is large enough. However, in our model, the Dynes model cannot give a good fit without the item C. A possibility is that these normal states may rise from the InSb nanowire segments beneath the contacts. This proposal is consistent with the features of the quasi-1D leads states in Dev. *NbInSbNb#1* that we discussed in Chapt. 3. However, a systemic study for the model of superconductor electrode/barrier/semiconductor lead-quantum dot-semiconductor lead/barrier/superconductor electrode is required with all possible configuration.

4.3 Josephson effect and proximity effect

4.3.1 Introduction of the Josephson effect and the proximity effect

In 1962, Josephson made the remarkable prediction that a dissipationless super-current should flow between two superconducting electrodes even when separated by a thin normal state layer (60). This effect is the so-called *Josephson effect*. The superconductor-normal conductor (or insulator, semiconductor)-superconductor (SNS) junction is therefore referred to as a *Josephson junction*, and the supercurrent through the Josephson junction is called the *Josephson current*. The critical current for a Josephson junction is given by:

$$I_c = I_m \sin \Delta\varphi \tag{4.6}$$

in which $\Delta\varphi = \Delta\varphi_L - \Delta\varphi_R$ is the phase difference between the superconducting wave function of the left and the right-side superconductors, and I_m is the maximum critical current that the junction can hold. I_m is usually much smaller than the intrinsic critical current of the superconductor.

Actually before Josephson effect was proposed, a supercurrent flowing through an SNS junction was found and was explained by the *proximity effect* (61, 62). As we pointed out earlier, all the electrons near the Fermi level of the superconductor condense into the BCS ground state and form bosonic Cooper pairs. All the Cooper pairs can be described by a macroscopic wave function ψ and have the same phase φ. At the interface of the superconductor and normal conductor, the amplitude of ψ cannot go to zero abruptly. Instead, ψ leaks out of the superconductor and spreads into the normal conductor. The decay tail length of ψ is determined by the superconductor coherence length ξ. In an SNS junction, the
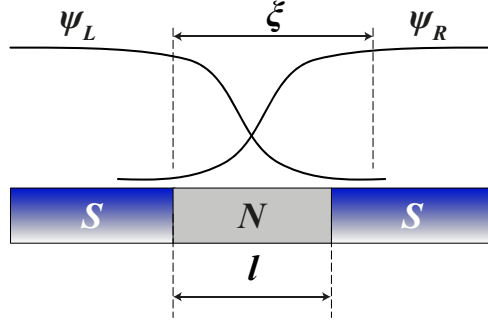
Figure 4.8: The superconducting proximity effect at the superconductor-normal conductor interface. In an SNS junction, a supercurrent can flow through the whole junction if the SN coupling is strong and the separation l between superconductors is smaller than or comparable to the superconductor coherence length ξ.

wave functions of the left-side and right-side superconductors, ψ_L and ψ_R, overlap if the width of the normal conductor l is smaller than or comparable to ξ[Fig. 4.8]. In microscopic view, the proximity effect is due to the penetration of Cooper pairs from superconductor to normal conductor in the vicinity of the interface. The incident Cooper pair remains their correlation in the normal conductor within a lifetime. Note the Cooper pair penetration is also interpreted as a process called the Andreev reflection which will be addressed later.

Besides the disspationless supercurrent, another important consequence of the proximity effect is the opening up of a quasi-particle DOS gap in the normal conductor, i.e., the induced superconducting energy gap. In Chapt. 5, we will show the direct probing of the induced superconducting energy gap and see how critical the induced superconducting energy gap is for searching for Majorana fermions.

4.3.2 Josephson current in InSb nanowire based Josephson Junction

In addition to the normal conductor, the normal state layer in the Josephson junction can also be semiconductor or insulator. Semiconductor nanowire or carbon nanotube based Josephson junctions have already been reported in Refs. (63, 64, 65). Especially, the InSb nanowire based Josephson junctions have also been achieved recently (51, 66).

Here, we show the transport measurement results for a Nb coupled InSb
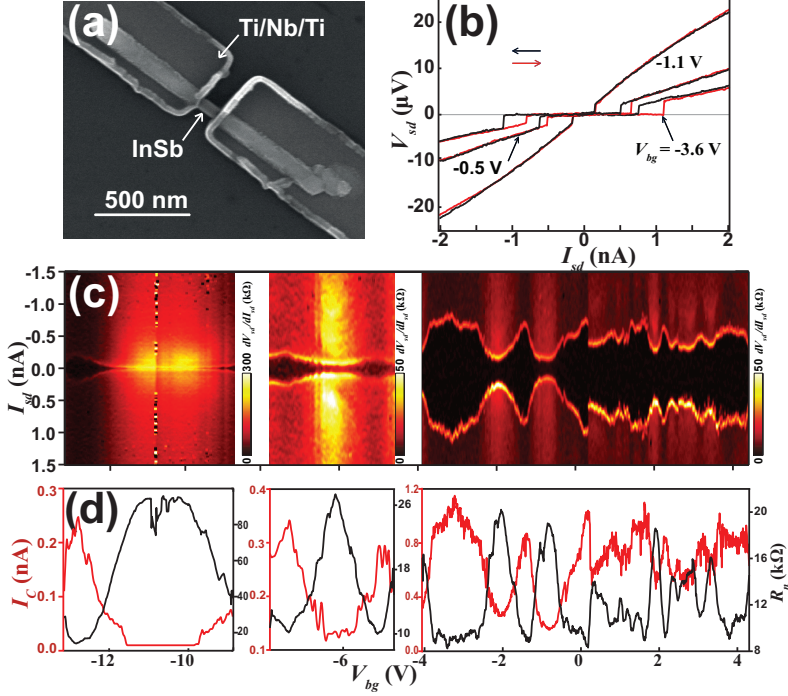
Figure 4.9: Josephson current through Dev. *NbInSbNb#2*. (a) SEM image of the device. The electrodes in the device are made from trilayer superconductor Ti/Nb/Ti (3/80/5 nm). The diameter of the InSb nanowire is about 65 nm, the separation between contacts is about 110 nm, and the lengths of the InSb nanowire sections covered by the two Nb based contacts are about 740 and 680 nm, respectively. (b) The source-drain voltage drop V_{sd} at the junction, as a function of the applied source-drain current I_{sd}, at three different back-gate voltages $V_{bg} = -3.6$ V, -1.1 V and -0.5 V. The red and black curves are recorded in the upward and the downward current sweeping direction, respectively. (c) Differential resistance on a color scale as a function of I_{sd} and V_{bg} measured for the device at $B = 0$ T. Here, the critical supercurrent shows a clear V_{bg} dependence. (d) The critical current I_c (red curve) and the normal state resistance R_N (black curve) as a function of V_{bg} measured for the device at $B = 0$ T. It is generally seen that the smaller R_N is, the larger I_c is.

nanowire device, or Dev. *NbInSbNb#2*. An SEM image of this device is shown in Fig. 4.9 (a). First, we characterize this device by current biased measurements. Figure 4.9 (b) shows the measured source-drain voltage of the device at a temperature of 25 mK as a function of the applied source-drain current I_{sd} at three different voltages V_{bg} applied to the back-gate. A zero resistance branch is clearly seen in each measured curve, which indicates the presence of a dissipationless Josephson supercurrent in the junction. The Josephson junction switches to a dissipative transport branch when the applied current is larger than the critical current I_c. Similar to the $I - V$ curve of the TiNbAl trilayer superconductor discussed in last section, the device also shows a hysteretic behavior, i.e., the upward current sweeping trace (red curve) and downward sweeping trace (black curve) have different switching points.

The critical current I_c of a semiconductor based Josephson junction is related to the resistance of the junction in the normal state (63, 66) and can thereby be tuned by V_{bg}. For example, in Fig. 4.9 (b), we see that I_c is 1.1 nA at V_{bg} = -3.6 V but it is only 0.2 nA at $V_{bg} = -1.1$ V. The tunability of the critical supercurrent I_c can be visualized more clearly in Fig. 4.9 (c), where the differential resistance is plotted as a function of I_{sd} and V_{bg}. I_c is characterized by the width of the low differential conductance region and it is evident that I_c is a function of V_{bg}. Fig. 4.9 (d) shows the measured critical current I_c and the normal state resistance R_n as a function of V_{bg}. The resistance R_n is deduced from the differential resistance at I_{sd} = 1.5 nA in Fig. 4.9 (c). At 1.5 nA and beyond the $V_{sd} - I_{sd}$ characteristics show approximately straight lines [see Fig. 4.9 (b)]. Generally, a small I_c is observed at a region of gate voltage for which R_n is large. According to theoretical predictions (45), the product $I_c R_n$ is a constant that is proportional to the superconducting energy gap: $I_c R_n = \pi \Delta / e$. However, the measured $I_c R_n$ product in this device is not a constant, but varies from 2 μV to 12 μV. These values are overall much smaller than the expected value of $\pi \Delta_{Nb} / e \approx 4.7$ mV. Such reduced experimental values have also been observed in Refs. (63, 66) and can typically be attributed to a premature switching due to thermal activation in a capacitively and resistively shunted junction and to finite transparencies at the superconductor-nanowire interfaces (45).

Figure 4.10 (a) shows the measured differential resistance of Dev. *NbInSbNb#2* as a function of I_{sd} and the magnetic field B applied perpendicular to the substrate at $V_{bg} = -3.6$ V. It is generally seen that the critical current I_c decreases
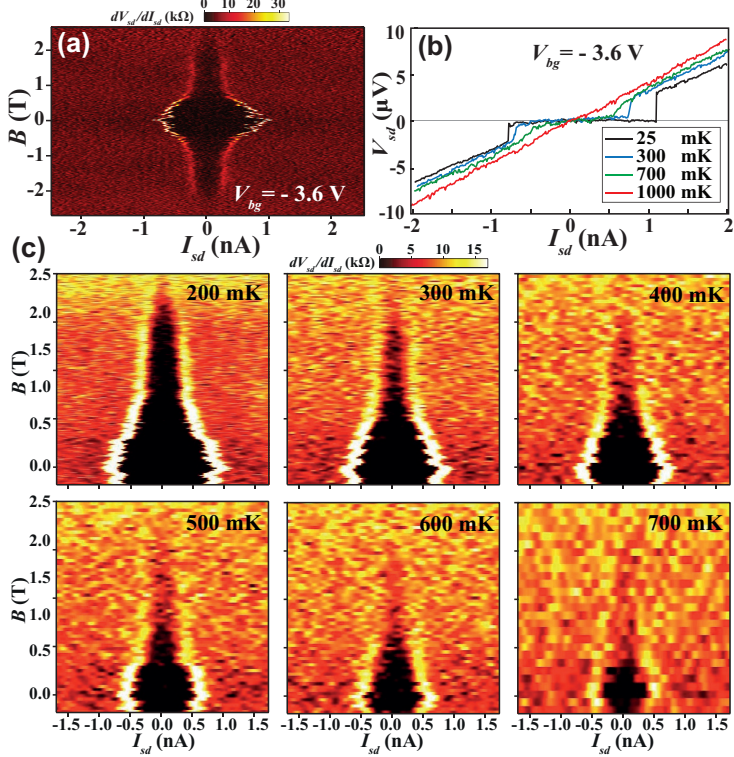
Figure 4.10: Magnetic field and temperature dependence measurements of the Josephson current in Dev. *NbInSbNb#2*. (a) Differential resistance on a color scale measured for Dev. *NbInSbNb#2* at $V_{bg} = -3.6$ V, as a function of I_{sd} and the magnetic field B applied perpendicularly to the substrate. The Josephson current is seen to persist as the magnetic field goes up to $B \sim 2$ T. (b) Source-drain voltage V_{sd} measured for the device, as a function of I_{sd} at $V_{bg} = -3.6$ V and $B = 0$ T and at four different temperatures $T = 25$, 300, 700, and 1000 mK. We can see that the supercurrent continues to be visible when the temperature goes up to $T = 700$ mK, but it disappears at $T = 1$ K. (c) The same as (a), but at different temperatures, from $T = 200$ mK to $T = 700$ mK. It is evident that B_c decrease as the temperature increases.

as B increases and disappears after the magnetic field becomes higher than the critical value B_c. We find that, with Nb contacts, B_c can reach a few Tesla, which is much higher than for Al based junctions (63, 66). The high B_c of the Josephson junction is due to the high intrinsic B_c of the Nb-based trilayer superconductor. Figure 4.10 (b) displays the source-drain voltage V_{sd} as a function of I_{sd}, measured at different temperatures for the device at $V_{bg} = -3.6$ V and $B = 0$ T. The measurements show that I_c has a clear temperature dependence. As the temperature increases, I_c decreases gradually. Eventually, I_c disappears at the temperatures higher than a critical value of $T_c \sim 1$ K. In Fig. 4.10 (c), a series of differential resistance measurements are shown, which are the same as in Fig. 4.10 (a) but at different temperatures, from $T = 200$ mK to $T = 700$ mK. It is evident that B_c decreases as the temperature increases. Above all, the magnetic field and temperature dependence of the Josephson current show the same tendency as the intrinsic supercurrent in superconductor metals.

As we will see later, InSb nanowire based Josephson junctions have promising applications in superconducting quantum computers (6, 67). Especially, the proximity effect induced superconductivity in InSb nanowire is very critical for the research of Majorana bound states in solid state systems. This is a crucial component for topological quantum computing (9).

4.3.3 Josephson current in an InSb/InAs nanowire based SQUID device

As indicated by Eq. 4.6, the amplitude of the Josephson current is strongly influenced by the phase difference between two superconductor electrodes. The Josephson current will show a sinusoidal modulation by $\Delta\psi$. If two Josephson junctions are connected by a superconductor loop, they then form a so-called *superconducting quantum interference device* (SQUID) (68). A SQUID system is composed of two Josephson junctions in parallel connected via a superconducting loop, as shown in the schematic in Fig. 4.11 (a). In the presence of a magnetic field, a magnetic flux $\Phi = B \cdot S$ is enclosed in the loop. If the maximum Josephson currents of the junctions are the same $I_{m1} = I_{m2} = I_m$, the Josephson current of the SQUID is then given by:

$$I_c = 2I_m \cos\left(\pi\Phi/\Phi_0\right) \qquad (4.7)$$

where Φ_0 is the flux quanta. The superconducting interference is a Cooper pair version of the Aharonov-Bohm effect (69), in which interference of single electrons is modulated with a vector potential A caused by an enclosed magnetic flux in a loop. Because the Cooper pair carries two elementary charges, the flux quanta in the SQUID is $\Phi_0 = h/2e$ instead of h/e in normal electron interference systems. For more general cases in which the $I_{m1} \neq I_{m2}$, Eq. 4.7 is modulated to (70, 71, 72):

$$I_c = \sqrt{(I_{m1} - I_{m2})^2 + 4I_{c1}I_{c2}\cos^2(\pi\Phi/\Phi_0)} \qquad (4.8)$$

.

Figure 4.11 (b) displays the schematic of a measured SQUID device made from a Ti/Nb/Al-trilayer coupled InSb junction and InAs junction. In the standard current-biased setup, the differential resistance on a color scale is illustrated in Fig. 4.11 (c), as a function of I_{sd} and a perpendicularly applied magnetic field B, at $V_{bg} = 3.9$ V and $T = 25$ mK. The critical current I_c can be extracted from the width of the zero-resistance region (dark) in the color scale. It is evident that the I_c shows a cosine-like oscillation in the range of $B = 0 - 100$ mT, which is the manifestation of Cooper pair interference. The oscillation period is about 20 mT. According to Eq. 4.7, this gives an effective SQUID area of $S \approx 1\mu m^2$. This effective area is much larger than the area of the red dashed square in Fig. 4.11 (b), which is about $0.4\mu m^2$. This is probably because the InSb nanowire and InAs nanowire have large contact areas with the superconductor, and the real SQUID area is extended, as the black dashed square shown in Fig. 4.11 (b).

However, in the high field region as shown in Fig. 4.11 (d), the oscillation of I_c disappears. We do not know the reason for the missing of I_c oscillation, but one possible argument is that the Cooper pair tunneling through one of the junctions is turned off by the magnetic field-effect-transistor behavior (B-FET, for a detailed discussion about this effect see Chapt. 5). The SQUID is degraded to a single Josephson junction.

Moreover, Fig. 4.12 shows that the magnetic field can also change the oscillation periods of I_c. Fig. 4.12 (a) displays similar measurements as in Fig. 4.11 (c), but at a different back-gate voltage $V_{bg} = 5$ V. The critical current I_c as a function of magnet field is extracted in Fig. 4.12 (b), and it is fitted to a cosine function (the dashed line). Here, the oscillation period is also about 20 mT. However, in the high field region as shown in Fig. 4.12 (c) and (d), the oscillation
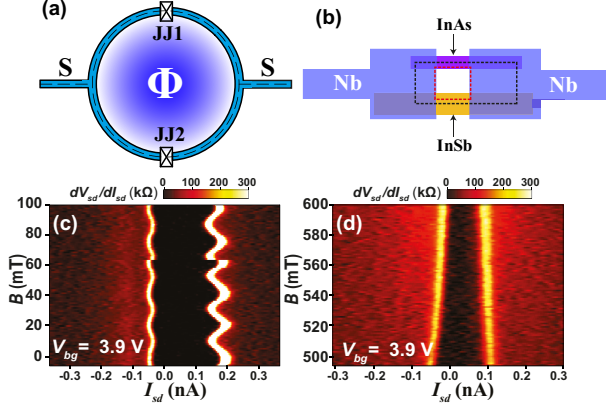
Figure 4.11: A SQUID device made from InSb and InAs nanowire Josephson junctions. (a) Schematic of a typical SQUID. (b) Schematic layout of a SQUID made from Nb-coupled InSb and InAs nanowires. (c) Differential resistance on a color scale measured for the SQUID, as a function of the applied source-drain current I_{sd} and magnetic field B, at $V_{bg} = 3.9$ V and $T = 25$ mK. The critical current I_c is represented by the width of the zero-resistance region. (d) Similar to (c), but in a different field region.

period is enlarged to about 32 mT. Again, the reason for the oscillation period change is not clear to us. From the point of view of the B-FET argument, the high magnetic field may dramatically change the potential profile of the junctions and therefore lead to a change of the effective SQUID area.

4.4 Conductance sub-gap structures in Josephson quantum dots

When the coupling between superconductors and normal conductors in an SNS structure is not strong enough, Cooper pairs cannot go directly through the junction via the proximity effect. There are voltage drops at the SN/NS interfaces and the N part itself when a non-zero current is passing through, and therefore a potential difference $\Delta\mu = \mu_s - \mu_d$ is developed between the two superconductors[1]. In fact, even in an SNS system with strong coupling, $\Delta\mu$ can also be developed

---

[1]This is the reason why we can probe the DOS of superconductors in the S-InSb QD-S system. The opaque barriers between S and QD protect the superconductivity from being destroyed by the large current.

Figure 4.12: Critical current of the SQUID. (a) Differential resistance on a color scale measured for the SQUID, as a function of the applied source-drain current I_{sd} and magnetic field, at $V_{bg} = 5$ V and $T = 25$ mK. (b) Extracted critical current as a function of magnet field. The dashed line is a cosine fit for the experimental data. (c) and (d) are similar to (a) and (b), respectively, but in a different magnetic field region.

when the applied source-drain current exceeds the critical current of the junction. Because the intrinsic critical current of a superconductor is usually much larger than the critical current of the Josephson junction, the induced superconductivity in the N layer will disappear first as the applied current increases. Then the voltage drops across the N layer as in the decoupled SNS structure. Many novel features will arise from the voltage-biased SNS systems. Especially, in the S-QD-S system (the Josephson QD), conductance sub-gap structures (SGS) such as multiple Andreev reflection (MAR), Andreev bound states (ABS) and Yu-Shiba-Rusinov states (YSR).

4.4.1 Mechanisms of SGS in Josephson junctions

As an incident electron at the Fermi level comes to the interface of the normal conductor and the superconductor, it will be scattered at the interface in the presence of the superconducting energy gap Δ. The scattering here takes a very unique form, which forces the electron to grab another nearby electron to form a Cooper pair and to enter the superconductor. As a result, a hole with an opposite
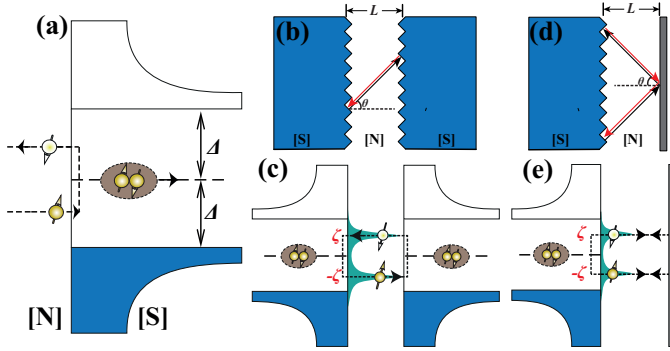
Figure 4.13: Schematic of Andreev reflection and Andreev bound states in the SNS and SN systems. (a) Andreev reflection occurs at the interface of a normal conductor and a superconductor. An incident electron (hole) from the normal layer side hits the SN interface, and another hole (electron) with an opposite spin will be reflected back. (b-c) The coherent back-and-forth Andreev reflections form bound states in the sandwiched normal layer. The configuration is an analogue of the Fabry-Pérot resonator and only the resonant states with standing-wave-like Schrödinger functions can be established. (d-e) Andreev bound states can also be established in a half Josephson junction (SN) structure.

spin and an opposite wave vector will be reflected back. The process is called the *Andreev reflection* and it is schematically shown in Fig. 4.13. If the incident charge carrier is a instead hole, the reverse process occurs, and an electron with an opposite spin and an opposite wave vector gets reflected back.

In an SNS junction in equilibrium, once the Andreev reflection is initialized, a process of bouncing back-and-forth will occur in between the two superconductors [Figs. 4.13 (b-c)]. This configuration is an analogue of the Fabry-Pérot optical resonator (73). Only the coherent states with standing-wave-like Schrödinger functions are robust. The quantization condition of the bound states is that the phase shift φ acquired on a single round-trip (two reflections) should be an integer multiple of 2π (74):

$$\varphi \equiv 2\frac{\zeta L'}{\hbar v_F} - 2\arccos\frac{\zeta}{\Delta_0} \pm \delta\phi = 2\pi m \quad m = 0, \pm 1, \pm 2, ... \tag{4.9}$$

where ζ is the energy of the bound state relative to the Fermi level, v_F is the Fermi velocity, $\delta\phi = \phi_L - \phi_R$ is the phase difference between the two superconductors, and $L' = L/\cos\theta$ is the traveling length of the electron/hole from one side of the superconductor to the other side. The item $\frac{\zeta L'}{\hbar v_F}$ is the phase shift picked up

by the electron/hole on a single path, while $\arccos\frac{\zeta}{\Delta_0}$ is the phase shift gained in a single reflection event. Because of the electron-hole symmetry, those bound states always come in pairs. Each pair contains an electron-like bound state and a hole-like bound state, and they are symmetric with respect to the Fermi level. According to Eq. 4.9, the discrete ABS spectrum can be tuned by varying the phase difference between superconductors, as reported in Refs. (75, 76).

ABS plays an important role in transferring the supercurrent through the SNS junction. However, it does not only exist in SNS junctions. Figure 4.13 (d) shows that the bound states can also be established in a superconductor-normal layer-barrier structure (a half Josephson junction). In this process, after an electron (hole) is reflected by the superconductor, it hits the barrier at the other side. The normal barrier bounces the incident electron (hole) back without changing its spin or charge sign. The electron (hole) then hits the SN interface again and a hole (electron) with an opposite spin is reflected. In this case, a whole round trip contains two Andreev reflections and two normal reflections. Since an elastic normal reflection does not change the phase, the total phase shift is $\varphi \equiv 4\frac{\zeta L'}{\hbar v_F} - 2\arccos\frac{\zeta}{\Delta_0}$. Therefore, the quantization condition of the bound states in the SN structures is given by:

$$\varphi \equiv 4\frac{\zeta L'}{\hbar v_F} - 2\arccos\frac{\zeta}{\Delta_0} = 2\pi m \quad m = 0, \pm 1, \pm 2, ... \tag{4.10}$$

These entangled ABSs in the SN-hybrid structures lead to discrete peaks in the DOS of the quasi-particles. These DOS peaks can be probed by tunneling spectroscopies (77, 78, 79, 80, 81).

When a bias voltage is applied to the two superconductors in the SNS junction, Andreev reflections cannot be bound any more. However, multiple Andreev reflection (MAR) events can still generate SGS features at $V_{sd} = 2\Delta/ne(n = 1, 2, ...)$. Differential conductance peaks emerge at each onset of the coherent MAR events (82) at low temperature. Figure 4.14 (a) shows an SNS junction with a bias voltage $V_{sd} = 2\Delta/e$ applied to the two superconductors. The bias aligns the lower electron-like quasi-particle DOS singularity of the left-side superconductor with the upper hole-like quasi-particle DOS singularity of the right-side superconductor.Quasi-particles direct tunneling peaks at $V_{sd} = 2\Delta/e$, and a differential conductance peak develops. Although no Andreev reflection occurs, we refer to the process as the first-order MAR. At $V_{sd} = \Delta/e$ [Fig. 4.14 (b)], the Fermi level of the left-side superconductor is aligned with the lower edge of the
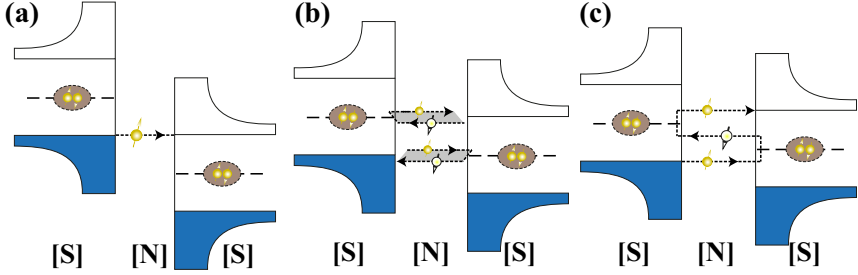
Figure 4.14: Schematic of multiple Andreev reflections. (a) The first-order MAR occurs under a bias voltage of $2\Delta/e$. The alignment of the left-lower and the right-upper quasi-particle singularities will lead to a differential conductance peak. Note that it is called the first-order of MAR induced conductance peak but there is no reflection at all. (b) The second-order MAR, where $\mu_s - \mu_d = \Delta$. The Andreev reflections occur at the SN interfaces. (c) The third-order MAR, where, $\mu_s - \mu_d = 2/3\Delta$.

upper band of the right-side superconductor. At the same time, the Fermi level of the right-side superconductor is aligned with the upper edge of the lower band of the left-side superconductor. Here the reflection of the hole-like quasi-particles from the right-side superconductor and the reflection of the electron-like quasi-particles from the left-side superconductor occurs. This process is referred to as the second-order MAR. In Fig. 4.14 (c), at a bias of $2/3\Delta/e$, a process involving two Andreev reflections is possible. Here, an electron-like quasi-particle from the singularity of the lower band of the left-side superconductor is Andreev-reflected against the right-side superconductor, reflecting a hole-like quasi-particle. The hole-like quasi-particle is in turn Andreev-reflected against the left-side super-conductor, sending an electron-like quasi-particle back. Finally, the electron-like quasi-particle enters the upper band of the right-side superconductor. The entire process is called the third-order MAR. Further lowering of the bias could induce more high-order MARs. However, as the order of the multiple Andreev reflection increases, the total scattering path gets longer and the process gets more difficult to keep coherent.

4.4.2 SGS in Josephson QD without Kondo effect

The SGS of the Josephson junction can be very complicated in the presence of the on-site Coulombic repulsion in the sandwiched object of nanoscale. In
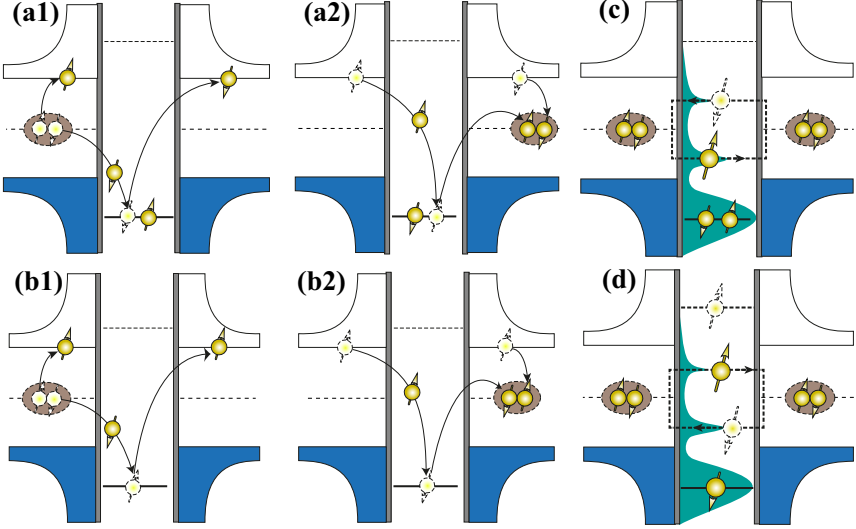
Figure 4.15: Schematic process of the co-tunneling of the Cooper pair across a quantum dot. (a1-a2) The "0"-junction: The Cooper pair tunnels through the quantum dot with a spin-singlet ground state, via a fourth-order co-tunneling process. No extra phase shift is picked up in this sequence of processes. (b1-b2) The "π"-junction: The Cooper pair tunnels through the quantum dot with a spinful doublet ground state, via a fourth-order co-tunneling process. The process is accompanied by the spin-flips on the dot and results in a π-phase shift to the transferred Cooper pair singlet. (c) and (d) show the Andreev bound states in a Josephson quantum dot with the spin-singlet and spin-doublet ground states, respectively. Compared with the "0"-junction, the electron-like bound state and the hole-like bound state swap their positions in energy in the "π"-junction.

this subsection, we focus on the SGS of the Josephson quantum dot without the influence of the Kondo effect. Before analyzing any experimental data, we discuss how the spin on the dot modifies the SGS.

When the sandwiched normal object in an SNS structure is a quantum dot, the Andreev transport process becomes sensitive to the dot configuration. In the strong coupling regime, where $\Gamma \gg E_C, \Delta$ (Γ is the total dot-leads coupling and E_C is the charging energy of the dot), the Coulomb blockade is negligible and the Andreev transport process is similar to the SNS junction discussed above. However, the Coulombic energy has to be taken into account when E_C is much larger than Γ. In this case, the intermediate quasi-particle-reflections in the

Andreev transport process cannot take ballistic paths as shown in Figs. 4.13 (b-d), but have to take a high-order co-tunneling path via virtual state(s) (83). When the ground state of the sandwiched quantum dot is a spin-singlet of zero spin (even occupation), the Cooper pair tunneling process does not pick up any additional phase shift more than the phase shift given in Eq. 4.9. Whereas, if the dot ground state is a spin-doublet with a $-\frac{1}{2}$ net spin (odd occupation), the dot behaves like a magnetic impurity and induces an additional phase change to the Cooper pair co-tunneling.

The details of the co-tunneling of the Cooper pair through a quantum dot are shown schematically in Fig. 4.15. Prohibited by the Coulomb blockade, the Cooper pair can only transport via the fourth-order co-tunneling process. Figures 4.15 (a1-2) illustrate the transfer of a Cooper pair through a quantum dot with a spin-singlet ground state. The co-tunneling starts from the transfer of one half of a Cooper pair in the left-side superconductor, for example, the down-spin electron as shown in Fig. 4.15 (a1). Via a virtual state, the down-spin electron tunnels into the dot by kicking out the down-spin electron of the spin-singlet on the dot. The system then comes to another virtual state (the energy is not conserved at this point), but the dot is still in the spin-singlet state. The co-tunneling of the up-spin electron of the original Cooper pair then occurs via another virtual state. The up-spin electron of the singlet in the dot is kicked out by the tunneling-in electron and it combines with the previously tunneled down-spin electron to form a new Cooper pair. In the whole process, three virtual states are involved and therefore the process is a fourth-order co-tunneling event.

The Cooper pair co-tunneling process via a spinful doublet ground state can be very different from the process via a spin-singlet, as shown in Figs. 4.15 (b1-2). The co-tunneling is also carried out by two half-Cooper pair co-tunneling events. However, each event is accomplished with a spin-flip in the dot, i.e., the tunneling-in down-spin (up-spin) electron kicks out an up-spin (down-spin) electron that was occupying the spin-doublet ground state of the dot. The spin-flip is favored because its corresponding virtual state has a lower energy than other possible virtual states. As a result, the Cooper pair singlet state from the left-side superconductor, $|\psi_L\rangle = (|\uparrow\downarrow\rangle - |\downarrow\uparrow\rangle)$, becomes $|\psi_R\rangle = (|\downarrow\uparrow\rangle - |\uparrow\downarrow\rangle) = e^{i\pi} |\psi_L\rangle$ in the right-side superconductor after being transferred across the dot. The sequence of the co-tunneling process above picks up a π-phase shift to the Cooper pair singlet state. Therefore, the Josephson quantum dot with a doublet ground state

is referred to as a *"π"-junction*, while the Josephson quantum dot with a singlet ground state is a *"0"-junction*. The Josephson current through a "π"-junction reverses in sign compared with the Josephson current through a "0"-junction.

Back to the point of view of ABS, compared with the "0"-junction, the electron-like ABS and the hole-like ABS in the "π"-junction swap their positions in the energy spectrum [Figs. 4.15 (c) and (d)]. The Josephson quantum dot can be tuned from a "0"-junction to a "π"-junction (from the even occupation to the odd occupation in weak coupling regime) by a gate. Therefore, the electron-like ABS overlaps with the hole-like ABS at the Fermi level at the phase-transition point. This phase-transition is called the *quantum phase transition* (QPT).

Now we focus on the SGS measurements that were performed for an Al-coupled InSb nanowire quantum dot device, named as Dev. *AlInSbAl#3*. Figure 4.16 (a) displays an SEM image of Dev. *AlInSbAl#3* and Fig. 4.16 (b) shows the schematic layout of the device. In this device, the InSb nanowire with a diameter of ∼70 nm is contacted by two Ti/Al (5/90 nm) superconductor leads with a separation of 120 nm. Besides the global back-gate, a fork-shape side-gate and a stick side-gate are also fabricated in order to finely control the chemical potential of the dot and the dot-leads coupling strength/symmetry.

The charge stability diagram in Figs. 4.16 (c) and (d) show the Coulomb diamond structures corresponding to the first electron in the normal state and the superconducting state, respectively. The two side-gates are not used here. The charging energy E_C is estimated to be about 8.5 meV according to the diamond size. E_C is much larger than the superconducting energy gap of Al $\Delta = 157\mu$eV. No Kondo ridge can be seen in the diamond, indicating that the dot-leads coupling Γ is weak. Compared with the diamond in the normal state, some features arise in the low-bias region in Fig. 4.16 (d) as the superconductivity of the leads is turned on. The fine structure in Fig. 4.16 (e) shows that the conductance SGS emerges. There are two pairs of vertical high-conductance lines around $V_{sd} = \pm 2\Delta/e$ (indicated by the black arrows) and $V_{sd} = \pm\Delta/e$ (red arrows). Figure 4.16 (f) displays two $dI_{sd}/dV_{sd} - V_{sd}$ line-cuts taken at point A and point B in Fig. 4.16 (e). It is evident that there are two differential conductance peaks at $V_{sd} = \pm 2\Delta/e$ and a conductance plateau with a threshold at $V_{sd} = \pm\Delta/e$. These features can be attributed to the first-order and the second-order MARs. High-order MARs are not visible in this regime due to the weak coupling.

Figure 4.16 (g) shows a close-up view of the region near the resonant level [the
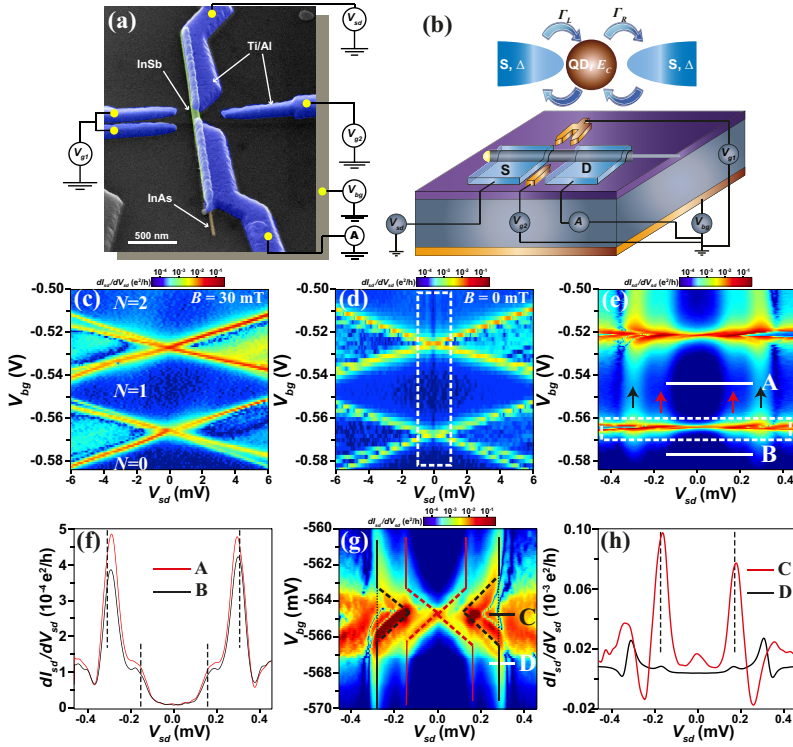
Figure 4.16: SGS of a Josephson quantum dot without the Kondo effect. (a) SEM image of Dev. *AlInSbAl#3*. The InSb nanowire is contacted by two Ti/Al (5/90 nm) superconductor leads with a separation of 120 nm. In addition to the global back-gate, a fork-shape side-gate and a stick side-gate are also fabricated. (b) Schematic layout of the device. (c) The charge stability diagram of Dev. *AlInSbAl#3*. The Coulomb diamond structure corresponding to the first electron occupation is shown here. The measurements are performed at $B = 30$ mT and the device is in its normal state. The charging energy can be estimated from the size of the diamond to be $E_C = 8.5$ meV. (d) The same as (c), but with $B = 0$ mT. The superconductivity of the leads is turned on. Some superconductivity-induced conductance features emerge in the low-bias region. (e) A close-up view of the squared region in (d). Vertical high-conductance lines are visible, which can be attributed to the MARs. (f) Two $dI_{sd}/dV_{sd} - V_{sd}$ line-cuts taken from (e). The conductance peaks around $V_{sd} = \pm 2\Delta/e$ and $V_{sd} = \pm \Delta/e$ are visible, corresponding to the first-order MAR and the second-order MAR, respectively. (g) A zoomed-in view of the squared region in (e). There are two high-conductance lines crossing at the resonant level, with another two outer parallel high-conductance lines. Those lines are due to the ABS formed in this junction and the crossing indicates that a QPT occurs when the quantum dot changes from even occupation to odd occupation. (h) The red line represents the $dI_{sd}/dV_{sd} - V_{sd}$ line-cut, taken at point C in (g), while the black line is taken at point D.
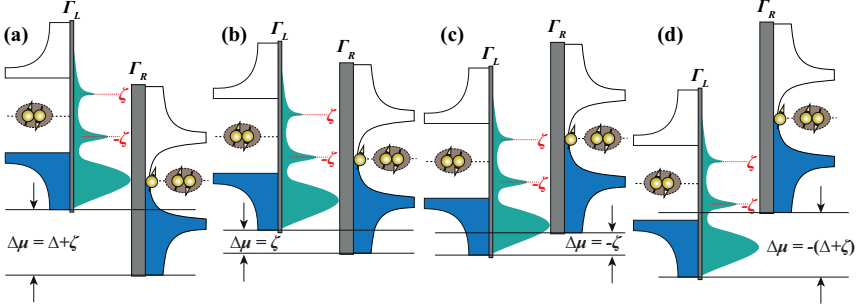
Figure 4.17: ABSs formed in the Josephson QD with asymmetric couplings. ABSs are formed at the interface of the left-side superconductor and the quantum dot, while the right-side superconductor serves as a tunneling tip and can probe the ABSs. (a) The configuration with a bias voltage $V_{sd} = (\Delta + \zeta)/e$. The lower ABS is aligned with the hole-like quasi-particle DOS singularity in the right-side superconductor and will result in a differential conductance peak. (b) The configuration with a bias voltage $V_{sd} = \zeta/e$. The lower ABS is aligned with the Fermi level of the right-side superconductor. The residual normal DOSs in the superconducting energy gap will lead to a weak differential conductance peak. (c) The bias-mirrored configuration of (b). (d) The bias mirrored configuration of (a).

squared region in Fig. 4.16 (e)]. We see that the vertical MARs high-conductance lines are interrupted at the resonant point. Two high-conductance lines (red-dashed lines) cross at the zero-bias voltage and are parallel to another outer pair of high-conductance lines (black-dashed lines). The $dI_{sd}/dV_{sd} - V_{sd}$ line-cut taken at the crossing point C is shown in Fig. 4.16 (h), in which we can see that the minimum separation of the outer conductance peaks is $2\Delta/e$. The high-conductance lines near the resonant point are the manifestations of ABSs formed in the Josephson quantum dot with a very asymmetric coupling.

Without loss of generality, let us assume $\Gamma_L \gg \Gamma_R$, namely, the dot is coupled strongly to the left-side superconductor but is well decoupled from the right-side superconductor. As a result, the S-QD-S junction degrades to an S-QD system with the other side of superconductor serving as a tunneling probe. ABSs are formed in the S-QD system at $\pm\zeta$ and are pinned to the left-side superconductor, as shown in Fig. 4.13 (e). The right-side superconductor can probe the DOS of the S-QD system. Differential conductance peaks will arise at $V_{sd} = \pm(\Delta + \zeta)/e$, when the lower (upper) ABS is aligned with the hole-like (electron-like)
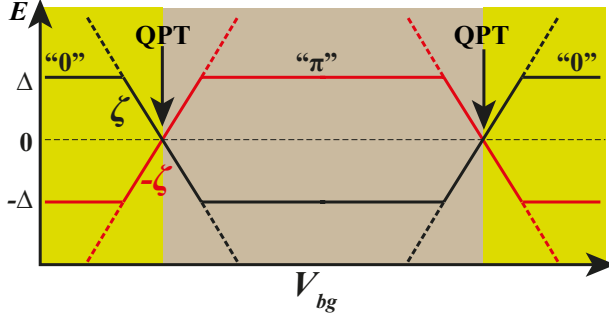
Figure 4.18: Schematic diagram of ABSs energies as a function of gate voltage. The texts
"0" and "π" indicate that the Josephson quantum dot is a "0"-junction or "π"-junction in
the corresponding regime. The two ABSs cross at the phase-transition points. As the gate
voltage goes away from the QPT point, ABSs merge with the quasi-particle continuum at
$\pm\Delta$.

quasi-particle DOS singularity in the right-side superconductor [Figs. 4.17 (a) and
(d)]. Moreover, in this case the superconducting energy gap is a softened gap,
i.e., there are normal DOS residuals in the superconducting energy gap. This
soft-gap may rise from material defects, impurities in the superconductor (58)
or the inhomogeneities of the superconductor-semiconductor interface (84, 85).
Therefore, when the Fermi level of the normal DOS is aligned with the ABSs at
$V_{sd} = \pm\zeta/e$, differential conductance peaks arise [Figs. 4.17 (b) and (c)] (86).

The ABSs energy dispersion relation with the gate voltage, $\zeta - V_{bg}$, can be
extracted according to the tunneling spectrum in Fig. 4.16. A schematic $\zeta - V_{bg}$
dispersion diagram is shown in Fig. 4.18. The texts "0" and "π" indicate that
the Josephson quantum dot is a "0"-junction or "π"-junction in the corresponded
diamond. The two ABSs cross at the phase-transition points (indicated by "QPT"
in the figure). As the gate voltage goes away from the QPT point, ABSs merge
with the quasi-particle continuum at $\pm\Delta$.

4.4.3 SGS in Josephson QD with Kondo effect

When a quantum dot with an odd occupation is strongly coupled to its con-
tact(s), a spin-exchange process will lead to the formation of a spin-singlet in
the dot-lead(s) system [Fig. 4.19 (a)]. This is the Kondo effect as we described
earlier. However, complexity increases when the coupled contacts are replaced
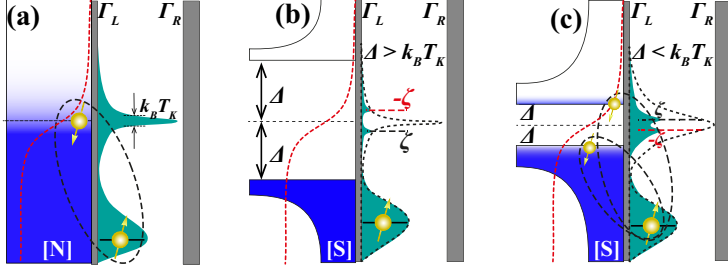
Figure 4.19: Schematic of a Josephson quantum dot with the Kondo effect. (a) Normal contact coupled quantum dot with the Kondo effect. The spin in the quantum dot forms a spin-singlet state with the electrons at the Fermi level of the contact, via a spin-flip process. The spin on the quantum dot gets screened by the Kondo effect. (b) The competition between the Kondo effect and the superconductivity. The Kondo effect will be suppressed if $k_B T_K < \Delta$, because there is no free electron in the uncertainty-principle defined energy window at the Fermi level of the superconductor, to form a spin-singlet with the spin on the dot. The superconductor-QD system is therefore a "π"-junction. (c) The Kondo effect survives if $k_B T_K > \Delta$, when the spin-flip dominates over electron pairing. A spin-singlet is formed and the system becomes a "0"-junction. The dashed lines in (b) and (c) represent the DOSs in the dot when the lead is in a normal state.

by superconductors. At the Fermi level of the superconductors, electrons with opposite spins pair up into Cooper pair spin-singlets and the pairing potential opens an energy window of 2Δ in the quasi-particle DOS. If the energy scale of the Kondo effect $k_B T_K$ is smaller than Δ, no free electrons are available at the Fermi levels of the leads to screen the magnetic spin on the dot. Cooper pairs with zero spin cannot screen the $-\frac{1}{2}$ magnetic impurity either. Therefore, the Kondo effect is suppressed [Fig. 4.19 (b)]. On the other hand, if the dot-lead exchanging energy is larger than the superconducting energy gap, the spin-flip then dominates over the electron pairing, and the magnetic impurity remains screened [Fig. 4.19 (c)]. As a result, the odd-occupied Josephson QD with $k_B T_K < \Delta$ is a "π"-junction due to the unscreened spin on the dot, while the odd-occupied Josephson QD with $k_B T_K > \Delta$ is a "0"-junction. Consequently, the ABSs formed in the Josephson QD with $k_B T_K > \Delta$ are reversed compared with the Josephson QD with $k_B T_K < \Delta$, i.e., the electron-like ABS and the hole-like ABS exchange their positions in the energy spectrum.

Figure 4.20 shows the measurements performed for Dev. *AlInSbAl#3* with

side-gate voltages $V_{g1} = -1$ V and $V_{g2} = 1$ V. In the V_{bg} region shown in the figure, the dot is odd-occupied and is associated with a high-T_K Kondo effect. The device is first characterized in its normal state. As shown in Fig. 4.20 (a), in the charge stability diagram measured at $B = 30$ mT, the Kondo ridge at zero-bias is visible. The superimposed white line is the $dI_{sd}/dV_{sd} - V_{sd}$ line-cut taken at the place indicated by a ★, i.e., the center of the Coulomb diamond. The Kondo effect induced zero-bias conductance peak has a half-width-of-half-maximum (HWHM) of 0.35 meV, which can be used as a approximate estimation of the Kondo temperature $k_B T_K \approx 0.35$ meV. Therefore, $k_B T_K > \Delta = 0.157$ meV. The coupling asymmetry ratio $\chi = \min{(\Gamma_L, \Gamma_R)}/\max{(\Gamma_L, \Gamma_R)}$ can be estimated according to the relation:

$$G_{\max} = \frac{2e^2}{h} \frac{4\Gamma_R \Gamma_L}{(\Gamma_R + \Gamma_L)^2} = \frac{2e^2}{h} \frac{4\chi}{(1+\chi)^2} \quad (\chi \leq 1) \tag{4.11}$$

in which $G_{\max}$ is the zero-bias conductance in the center of the Coulomb diamonds (the electron-hole symmetry point). Here, the $G_{\max} = 0.42e^2/h$ and therefore $\chi \approx 0.06$, indicating the dot-leads coupling are very asymmetric.

In Fig. 4.20 (b), the lead superconductivity is turned on at $B = 0$ mT. The superconductivity-induced conductance SGS emerges at the low-bias region of the charge stability diagram. For clarity, Fig. 4.20 (c) shows a few $dI_{sd}/dV_{sd} - V_{sd}$ line-cuts taken at the points indicated by A, B and C in Fig. 4.20 (b). The diagram and line-cuts show that in the even occupation region, the SGS is dominated by the first-order and second-order MAR features. Conductance peaks appear around $V_{sd} = \pm 2\Delta/e$ and $\pm \Delta/e$. In the odd occupation regime, however, the SGS becomes subtle. The conductance peaks at $V_{sd} = \pm 2\Delta/e$ are missing, while conductance peaks at $V_{sd} = \pm \Delta/e$ are enhanced both in height and width. Moreover, two small inner conductance peaks emerge at $V_{sd} = \pm 10\mu$V with a close-up view shown in Fig. 4.20 (d).

To fully understand the SGS in the odd occupation regime, the Kondo effect, ABSs and MARs all have to be taken into account. The mechanisms, which can induce enhanced conductance peaks at $V_{sd} = \pm \Delta/e$ will be discussed systematically in the next subsection. For this device, we only focus on the signatures of ABS. In Fig. 4.20 (b), the dashed lines indicate the ABSs signatures probed by the DOS singularities in the weakly-coupled superconductor (the probing lead). The two small inner peaks in Fig. 4.20 (d) are the ABSs signatures probed by the residual DOS in the probing lead. The separation in V_{sd} between the high conductance peak and the small conductance peak with the same V_{sd} sign is about

Δ/e, which is consistent with our assumption.

Although the quantum dot transforms from even occupation to odd occupation, the QPT, i.e., ABSs crossing at zero-bias as in Fig. 4.16 is missing. This is due to the Kondo effect which screens the spin on the dot. Therefore, the junction does not experience a "0-π" phase transition, as indicated by Fig. 4.20 (g) where the ABS energy diagram as a function of V_{bg} is schematically shown. To prove this assumption, we performed magnetic field dependence measurements. Figure 4.20 (e) displays the low-energy differential conductance on a color scale as a function of V_{sd} and a perpendicularly applied magnetic field B, at $V_{bg} = -332$ mV [indicated by the dashed line in Fig. 4.20 (d)]. A few $dI_{sd}/dV_{sd} - V_{sd}$ line-cuts taken from Fig. 4.20 (e) at points *D, E* and *F* are also shown in Fig. 4.20 (f) for clarity. The magnetic field dependence diagram and line-cuts show that the two inner conductance peaks cross at $B = \sim \pm 2$mT and split again afterwards. This can be explained as the magnetic field induced QPT (80). The applied magnetic field lifts the spin-degeneracy of the quantum level in the dot by Zeeman splitting. As we discussed in Chapt. 3, the spin-flip process is then significantly suppressed, and therefore the spin-singlet state degrades to a magnetic-doublet state. As a result, the magnetic field drives the Josephson QD from a "0"-junction to a "π"-junction and the QPT occurs at a finite magnetic field. Note that the field-induced QPT leads to the emergence of a zero-bias conductance peak at a finite magnetic field. We will show in the next chapter that this zero-bias peak can mimic the Majorana bound states in some cases, and therefore special attentions should be paid to it. The ABS energy diagram as a function of B is schematically shown in Fig. 4.20 (h). The field-evolution of the inner conductance peaks is again consistent with the assumption of ABS.

We note that there are also conductance peaks/plateaus at $V_{sd} = \pm \Delta/e$ and $V_{sd} = \pm \frac{1}{2}\Delta/e$ in Figs. 4.20 (b) and (c), which can be attributed to the second-order and the forth-order MARs.

The measurements in Fig. 4.20 reveal that the odd-occupied Josephson quantum dot with strong Kondo effect can screen the $-\frac{1}{2}$-spin on the dot, and make the odd-occupied QD a "0"-junction. What about a Kondo effect with medium strength, i.e., $k_B T_K \approx \Delta$? A reasonable prediction is that the Kondo effect will drive the "π"-junction towards the "0"-junction, but whether the phase transition can be completed or not depends on the relations among Γ, Δ and E_C. As an example, we discuss the measurements shown in Fig. 4.21 which were performed
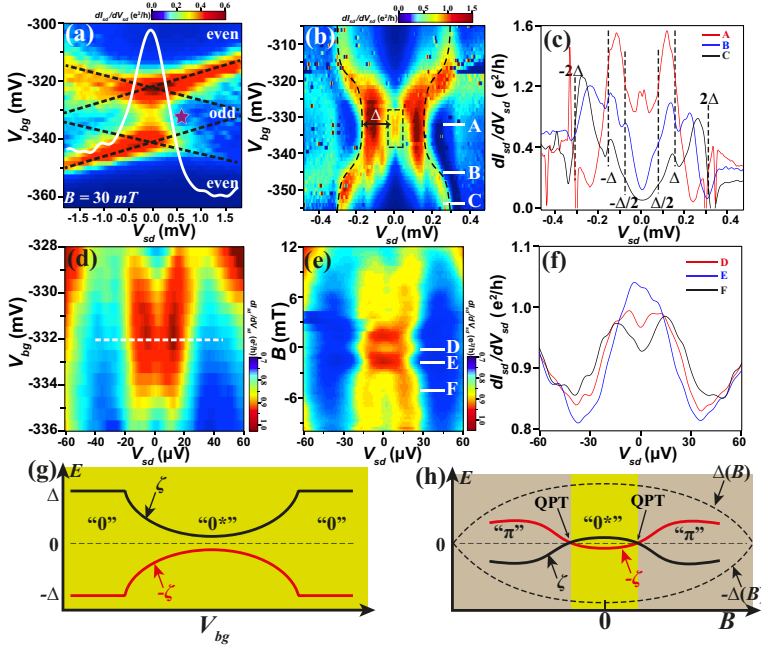
Figure 4.20: SGS of a Josephson quantum dot with a strong Kondo effect. (a) The charge stability diagram measured for Dev. *AlInSbAl#3*, at $B = 30$ mT and with side-gate voltages $V_{g1} = -1$ V and $V_{g2} = 1$ V. The system is in its normal state. The zero-bias Kondo ridge is visible. The superimposed white line is the $dI_{sd}/dV_{sd} - V_{sd}$ line-cut taken at the position indicated by ★. (b) The low-bias region of the charge stability diagram in (a) but with $B = 0$ mT, i.e., the device is in its superconducting state. (c) The $dI_{sd}/dV_{sd} - V_{sd}$ line-cuts taken from (b) at the points indicated by *A,B* and *C*. The diagram in (b) and line-cuts in (c) show an even-odd alternation of the conductance SGS. In the even occupation region, the SGS is dominated by the first-order and the second-order MAR features. In the odd occupation, the SGS is composed of ABS-features superimposed with MAR signatures. Although the quantum dot transforms from even occupation to odd occupation, the QPT is missing. This is due to the Kondo effect which screens the spin on the dot and a spin-singlet ground state is formed in the dot-lead system. Therefore, the junction does not experience a "0-π" phase transition. (d) A zoomed-in view of the squared region in (b). There are two inner high-conductance lines at $V_{sd} = \pm 10\mu$V, which can be attributed to the residual normal DOS probed ABSs. (e) Differential conductance in the low-bias region on a color scale, as a function of V_{sd} and a magnetic field B applied perpendicularly to the substrate, at $V_{bg} = -332$ mV [indicated by the dashed line in (d)]. (f) The $dI_{sd}/dV_{sd} - V_{sd}$ line-cuts taken from (e) at points *D, E* and *F*. The diagram in (e) and line-cuts in (f) show the inner high-conductance lines in (d) cross at $B = \sim \pm 2$mT and split again afterwards. This can be explained as the magnetic field induced QPT when the singlet state changes to magnetic doublet as the spin-degeneracy is lifted. (g) and (h): Schematic diagram of ABS energy in this case, as a function of V_{bg} and B, respectively.

for Dev. *AlInSbAl#3* in a region with a medium dot-leads coupling.

Figure 4.21 (a) displays the charge stability diagram at $V_{g1} = V_{g2} = 0$ V and $B = 30$ mT[1]. The Kondo ridge at zero-bias is visible. According to the HWHM and the peak heigh of the conductance ridge at the center of the Coulomb diamond, the Kondo temperature of this region is estimated to be $T_K \approx 1.5$ K and the coupling asymmetry ratio to be $\chi = 0.09$. Again, the device is asymmetrically coupled to the superconductors. The Kondo energy is therefore $k_B T_K = 0.13$ meV. In Fig. 4.21 (b), the lead superconductivity is turned on at $B = 0$ mT. The SGS features emerge in the low-bias region. A zoomed-in view of the SGS in the low-energy regime is shown in Fig. 4.21 (c) on a color scale, and in Fig. 4.21 (d) in the form of line-cuts. The even-odd alternation of SGS is evident. In the even-occupied region, the first-order and the second-order MAR signatures dominate the SGS. In the odd-occupied region, the ABS signatures and the MAR signatures are both visible. For clarity, we superpose guiding lines of different signatures on the charge stability diagram in Fig. 4.21 (e) with a different color scale . The first-order, the second-order and the forth-order MAR signatures are indicated by the dashed lines at $V_{sd} = \pm 2\Delta/e$, $V_{sd} = \pm\Delta/e$ and $V_{sd} = \pm\frac{1}{2}\Delta/e$, respectively. The singularity probed and normal DOS probed ABS signatures are indicated by open-circles and open-squares, respectively. We see that the ABS signatures show two nested brackets-like shapes, and the inner pair crosses at the resonant points. This indicates that the Josephson quantum dot is a "π"-junction in the odd-occupied Coulomb diamond, and QPT occurs at the resonant points where the quantum dot changes from even-occupied to odd-occupied. However, in the presence of the Kondo effect, the energies of the ABSs are lowered, i.e., they do not merge into the quasi-particle continuums as in Fig. 4.16. A schematic diagram of the energies of ABSs as a function of gate voltage is shown in Fig. 4.21 (f).

So far, we have demonstrated the ABSs in the quantum dots that are weakly, strongly and medially coupled to superconductors, respectively. In the odd-occupied Coulomb diamonds, these ABS signatures exhibit different behaviors which are strongly dependent on the dot-lead(s) coupling. In Fig. 4.22, we will show the evolution of the ABS signatures with a continuously-scaled dot-lead(s)

---

[1]Note that the measurements were performed in the fridge after a warming-up and cooling-down process, compared with the above measurements performed for this device. A warming-up/cooling-down process rearranges the background charge-distribution of the measurement substrate, and the device may show different gate response.
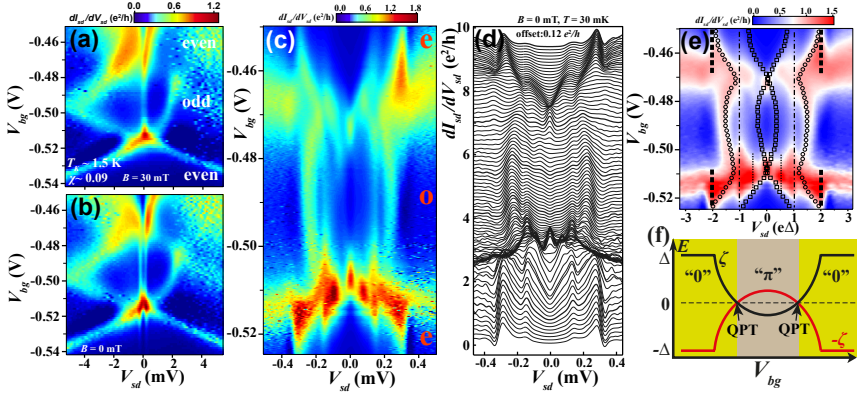
Figure 4.21: ABS signatures and MAR signatures in a Josephson quantum dot with the Kondo effect of medium strength. (a) The charge stability diagram measured for Dev. *AlInSbAl#3*, at $V_{g1} = V_{g2} = 0$ V, and $B = 30$ mT (normal state). The Kondo ridge is visible with $T_K \approx 1.5$ K and coupling asymmetry ratio $\chi = 0.09$. (b) The same as (a), but measured at $B = 0$ mT. The SGS emerge when the lead superconductivity is turned on. (c) A zoomed-in view of the SGS in the low-energy regime. (d) The same as (c) but in the form of line-cuts. Adjacent line-cuts are offset sequentially by 0.12 e^2/h for clarity. The even-odd alternation of SGS is evident in both (c) and (d). The ABS signatures and MAR signatures are both visible. (e) The same as (c) but in a different color scale. (f) The schematic energy diagram of ABS as a function of gate voltage.

coupling.

For Dev. *AlInSbAl#3*, we can use its two side-gates to control the total dot-lead(s) coupling and the coupling asymmetry. By adjusting the voltages applied on the side-gate #1 (V_{g1}) and the voltage on the side-gate #2 (V_{g2}), we can keep the chemical potential of the quantum dot at the center of a Coulomb blockade region with an odd occupation, but vary the dot-lead(s) coupling. Figure 4.22 (a) shows a phase-diagram of the two side-gates measured for Dev. *AlInSbAl#3*, i.e., the linear-response conductance on a color scale as a function of V_{g1} and V_{g2}. The measurements are performed at $V_{bg} = -0.5$ V and $B = 200$ mT. The dashed line is an equipotential line that corresponds to the center of a Coulomb blockade region with an odd occupation. The charge stability diagram with respect to V_{bg} in Fig. 4.21 (a) corresponds to the position indicated by ★ in Fig. 4.22 (a), at $V_{g1} = V_{g2} = 0$ V. The Kondo ridges in the normal state that were measured along this equipotential line are shown in Fig. 4.22 (b). T_K can be estimated according to the HWHM of the Kondo peaks. It is clear to see that T_K increases from 1.6 K to 2.7 K, as V_{g1} gets more positive and V_{g2} gets more negative. The corresponding evolution of the SGS measured at $B = 0$ mT is displayed in Fig. 4.22 (c). The signatures of the ABSs probed by the quasi-particle DOS singularities are visible and are indicated by the solid lines. The dashed lines are the guide lines to show normal DOS probed ABSs signatures which are only partly visible. It is evident that the ABS energies decrease as T_K increases, which is consistent with our expectation. A QPT occurs at the point indicated by ★, where the electron-like and the hole-like ABSs merge together, associated with a zero-bias conductance peak. The schematic diagram of the ABS energies as a function of T_K is shown in Fig. 4.22 (d). Note that the T_K at the QPT point is 2.1 K, which is higher than the theoretically predicted value of $\Delta/k_B \approx 1.8$ K. We attribute the inconsistency of T_K at the QPT to the systematic deviation of the estimation method of T_K[1].

4.4.4 Kondo effect enhanced Δ-peaks

We summarize several low-energy charge stability diagrams in Fig. 4.23, in which Figs. 4.23 (a), (d) and (g) have already been discussed earlier. All measurements are performed in the odd-occupied Coulomb blockade regions of Dev. *AlInSbAl#3* at $B = 0$ mT, $T = 25$ mK and different gate voltage configurations. Tuned by

---

[1]T_K is extracted according to the HWHM of the Kondo ridge that was measured at $B = 30$ mT. However, the Kondo peak may be broadened by the magnetic field due to the large effective g-factor.
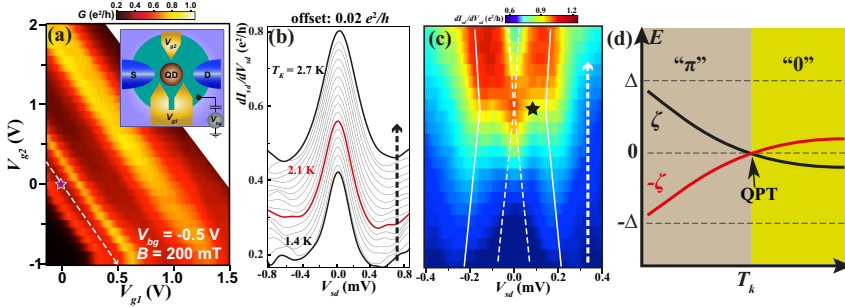
Figure 4.22: The ABS evolution with the Kondo temperature. (a) The linear-response conductance on a color scale measured for Dev. *AlInSbAl#3*, as a function of V_{g1} and V_{g2}, at $V_{bg} = -0.5$ V and $B = 200$ mT. The chemical potential of the quantum dot can be controlled by adjusting V_{g1} and V_{g2}. The dashed line is an equipotential line that corresponds to the center of the Coulomb blockade region shown in Fig. 4.21 (a). (b) The Kondo ridges in the normal state that measured along the equipotential line in (a). The values of T_K are estimated according to the HWHMs of the Kondo peaks. Along the arrow, T_K increases from 1.4 K to 2.7 K. (c) The evolution of the SGS along the equipotential line in (a). The superimposed solid lines are the guide lines of the singularity-probed ABS signatures, while the dashed lines are the guide lines of the normal DOS probed ABS signatures which are not visible here. The coupling controlled QPT occurs at the point indicated by ★. (d) The schematic diagram of the ABS energy as a function of the Kondo temperature T_K.

V_{g1}, V_{g2} and V_{bg}, these diamonds are associated with different Kondo temperatures and different coupling asymmetry ratios. The values of T_K and χ are estimated according to the HWHMs and peak heights of the Kondo ridges in the normal state. Generally, the right-upper diagrams in Fig. 4.23 correspond to higher T_K values and larger χ values, while left-lower diagrams correspond to lower T_K values and smaller χ values.

In almost all of the diagrams in Figs. 4.23 [except (g)], pronounced conductance peaks show up around $V_{sd} = \pm\Delta/e$. Moreover, in the diagrams with stronger and more symmetric coupling [(b), (c), (e), (f) and (i)], the differential conductance peaks emerge at zero-bias voltage and run through the whole Coulomb diamond of odd occupation. These features all strongly depend on the Kondo resonance.

These conductance peaks at $V_{sd} = \pm\Delta/e$ have been detected routinely in odd-occupied Josephson quantum dots with moderate dot-lead(s) couplings (87, 88, 89, 90, 91), and are often referred to as the Δ-peaks. However, there are still a lot of argument and debate about the physical origin of the Δ-peaks.

For the Josephson quantum dot with asymmetric coupling, Refs. (88, 89) state that the Δ-peaks could be caused by the hidden Kondo DOS peak formed in the dot-lead system. The corresponding schematic is shown in Fig. 4.24 (a). When $\Gamma \geq \Delta$, the Kondo resonance survives in the competition with the superconductivity. If $\Gamma_L \gg \Gamma_R$, the left-side lead contributes more than the right-side lead on screening the spin on the dot. That is to say, with a finite bias voltage, the Kondo DOS peak at the Fermi level of the left-side contact is much larger than the Kondo DOS at the Fermi level of the right-side contact. It looks like the Kondo DOS peak is pinned at the Fermi level of the left-side contact. In this case, the right-side superconductor serves as a tunneling probe. When the quasiparticle DOS singularities of the probing superconductor are aligned with the Kondo DOS peak at the Fermi level of the left-side superconductor, a prominent tunneling current enhancement occurs. The explanation is reasonable when the total dot-leads coupling is strong but very asymmetric.

Another argument is that the Δ-peaks are due to the ABS at the QPT point. Here, we would like to explain the sub-gap bound states induced Δ-peaks from another point of view, which is described in terms of the Kondo model rather than the Anderson model (91, 92) for a spinful Josephson quantum dot.

In bulk superconductors, magnetic impurities will give rise to the localized Yu-
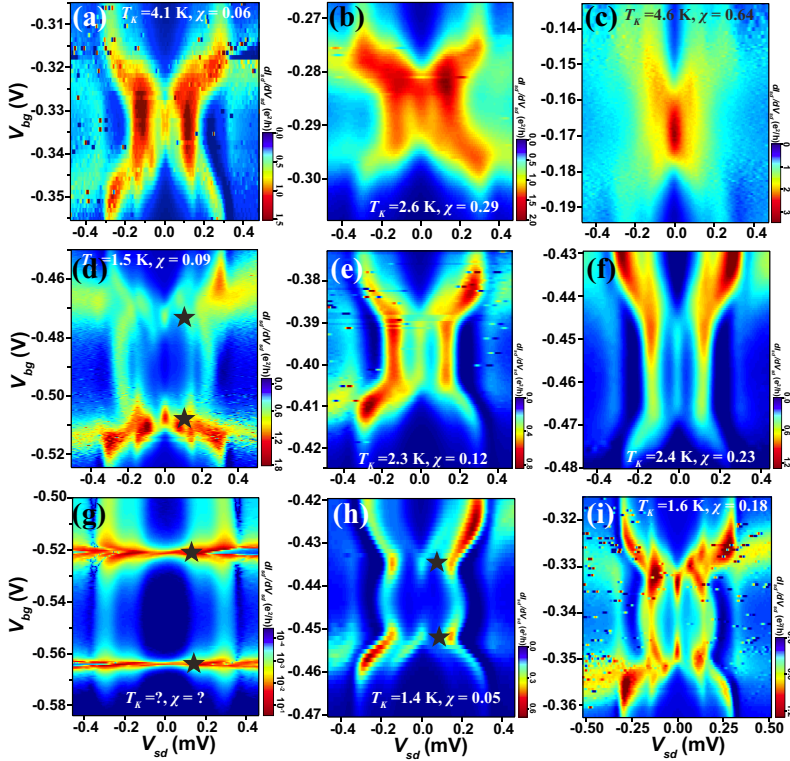
Figure 4.23: The low-energy charge stability diagrams measured for Dev. *AlInSbAl#3*
with different gate-voltage configurations. All measurements are performed at $B = 0$ mT
and $T = 25$ mK. The estimated Kondo temperature T_K and coupling asymmetry ratio χ
are labeled for each diagram except for (h). Generally, right-upper diagrams correspond
to higher T_K values and larger χ values, while left-lower diagrams correspond to lower T_K
values and smaller χ values.
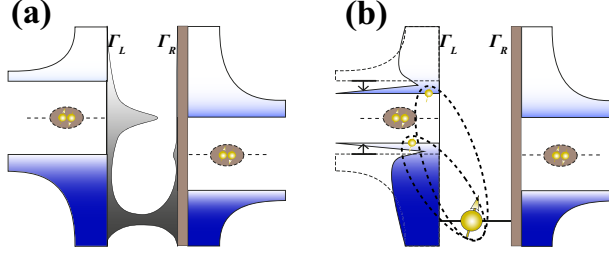
Figure 4.24: The hidden Kondo DOS peak and YSR bound states. (a) The hidden Kondo DOS peak that is pinned to the superconductor on one side may cause two pronounced Δ-peaks. The explanation is reasonable when the total dot-leads coupling is strong but very asymmetric. (b) The formation of Yu-Shiba-Rusinov sub-gap bound states could also induce enhanced Δ-peaks, especially when $k_B T_K \sim \Delta$, i.e., at the QPT point.

Shiba-Rusinov bound states (YSR-states) inside the superconducting gap (93, 94, 95, 96). YSR-states result from a reduced pairing potential near the magnetic impurities. In the vicinity of an uncompensated $-\frac{1}{2}$-spin, it needs smaller energy to break a Cooper pair spin-singlet. Therefore, the quasi-particle DOS singularities at $\pm\Delta$ will move towards the Fermi level by E_x, the exchange energy between the unscreened spin of the magnetic impurity and the quasi-particles in the superconductor. The quantum dot with an odd occupation can reduce the pairing potential in the same way as the magnetic impurity, when it is coupled to superconductors. To lower its energy, the unpaired spin in the quantum dot correlates with the quasi-particles in the superconductor leads via an exchange interaction, which is known as the spin-flip process as we described earlier. This leads to the formation of the sub-gap bound states at $\pm(\Delta - E_x)$ [Fig. 4.24 (b)], similar to the YSR-states in the bulk superconductor with magnetic impurities. The energy scale of the exchange interaction E_x can be reflected by the Kondo temperature T_K. If $k_B T_K \ll \Delta$, the exchange interaction is so weak that there is not much inter-talk between the superconductor and the quantum dot. YSR-states are close to the quasi-particle continuum. As T_K increases, the energies of the YSR-states get lower. In the limit of $k_B T_K \approx \Delta$, the exchange interaction is well-matched with the electron pairing potential in strength. This leads to the merging of the sub-gap bound states at the Fermi level and a complete closing of the quasi-particle excitation gap. When $k_B T_K$ exceeds Δ significantly, the spin-flip wins the competition. However, the magnetic spin in the dot is

get well-screened by the Kondo resonance at the same time, and therefore the quasi-particle excitation gap opens up again, along with the YSR-states moving towards the opposite quasi-particle bands (97).

The crossing and spliting of the YSR sub-gap states as T_K increases are consistent with the QPT in the point of view of the Andreev bound states. When $k_B T_K \approx \Delta$, the YSR-resonance states emerge at the Fermi level of the strongly coupled superconductor. If the dot-leads coupling is asymmetric, Δ-peak will emerge when the quasi-particle DOS singularity is aligned with the YSR-states.

The third proposal is that the prominent Δ-peak can be attributed to the Kondo effect enhanced second-order MAR (87). At a finite bias voltage V_{sd}, Kondo DOS peaks are pinned at the Fermi levels of both superconductor contacts with an energy separation of eV_{sd}. This requires that the dot-lead coupling Γ_L and Γ_R are both large enough to retain Kondo resonance in the non-equilibrium regime. As shown in Fig. 4.25 (a), under $V_{sd} = \pm\Delta/e$, the Kondo DOS peaks overlap with the paths of the second-order MAR[1]. The overlapping reliefs the on-site Coulomb interaction caused tunneling suppression, and opens up two channels for the AR process. Therefore, the second-order MAR is greatly enhanced in contrast to the one in the even-occupied Coulomb diamonds. However, the Kondo DOS peaks do not overlap with the first-order and the third-order MARs, while they partly overlap with the forth-order MAR. Generally, it is predicted that the Kondo DOS should enhance MARs of even-order. This predication is consistent with our measurement results in Figs. 4.20 and 4.21, where Δ-peaks are pronounced and $1/2\Delta$-peaks are visible.

The above three explanations for the enhanced Δ-peaks focus on different physical mechanisms, and the extent of their applications differs with each other. However, the Kondo effect is proven to be critical in all of these arguments. In some cases, comprehensive and unified scopes are needed to explain the Δ-peaks.

4.4.5 Kondo effect enhanced zero-bias peaks

The zero-bias conductance peaks (ZBP) in Figs. 4.23 (b), (c), (e), (f) and (i) can be attributed to the supercurrent enhanced by the Kondo effect. In a voltage-biased measurement setup, ZBP should appear if Cooper pair (co-)tunneling occurs. In fact, in some cases, the ZBP is a more sensitive signature of the supercurrent than the zero-resistance current in current-biased measurements (see SI of

---

[1]In some references, the second-order MAR is referred to as the first-order AR.
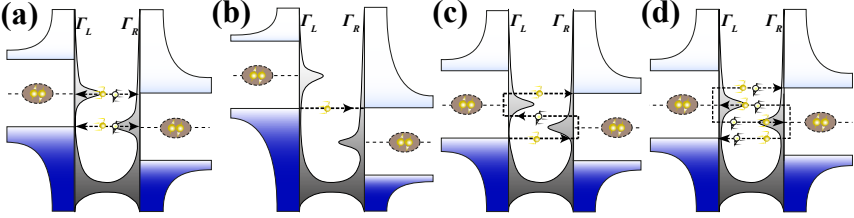
Figure 4.25: MARs correlate with the Kondo effect. (a) The Kondo effect enhanced second-order MAR. Kondo DOS peaks at the Fermi levels of the superconductor contacts open channels for the second-order MAR. (c)-(d) Kondo DOS peaks with the first-order, the third-order and the forth-order MARs, respectively. However, only MARs of even-order can be enhanced by the Kondo effect.

Ref. (98)). Generally speaking, the (co-)tunneling of the Cooper pair through a quantum dot is strongly suppressed due to the on-site repulsive Coulomb interaction. However, the supercurrent is predicted to coexist with the Kondo resonances provided that the Kondo energy $k_B T_K$ is larger than Δ (99, 100, 101). The Kondo resonance increases the electrical transparency of the quantum dot and therefore also promotes the (co-)tunneling of the Cooper pair. The supercurrent enhanced by the Kondo effect has been observed experimentally (102, 103). It was proven in the previous theoretical and experimental work that the energy ratio $k_B T_K / \Delta$ is the key parameter of determining the magnitude of the enhanced Josephson current. Normally, the larger the ratio $k_B T_K / \Delta$ is, the larger the Josephson current I_c is, with an exception at the QPT point, where $|I_c|$ shows an abrupt drop (104).

The values of T_K corresponding to the Kondo valleys in Figs. 4.23 (b), (c), (e), (f) and (i) are 2.6 K, 4.6 K, 2.3 K, 2.4 K, and 1.6 K, respectively. According to our earlier discussion, the Josephson quantum dot is a "0"-junction in the odd-occupied Coulomb diamonds in Figs. 4.23 (b), (c), (e), and (f), whereas it is a π-junction in Fig. 4.23 (i). Despite the different phases-shifts, ZBPs emerge in all of these diagrams. However, we found that the diagram in Fig. 4.23(a) (or in Fig. 4.20) does not show a ZBP, even with a high T_K of 4.1 K. The ZBP missing in the high T_K regime could result from the very asymmetric coupling. Although the quantum dot is strongly coupled to the superconductor contact on one side, leading to a high T_K Kondo resonance, the decoupling between the dot and the superconductor on the other side inhibits the tunneling of Cooper pairs.

To investigate the influence of coupling asymmetry on the ZBP, we activate the two side-gates of Dev. *AlInSbAl#3* and select a region in the $V_{g1} - V_{g2}$ phase-diagram to finely control the asymmetry. The $V_{g1} - V_{g2}$ phase-diagram, i.e., the linear-response conductance on a color scale as a function of V_{g1} and V_{g2} is shown in Fig. 4.26 (a). The measurements are performed at $B = 30$ mT and $V_{bg} = -0.3$ V. Due to the strong coupling, the resonant peaks of the same orbital state merge together, but they split at $B = 0.2$ T because of the Zeeman effect, as shown in the inset colormap of Fig. 4.26 (a). Along the dashed line in Fig. 4.26 (a), the differential conductance as a function of V_{sd} is plotted on a color scale in Fig. 4.26 (b). The coordinated adjustment of V_{g1} and V_{g2} keeps the V_{sd}-sweeping in the center of the Coulomb diamond with an odd occupation. We can see that the Kondo ridge emerges at zero-bias, varying both in magnitude and width. Along the arrow, the value of T_K shows a slight increase from 2.6 K to 3.2 K, but the coupling asymmetry ratio χ decreases from 0.38 to 0.08. We then come to the SGS in the superconducting state in Fig. 4.26 (c). As we predicted, the ZBP only emerges at the region with more symmetric coupling, despite fact that the total coupling is slightly weaker. This indicates that besides the total coupling, the coupling asymmetry is another important parameter for the (co-)tunneling of the Cooper pair.

Special attention should be paid to the ZBPs appearing near the quantum level resonance points, like those points labeled by ★ in Figs. 4.23 (d), (g) and (h). The Kondo resonance has the highest strength near the resonant level, and therefore the supercurrent can be more enhanced by the Kondo correlation. However, ZBP can also be caused by many other mechanisms near the resonant level. Firstly, the single electron resonant level is also a possible supercurrent channel, and therefore the supercurrent transistor effect (105) can be induced. Secondly, crossover of ABS (or YSR) states can also lead to a ZBP in the tunneling regime, as we discussed earlier. Thirdly, a bunch of high-order MARs could get dramatically modified and converge to a ZBP (106) near the resonant level. Finally, the residual quasi-particle resonant tunneling events near the Fermi level can also contribute to the conductance peak, as shown in Fig. 4.7.
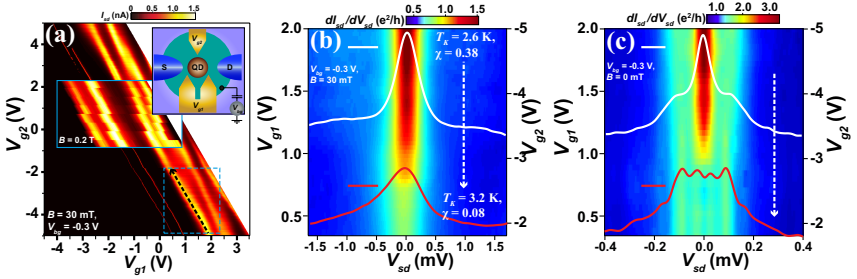
Figure 4.26: The influence of the coupling asymmetry on the ZBP. (a) The $V_{g1} - V_{g2}$ phase-diagram of Dev. *AlInSbAl#3*, i.e., the linear-response conductance on a color scale as a function of V_{g1} and V_{g2}, at $B = 30$ mT and $V_{bg} = -0.3$ V. The inset schematic shows the device layout and the inset colormap is the $V_{g1} - V_{g2}$ phase-diagram in the normal state for the dash-squared region. (b) The differential conductance on a color scale as a function of V_{sd}, along the dashed line in (a). The measurements are kept in the center of the Coulomb diamond with an odd occupation. Along the arrow, the value of T_K shows a slight increase from 2.6 K to 3.2 K, but the coupling asymmetry ratio χ decreases from 0.38 to 0.08. (c) The same as (b) but at $B = 0$ mT. Conductance SGS emerges at the low-bias region. ZBP only appears in the upper region where coupling is more symmetric despite the fact that the total coupling is slightly weaker.

4.5   SGS evolutions with temperature and magnetic field

The conductance SGS can be dramatically modified with the increasing temperature or an increase of the external magnetic field. In this section, we will discuss how SGS evolves as the temperature or the magnetic field increases, by analyzing the measurement results achieved from a few Josephson quantum dot devices.

The first example is selected from the electron transport region of Dev. *AlInSbAl#1*. We first characterize the device in its normal states and its SGS at zero field and base temperature in Fig. 4.27.

Firstly, the device is measured in a voltage-biased setup. Figure 4.27 (a) shows the charge stability diagram measured for the device at $B = 0.2$ T, when the contacts are in their normal states. The Coulomb diamond structure can be identified with the charging energy of $E_c \approx 7$ meV. The Kondo anomaly can be identified near the zero-bias region. However, due to the large effective g-factor of the InSb quantum dot, the Kondo ridge has split at $B = 0.2$ T. The Kondo peaks at different magnetic fields from $B = 70$ mT to $B = 700$ mT, are shown in Fig. 4.27 (b). It is evident that the Kondo ridge starts splitting even at $B = 70$ mT, where the device just transforms from the superconducting state to the normal state ($B_c = 62$ mT for this device). To estimate the Kondo temperature, we have to deduce the line-shape of the Kondo ridge at zero field but with normal contacts. This is done by fit the measured split-Kondo peaks using the method in Ref. (37). The result of the fit is represented by the red-dashed line in Fig. 4.27 (b). Accordingly, the Kondo temperature T_K at the center of Coulomb diamond is determined to be 2.2 K and the coupling asymmetry ratio χ is 0.17. So the relative energy-relations for the odd-occupied diamond can be determined as $E_c \gg k_B T_K \gtrsim \Delta$.

In the superconducting state, the conductance SGS emerges. Figures 4.27 (c) and (d) display the low-energy SGS on a color scale and sequentially offset line-cuts, respectively. A few line-cuts [indicated by *A-D* in Fig. 4.27 (c)] are highlighted in Figs. 4.27 (e) and (f). The SGS exhibits typical even-odd alternation behavior as we described earlier. In the deep blockade region with even occupation [like at point *A* in Fig. 4.27 (c)], only the first-order and the second-order MAR induced peaks are visible. The first-order MAR feature is very sharp and it is even associated with two differential conductance dips with negative values near the two 2Δ-peaks. The areas with negative differential conductance
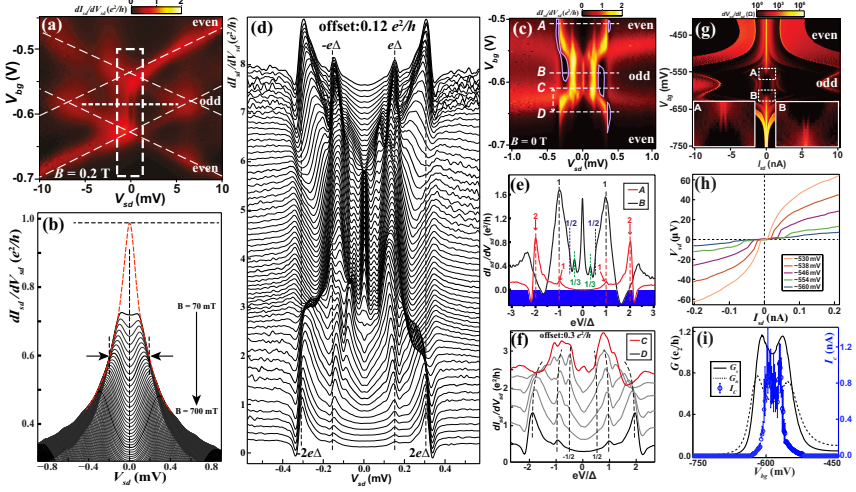
Figure 4.27: The SGS measured for Dev. *AlInSbAl#1*. (a) The charge stability diagram measured for the device at $B = 0.2$ T. The device is in its normal state, and the Coulomb diamond structure can be identified. The Kondo anomaly can be seen clearly at zero-bias. However, the Kondo ridge has already split even at $B = 0.2$ T due to the large effective g-factor of the InSb quantum dot. (b) The differential conductance as a function of V_{sd} performed at $V_{bg} = -585$ mV [the dashed line in (a)] and at different magnetic fields from $B = 70$ mT to $B = 700$ mT. It is evident that the Kondo ridge already starts splitting at $B = 70$ mT, where the device just transforms from the superconducting state to the normal state ($B_c = 62$ mT for this device). The line-shape of the Kondo ridge at zero field but with normal contacts is deduced according to the measured split-Kondo peaks, and is represented by the red-dashed line in (b). Accordingly, the Kondo temperature T_K at the center of the Coulomb diamond is determined to be 2.2 K and the coupling asymmetry ratio χ is 0.17. (c) and (d) show the low-energy SGS of the squared region in (a), on a color scale and in a sequentially offset line-cut plot, respectively. A few line-cuts [indicated by A-D in (c)] are highlighted in (e) and (f). The SGS exhibits typical even-odd alternation behavior. In the deep blockade region with even occupation (like at point A), only the first-order and second-order MAR induced peaks are visible. The first-order MAR feature is so sharp it is even associated with two differential conductance dips with negative values near the two 2Δ-peaks. In contrast, the SGS in the deep blockade region with odd occupation (like at point B) displays two pronounced Δ-peaks but with the 2Δ-peaks missing. A pronounced ZBP and the conductance peaks at $\pm 1/3\Delta/e$ can be also identified. (g) The differential resistance as a function of the applied source-drain current I_{sd} and V_{bg} measured for the device. (h) $V - I$ curves (the measured voltage drop as a function of the applied current) measured in the Kondo valley. It is clear to see that there is a relatively flat part at the low-bias region in each of these curves, which can be attributed to the Kondo effect enhanced Josephson current. (i) The zero-bias conductance measured in the superconducting state G_s and measured in the normal state G_n, and the critical current I_c, as a function of V_{bg}.

(NDC) in Fig. 4.27 (c) are encircled by purple lines, which favors a upper left-lower right diagonal distribution in the stability diagram. The signature of the second-order MAR is much weaker than the signature of the first-order MAR. This is because that the Andreev reflection process is strongly suppressed by the on-site Coulomb interaction.

In contrast, the SGS in the deep blockade region with odd occupation [like at point B in Figs. 4.27 (c) and (e)] displays two strongly enhanced Δ-peaks but the 2Δ-peaks are absent. Outside of the Δ-peaks, pronounced NDC-dips are also clearly seen. The prominent features around Δ should be related with the Kondo effect, as we discussed earlier. According to the energy scale relation $k_B T_K \gtrsim \Delta$, the assumptions of the hidden-Kondo peak, the YSR-states and the Kondo-enhanced second-order MAR all make sense. In addition to the Δ-peaks, a sharp ZBP and the conductance peaks at $\pm 1/3\Delta/e$ are also visible. The ZBP is attributed to the Kondo effect enhanced supercurrent. The $\frac{1}{3}\Delta$-peak could result from the sixth-order-MAR enhanced by the Kondo effect, as we anticipated that the even-order MAR will get enhanced by the Kondo effect. In fact, if we check the line-cut B in Figs. 4.27 (e) carefully, fainter conductance shoulders can be identified at $V_{sd} = \pm 1/2\Delta/e$ on the sharp slopes of Δ-peaks. The shoulders may imply the onset of the fourth-order-MAR process, but it gets absorbed by the nearby Δ-peaks.

Near the resonance point [the line-cut in Fig. 4.27 (f)], the SGS becomes complicated. The conductance peaks or conductance plateaus at $\pm 2\Delta/e$, $\pm \Delta/e$ and $\pm 1/2\Delta/e$ can be identified. These are attributed to the first-order, second-order, and fourth-order MARs. As indicated by the dashed lines, their magnitudes and positions show a clear V_{bg}-dependence. This is because the MAR is modified by the single electron resonance in the dot (106).

The device is then characterized in a current-biased setup. Figure 4.27 (g) shows the measured differential resistance as a function of applied current I_{sd} and V_{bg} measured for the device. The dark region represents the area where the device has a lower resistance. Figure 4.27 (h) shows a few $V - I$ curves, i.e., the measured voltage drop across the junction as a function of the applied source-drain current. The $V - I$ curves are measured in the Kondo valley. It is clear to see that there is a nearly-dissipationless[1] current branch in each of the $V - I$ curves. The nearly-

---

[1]The resistance of the Josephson current here is not strictly zero, which is due to the background resistance in the measurement circuit and due to the fact that the Josephson quantum dot here is

dissipationless current can be attributed to the Kondo effect enhanced Josephson current. We extract the critical current I_c in the Kondo regime and plot it in Fig. 4.27 (i), as a function of V_{bg}, along with the zero-bias conductance measured in the superconducting state G_s and in the normal state G_n. It is evident that I_c is significantly dependent on the Kondo resonance instead of the single electron resonance.

4.5.1   SGS evolution with temperature

We now turn to the SGS evolution with the temperature. As the temperature increases, the SGS of the Josephson quantum dot changes. Firstly, according to Eq. 4.1, the superconducting energy gap Δ decreases as the temperature rises and the superconductivity completely vanishes above the critical temperature T_c. Therefore, all the features related to $\Delta(T)$ will evolve accordingly. Secondly, the single-electron resonance levels, the quasi-particle DOS singularities, and the Kondo ridges will be thermally broadened and smoothed. Therefore, sharp peaks and/or dips in SGS will be flattened. Lastly, the temperature changes the Fermi-Dirac distribution function $f(E, T) = \left[1 + e^{\left(E - E_f\right)/k_B T}\right]^{-1}$, and therefore more electron-like quasi-particles will be activated over $2\Delta(T)$ to another quasi-particle band and leads to new transport features.

Figure 4.28 displays the temperature dependent measurements for Dev. *AlInSbAl#1*. Figure 4.28 (a) shows the differential conductance on a color scale as a function of V_{sd} and T. The measurements are performed in the blockade region with an even occupation, at the position indicated by the dashed line A in Fig. 4.27 (c). The 2Δ-peaks and the Δ-peaks are visible. We extract their positions in V_{sd} and their peak heights, and plot them as a function of T in Figs. 4.28 (b) and (c), respectively. It can be seen that the positions of the 2Δ-peaks and the Δ-peaks bend towards zero-bias and fits well with $\Delta(T)$ and $1/2\Delta(T)$, respectively. The peak magnitudes also decrease as the temperature rises as the superconductivity and Andreev reflections are thermally smeared.

Surprisingly, a ZBP emerges at $T \sim 450$ mK and peaks at $T = 800$ mK. It disappears when the superconductivity disappears above $T = 1$ K. We attribute this ZBP to the thermal-activation enhancement of the quasi-particles. As shown in Figs. 4.28 (g-h), as the temperature increases, Δ shrinks and the two quasi-

---

resistively and capacitively shunted.
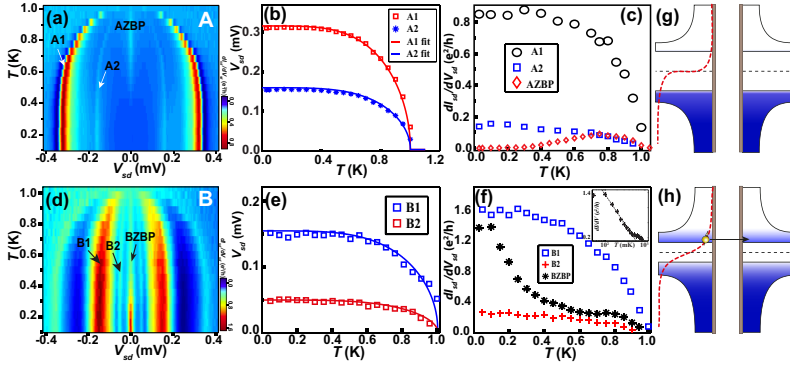
Figure 4.28: The SGS evolution with temperature. (a) The differential conductance on a color scale measured for Dev. *AlInSbAl#1*, as a function of V_{sd} and T, at the position indicated by the dashed line A in Fig. 4.27 (c). (b) The positions of peak *A1* and peak *A2* in V_{sd}, as a function of T. Solid lines are the fit lines of $\Delta(T)$ and $1/2\Delta(T)$, respectively, according to Eq. 4.1 (1). (c) The heights of peak *A1*, peak *A2* and peak *AZBP* as a function of T. (d-f) The same as (a-c) but for the position indicated by the dashed line B in Fig. 4.27 (c). (g) and (h) show the schematics of the influence of the quasi-particle thermal-excitation on the tunneling current.

particle bands move closer. On the other hand, electron-like quasi-particles get more thermally activated (107). As a consequence, more and more electron-like quasi-particles accumulate in the upper quasi-particle band. The quasi-particle band to band tunneling is thereby activated and the ZBP develops.

Figures 4.28 (d-f) show similar measurements as Figs. 4.28 (a-c), but measured in the blockade region with odd occupation, at the position indicated by the dashed line B in Fig. 4.27 (c). In this region, Δ-peaks and $1/3\Delta$-peaks exhibit the same tendency as the peaks in the even-occupied region, and their positions in V_{sd} and peak heights both decrease as $\Delta(T)$.

Although the Kondo-effect enhanced ZBP also decreases in magnitude, it shows a different line-shape than other peaks in Figs. 4.28 (f). In contrast to the slow drops of the Δ-peak and the $1/3\Delta$-peak, the ZBP shows a dramatic decrease at $T < 500$ mK[1]. The inset plot of Fig. 4.28 (f) shows the height of the ZBP but on a logarithmic temperature scale, and it is clear to see the negative

---

[1]Below $T = 150$ mK, the ZBP and other conductance peaks do not show any significant change due to the electron temperature saturation.
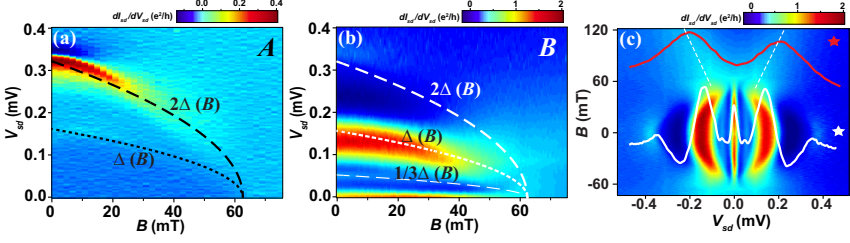
Figure 4.29: The SGS evolution with the magnetic field. (a) The differential conductance on a color scale measured for Dev. *AlInSbAl#1*, as a function of V_{sd} and B, at the position indicated by the dashed line A in Fig. 4.27 (c). The fit lines of $2\Delta(B)$ and $\Delta(B)$ are superimposed. (b) The same as (a), but at the position indicated by the dashed line B in Fig. 4.27 (c). The fit lines of $\Delta(B)$, $\Delta(B)$ and $\frac{1}{3}\Delta(B)$ are superimposed. (c) The same as (b), but in a larger B scale. Two $dI_{sd}/dV_{sd} - V_{sd}$ line-cuts are superimposed, which are taken at the position indicated by ★s .

linear slope in the range of $T = 150 - 700$ mK. This is consistent with the fact that the ZBP is greatly dependent on the Kondo effect. As we discussed in Chapt. 3, the negative linear slope in the $G - log(T)$ curve is a typical feature of the temperature dependence of the Kondo effect. Therefore, the Kondo effect enhanced ZBP could show the same tendency. Note that the height of the ZBP shows a small recovery in the range of $T = 700 - 950$ mK, and it can be attributed to the shadow-effect of the quasi-particle thermal-activation, similar to that of the ZBP shown in Fig. 4.27 (c).

4.5.2 SGS evolution with magnetic field

The magnetic field can modify the SGS of a Josephson quantum dot in many aspects. First, the magnetic field leads to the closing of Δ and all the SGS features related to $\Delta(B)$ evolve accordingly. Second, the magnetic field induces the Zeeman effect, which splits the spin-degenerated quantum levels. The lifting of the spin degeneracy can lead to the splitting of the Kondo ridge and a "0-π" quantum phase transition. The Zeeman effect can also change the on/off resonance status of the quantum dot, especially for a quantum dot with a large effective g-factor.

In Fig. 4.29, the SGS field evolution of Dev. *AlInSbAl#1* is shown. Figure 4.29 (a) displays the differential conductance on a color scale measured for

Dev. *AlInSbAl#1*, as a function of V_{sd} and B. The measurements are performed in the blockade region with an even occupation, at the position indicated by the dashed line A in Fig. 4.27 (c). It can be seen that both the 2Δ-peak and the Δ-peak bend towards zero-energy as the magnetic field increases. According to Eq. 4.1 (2), $2\Delta(B)$ and $\Delta(B)$ are plotted and superimposed on the colormap, and they fit well with the 1_{st} and 2_{nd} MAR features, respectively. As expected, the magnitudes of the 2Δ-peak and the Δ-peak also decrease as the magnetic field increases.

The SGS field evolution for the blockade region with odd occupation is shown in Figs. 4.29 (b) and (c). The measurements are performed at the position indicated by the dashed line B in Fig. 4.27 (c). The fit lines of $2\Delta(B)$, $\Delta(B)$ and $\frac{1}{3}\Delta(B)$ are superimposed on Fig. 4.29 (b). Again, we can see that all the MAR peaks evolve with $\Delta(B)$ even when they have a correlation with the Kondo effect. Figure 4.29 (c) shows the SGS evolution in a larger B scale. The Kondo peak can be identified when the superconductivity vanishes at $B > 62$ mT, when the Kondo ridge has already split.

The SGS field evolution of Dev. *AlInSbAl#1* mainly shows that they are modified as Δ decreases with the magnetic field. As we mentioned, a magnetic field can also modify the SGS in other ways.

We have demonstrated the magnetic field induced QPT in an odd-occupied quantum dot but with a spin-singlet ground state [Fig. 4.20 (c)]. In contrast, the ABS in a "π"-junction quantum dot should show a split due to the Zeeman effect (80). An example is given in Figs. 4.30 (a-c). Figure 4.30 (a) illustrates the measured SGS of Dev. *AlInSbAl#3* which has been shown in Fig. 4.23 (h). The guide lines of the quasi-particle DOS singularity probed ABS signatures and the residual normal DOS probed ABS signatures are superimposed. According to the bracket-like shape of the ABS signatures, it is clear that the Josephson quantum dot is a "π"-junction in the center of the blockade region with an odd occupation. Figure 4.30 (b) shows the SGS field-evolution at the position indicated by the dashed line in Fig. 4.30 (a), and the squared region is shown in the 3D zoomed-in plot in Fig. 4.30 (c). As expected, the ABS shows a split in the magnetic field. The splitting of the ABS signatures is limited by the quasi-particle continuum which is defined by $\Delta(B)$. Again, the split Kondo peaks emerge when the superconductivity is quenched by the magnetic field.

Figures 4.30 (d-f) illustrate the SGS evolution in a magnetic field for three
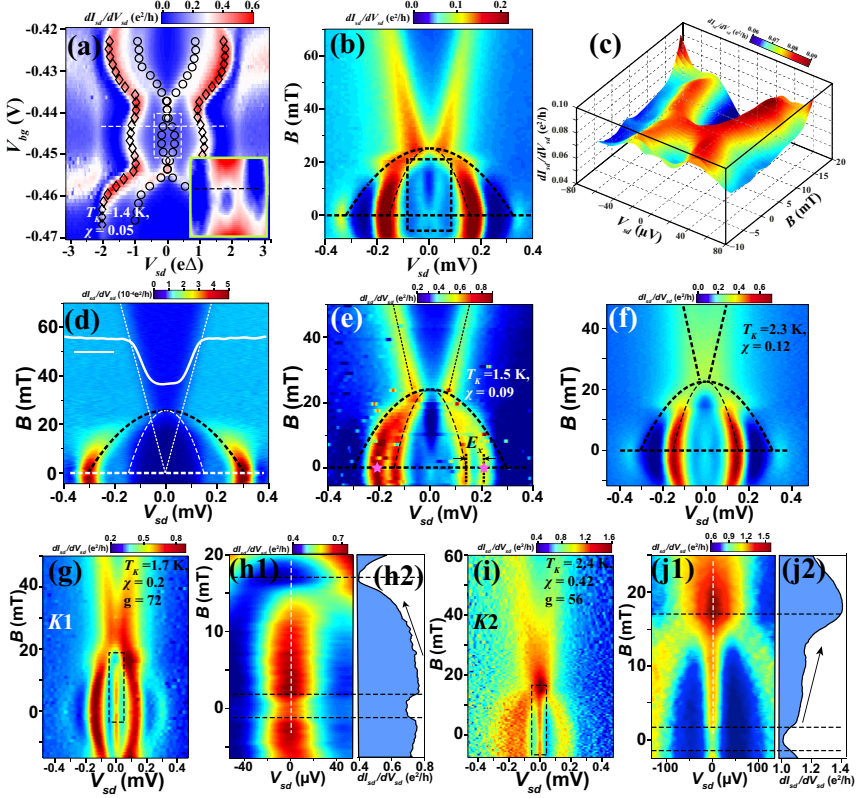
Figure 4.30: The SGS evolution in a magnetic field. (a) The charge stability diagram which is the same as Fig. 4.23 (h) in a different color scale. The guide lines for DOS singularity probed ABS signatures (diamonds) and residual normal DOS probed ABS signatures (circles) are superimposed. The inset is a close-up view of the squared region, in which normal DOS probed ABS is visible. (b) The differential conductance on a color scale as a function of V_{sd} and B, measured at the position indicated by the dashed line in (a). The fit lines of $2\Delta(B)$ and $\Delta(B)$ are superimposed. (c) A 3D zoomed-in view of the squared-region in (b). (d-f) The same as (b) but measured at three different odd-occupied diamonds. They are measured at the centers of the odd-occupied diamonds in Figs. 4.23 (g), (d) and (e), respectively. (g) The same as (b), but measured for Dev. *AlInSbAl#2*, in an odd-occupied Coulomb diamond. (h1) A close-up view for the squared region in (g). (h2) The zero-bias differential conductance as a function of B, taken in (h1) along the dashed line. (i), (j1) and (j2) are the same as (g), (h1) and (h2), respectively, but measured at a different odd-occupied Coulomb diamond of Dev. *AlInSbAl#2*.

odd-occupied Coulomb diamonds with different T_Ks. They are taken from the diamonds shown in Figs. 4.23 (g), (d) and (e), respectively.

The quantum dot in Fig. 4.30 (d) is associated with the lowest T_K, in which the coupling is so weak that no Kondo features can be identified. Although the quantum dot is odd-occupied, its SGS does not show any typical odd-occupied behavior such as the enhanced Δ-peaks or the emergence of a ZBP. Due to the weak exchange interaction, the sub-gap bound state is close to the quasi-particle continuum and only weak first-order and second-order MAR signatures are visible. The field evolution of these weak MARs only show monotonic decrease with $\Delta(B)$.

As the Kondo correlation gets stronger in Fig. 4.23 (e), the exchange interaction drives the sub-gap bound state towards the Fermi level, to an energy of $E_b = \Delta - E_x$. As indicated by the ★, the sub-gap bound state is probed by the quasi-particle DOS singularity of the superconductor on other side and induces two conductance peaks at $\pm |\Delta + E_b| /e$. For the bound state with $0 < E_b < \Delta$, its induced conductance peak does not follow $2\Delta(B)/e$ or $\Delta(B)/e$ in a magnetic field. However, the conductance peaks at $\pm\Delta/e$ in Fig. 4.30 (e) show a good fit with $\pm\Delta(B)/e$, and is therefore consistent with our assumption that they are attributed to the Kondo effect enhanced second-order MAR.

In Fig. 4.30 (f), the Kondo energy $k_B T_K$ just exceeds Δ and therefore $E_b \approx 0$. Similar to the measurements in Figs. 4.29 (b) and (c), the field evolution of the SGS in Fig. 4.30 (f) mainly exhibits the monotonic decrease of the Δ-peaks with $\Delta(B)$.

Lastly, we check the influence of the magnetic field on the ZBP which is induced by the Kondo effect enhanced supercurrent. As pointed out earlier, the magnitude of the Kondo effect enhanced Josephson current is mainly determined by the energy ratio $k_B T_K/\Delta$. The magnetic field smears both the Kondo resonance and Δ, and therefore the field evolution of the Josephson current should depend on whether the degrading of the Kondo effect is faster than the degrading of Δ in the magnetic field (108). The degrading of Δ is determined by the Eq. 4.1 (2), however, the decreasing of the Kondo resonance depends on T_K and the effective g-factor of the quantum dot. According to theoretical prediction (37), the higher T_K is and the smaller the effective g-factor is, the higher the splitting threshold field is (36), and therefore the slower the Kondo resonance degrading is.

Figures 4.30 (g-j) show the measurements for another Al-contacted InSb quan-

tum dot device, Dev. *AlInSbAl#2*, with the same geometry as Dev. *AlInSbAl#3*. In these measurements, two different evolutions of the Kondo effect enhanced Josephson current in two Kondo valleys (*K1* and *K2*) are illustrated. The field evolutions of SGS in two odd-occupied Coulomb diamonds are shown in Figs. 4.30 (g) and (h). With different T_K, χ and g-factors, Kondo effect enhanced ZBPs appear in both regimes. The highlighted ZBP structures and their corresponding zero-bias conductance as a function of B are displayed in Figs. 4.30 (h) and (j). It is evident that the height of the ZBP in valley *K1* decreases in the range of $B = 3 - 17$ mT, whereas the ZBP of the valley *K2* shows a clear increase in the same range of the magnetic field.When compairing the T_K values and effective g-factors of *K1* and *K2*, we found $T_{K1} < T_{K2}$ and $|g_1^*| > |g_2^*|$, which is consistent with our expectation. However, we are aware that there could be other affecting parameters such as χ or E_c to complicate the competition between the Kondo effect and Δ.

4.6 Anomalous low-field suppression of the zero-bias conductance peak in Josephson QD devices

We have shown that the Josephson current in a single junction decreases as the applied magnetic field increases. However, after careful checking the Josephson current induced ZBPs in Fig. 4.29 (c) and Figs. 4.30 (g-j), we found that the ZBPs do not reach their maxima at $B = 0$ mT. Instead, there are conductance valleys or dips in the low-field region[$B = -20 - 20$ mT in Fig. 4.29 (c) and $B = -3 - 3$ mT in Figs. 4.30 (g-j)]. We will see in this section that the exotic field-response of the ZBPs in the low-field region has been routinely observed in our InSb nanowire based Josephson quantum dots.

In Fig. 4.31 (a), a close-up view of the ZBP region of Fig. 4.29 (c) is shown. It is evident that the height of ZBP reaches its maximum at $B = \pm 20$ mT, and it is suppressed in the range of $B = -20 - 20$ mT. More clearly, Fig. 4.31 (b) displays the measured source-drain current I_{sd} in the same region, as a function of B, at different V_{sd} from 2 μV to 38 μV. For each $I - B$ curve, a current valley shows up in the range of $B = -20 - 20$ mT. We define I_P as the maximum current, I_V as the current at $B = 0$ mT, and $I_\Delta = I_P - I_V$ as the depth of the current valley. We then extract I_P, I_V and I_Δ from (b), and plot them in Fig. 4.31 (c), as a function of V_{sd}. Both I_P and I_V increase with V_{sd}, while I_Δ displays a non-monotonical
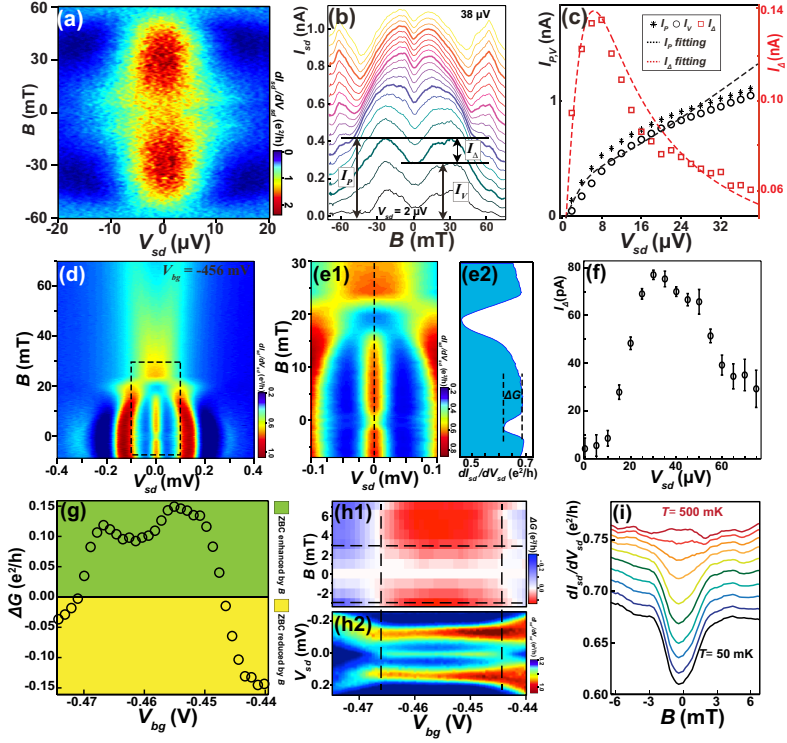
Figure 4.31: The anomalous low-field suppression of the Kondo effect enhanced Joseph-son current in Dev. *AlInSbAl#1* and Dev. *AlInSbAl#3*. (a) A close-up view of the ZBP region in Fig. 4.29 (c). The height of the ZBP in the range of $B = -20 - 20$ mT is sup-pressed. (b) The measured source-drain current I_{sd}, corresponding to (a), as a function of B, at different V_{sd}s from 2 μV to 38 μV. For each $I - B$ curve, we define I_P as the maximum current, I_V as the current at $B = 0$ mT and $I_\Delta = I_P - I_V$. (c) The extracted I_P, I_V and I_Δ from (b), as a function of V_{sd}. The solid lines are the fit lines of I_Δ and I_P according to Eq. 4.12. The line-shape of $I_\Delta - V_{sd}$ shows a typical supercurrent-V_{sd} shape of a small Josephson junction. (d) The differential conductance on a color scale as a function of V_{sd} and B, measured in the Kondo valley in Fig. 4.23 (f). (e1) A zoomed-in view of the squared region in (d). (e2) The zero-bias conductance as a function of B. (f) I_Δ as a function of V_{sd}, extracted for the region shown in (e1). The line-shape of the $I_\Delta - V_{sd}$ curve is similar to the one in (c). (g) The difference between the zero-bias conductance at $B = 3$ mT and the zero-bias conductance at $B = 0$ mT, which is denoted $\Delta G(B = 3mT)$, as a function of V_{bg}. $\Delta G(B = 3mT)$ represents the depth of the conductance dip in the low-field region [see the definition in (e2)]. (h1) $\Delta G(B)$ as a function of B and V_{bg}, com-pairing with the low-energy charge stability diagram in (h2). (i) The same as (f), but at different temperatures from $T = 50$ mK to 500 mK. As the temperature increases, the conductance dip is smeared out.

change as V_{sd} increases. I_Δ first dramatically increases from $V_{sd} = 0\mu V$ to $6\mu V$, and it then decays with a long smooth tail as V_{sd} continues to increase. We found that the line-shape of I_Δ can be fitted very well to a typical $I_s - V$ curve (the Josephson current as a function of V_{sd}) (104, 109, 110), which is described by:

$$
\begin{cases}
I_s\left(V_{sd}\right) = I_c \text{Im} \left[\dfrac{J_{1-i\eta(V_{sd})}(I_c\hbar/2ek_BT)}{J_{-i\eta(V_{sd})}(I_c\hbar/2ek_BT)} \right] \\
I\left(V_{sd}\right) = \dfrac{I_s R_J + V_{sd}}{R + R_J}
\end{cases}
\tag{4.12}
$$

where I_c is the critical current of the Josephson junction, R and R_J are two resistances in a resistively and capacitively shunted junction model (105), $J_\alpha\left(x\right)$ is the modified Bessel function of the complex order α, and $\eta\left(V_{sd}\right) = \hbar V_{sd}/2eRk_BT$. For the fit shown in Fig. 4.31 (c), the parameters are set to be $T = 100$ mK, $I_c = 1.6$ nA, $R = 1.5$ kΩ, and $R_J = 45$ kΩ.

The good correlation between the line-shape of $I_\Delta - V_{sd}$ and the typical $I - V$ curve of Josephson current implies that the current suppression in the low-field region is due to the decrease of the Josephson current. In this case, the Josephson current through a quantum dot is suppressed.

The measurements for Dev. *AlInSbAl#3* also show similar phenomena. Figures 4.31(d-f) display a suppression of ZBP in the range of $B = -3 - 3$ mT. The suppression here is even sharper than the one shown in Figs. 4.31 (a-c), and the zero-bias conductance shows a dip in the low-field region. The suppression also shows the finger-prints of the Josephson current in the $I_\Delta - V_{sd}$ curve in Fig. 4.31 (c), with a similar line-shape as the Josephson $I - V$ curve. We then check the gate-dependence of the low-field suppression. For convenience we denote the differential conductance as a function of V_{bg} and B as $G(V_{bg}, B)$. In Fig. 4.31 (g), we extract $\Delta G = G(V_{bg}, 3mT) - G(V_{bg}, 0mT)$, i.e., the depth of the conductance dip in the low-field region [see the definition in Fig. 4.31(e2)], as a function of V_{bg}. Similarly, $\Delta G(B) = G(V_{bg}, B) - G(V_{bg}, 0mT)$ is shown on a color map in Fig. 4.31 (h1) as a function of B and V_{bg}, along with the low-energy charge stability diagram in Fig. 4.31(h2). We can see that the low-field suppression occurs for all V_{bg} values as long as there is a ZBP at that V_{bg}. Moreover, the dip-depth is relevant to the ZBP height at the zero field. The higher the ZBP at $B = 0$ mT is, the deeper the low-field conductance dip is. The temperature dependence measurements of the low-field suppression is shown in Fig. 4.31 (i), in which the zero-bias conductance as a function of B measured from $T = 50$ mK to $T = 500$ mK is shown.The conductance dip gets shallower as the temperature increases

and is completely smeared out at $T = 450$ mK.

As we have shown in Fig. 4.30 (j), the magnetic field could lead to an increase of the energy ratio $k_B T_K/\Delta$ and therefore increase the Josephson current. However, the low-field suppression of ZBP in Figs. 4.31 (d-i) only occurs below $|B| < 3$ mT, and $k_B T_K/\Delta$ has not yet effectively increased with $\Delta(B = 3mT) \geq 0.98\Delta_0$. Therefore, the low-field suppression of the ZBP is not a modification of the change of $k_B T_K/\Delta$.

One might think the low-field suppression of the ZBP is a result of the magnetic field induced QPT, i.e., the Josephson quantum dot changes from a "0"-junction at zero magnetic field to a "π"-junction at a finite magnetic field, just like the measurements shown in Fig. 4.20 (e) and the data reported in Ref. (80). However, in Fig. 4.32, we will demonstrate that the low-field suppression of ZBP could occur in both "0"-junction and "π"-junction.

Figures 4.32 (a-c) display the magnetic field dependence measurements for the Kondo valley shown in Fig. 4.23 (b). The Josephson quantum dot is a "0"-junction in the center of the odd-occupied Coulomb diamond, due to the strong Kondo effect. It shows a low-field suppression of ZBP in the range of $B = -3 - 3$ mT. We then change to another Kondo valley with a lower T_K of ~ 1.2 K. The bracket-like shape of the ABS-induced conductance peaks in Fig. 4.32 (d) indicate that the Josephson quantum dot is a "π"-junction deep in the odd-occupied diamond region. Figures 4.32 (e) and (f) show the magnetic field dependence measurement for the ZBP, at position A (near the phase transition point) and position B (deep in the "π"-junction), respectively. It is clear to see that a low-field suppression of ZBP occurs at both positions. In this case, there is no QPT because the dot is a "π"-junction even at $B = 0$ mT. Therefore, the low-field suppression of ZBP does not result from the field-induced QPT. Moreover, the zero-bias conductance as a function of B at different V_{bg} positions from A to B are shown in Fig. 4.32. With different bound state energies E_b, the widths of these low-field conductance dips in a magnetic field are all about 6 mT.

In Fig. 4.33, we summarize several measurement results of the low-field suppression of ZBP in the regimes with different T_Ks. Figure4.33 shows the zero-bias conductance as a function of the applied magnetic field, measured at different regimes with different Kondo temperatures. Figures 4.33 (a-d) are measured for Dev. *AlInSbAl#2* and (e-h) are measured for Dev. *AlInSbAl#3*. The low-field suppression of the zero-bias conductance occurs in all of the regimes, with the T_K
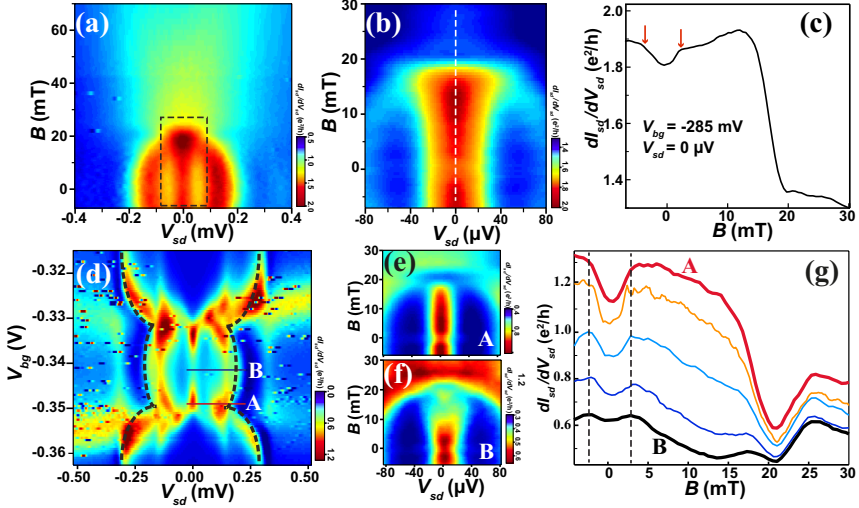
Figure 4.32: The low-field suppression of the ZBPs in a "0"-junction and in a "π"-junction. (a) The differential conductance on a color scale as a function of V_{sd} and B, measured for Dev. *AlInSbAl#3* at the center of the odd-occupied Coulomb diamond in Fig. 4.23 (b). (b) A close-up view of the squared region in (a). (c) The zero-bias conductance as a function of the magnetic field [along the dashed line in (b)]. The ZBP in this "0"-junction Kondo valley shows a fainter conductance-dip as indicated by the arrows in (c). (d) The low-energy charge stability diagram with the SGS, measured for Dev. *AlInSbAl#3*, at $V_{g1} = -2$ V and $V_{g2} = 3$ V. The bracket-like shape of the ABS signature indicates that the quantum dot is a "π"-junction in the odd-occupied diamond. (e)-(f) The same as (b), but measured at the positions A and B in (d). (g) The zero-bias conductance as a function of B measured at different V_{bg} between positions A and B. It is clear to see that a low-field conductance dip emerges in each of these curves. The width of the dip on the scale of the magnetic field does not depend on the energy E_b of the sub-gap bound states.
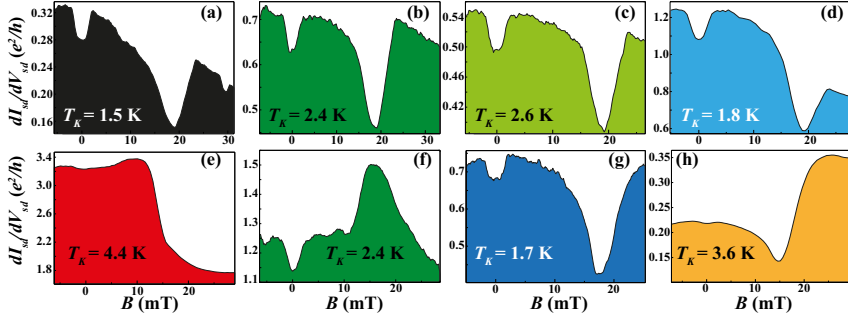
Figure 4.33: The zero-bias conductance as a function of the applied magnetic field, measured at different regimes with different Kondo temperatures. (a-d) are the measurements for Dev. *AlInSbAl#2* and (e-h) are the measurements for Dev. *AlInSbAl#3*. The low-field suppression of the zero-bias conductance occurs in all of the regimes, with the T_K ranging from 1.5 K to 4.4 K. However, the suppression is very weak in the regimes shown in (e) and (h) associated with the highest T_K of 4.4 K and 3.6 K, respectively.

ranging from 1.5 K to 4.4 K. However, the suppression is very weak in the regimes shown in (e) and (h) which have the highest T_K of 4.4 K and 3.6 K, respectively.

We also performed field dependence measurements for Dev. *AlInSbAl#3* in an open region without the Coulomb blockade.

Figure 4.34 (a) shows the differential conductance as a function of V_{sd} and V_{bg}, measured in the open region of Dev. *AlInSbAl#3* in its normal state at $B = 30$ mT. Because there is no Coulomb blockade, the conductance exceeds $2e^2/h$. A chess-pattern conductance structure can be identified, indicating that the Fabry-Pérot interference-like transport occurs. In the superconducting state, the tunneling of the Cooper pair is enhanced at the constructively interfered points in the conductance chess pattern and a high ZBP emerges there (111) [Fig. 4.34 (b)]. The magnetic field dependence measurements are shown in Figs. 4.34 (c) and (d), at $V_{bg} = 1.88$ V as indicated by the dashed line in Fig. 4.34 (b). Although the supercurrent-induced ZBP is as high as $6e^2/h$, no low-field suppression emerges here.

Consequently, the low-field suppression is much sharper for the ZBP in the Kondo regime with a medium T_K. Also, for the same device, the conductance-dip width in the scale of the magnetic field varies very little with gate voltage, despite the fact that the g-factor of the quantum dot and T_K both fluctuate greatly with
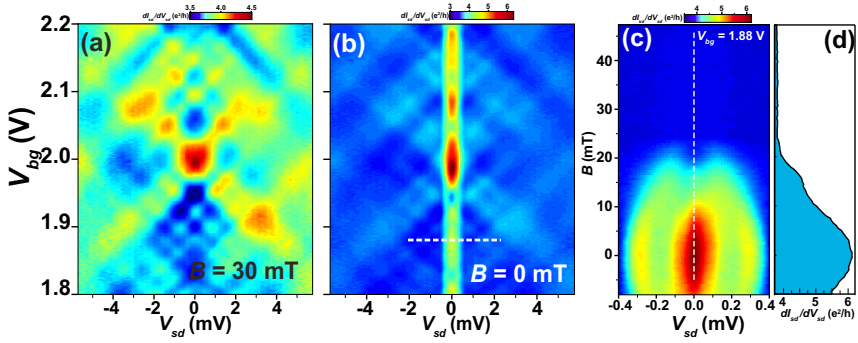
Figure 4.34: The measurements in the open region of Dev. *AlInSbAl#3*. (a) The charge stability diagram measured in the open region of Dev. *AlInSbAl#3* in its normal state at $B = 30$ mT. A Fabry-Pérot interference-like conductance chess pattern can be identified. (b) The same as (a), but measured in the superconducting state at $B = 0$ mT. The Josephson current induced ZBP is visible at those V_{bg} values where the normal state conductance is high. (c) The differential conductance as a function of V_{sd} and B, measured at the position indicated by the dashed line in (b). (d) The zero-bias conductance as a function of B [along the dashed line in (c)]. The ZBP does not show any suppression in the low-field region.

gate voltage. However, the dip-width can be very different from device to device.

We are uncertain about the physical origin of the exotic low-field suppression of the ZBP. Similar field-enhancement of the superconductivity has been reported in ultra-thin superconductor films and wires (112, 113, 114), where it is referred to as the *anti-proximity effect*. Different explanations are proposed for the anti-proximity effect in those references. However, the anti-proximity effect in Josephson quantum dot has never been reported. Our measurements show that the anti-proximity effect is routinely found in the Kondo regime of the InSb nanowire based Josephson quantum dot devices. The anti-proximity effect likely favors the regime where the Kondo effect promotes the co-tunneling of Cooper pair but the quantum dot remains to be spinful.

5

Search for Majorana Bound States in Superconductor-InSb Nanowires Hybrid Devices

In this chapter, we will discuss the search for the Majorana bound states in superconductor-InSb nanowire hybrid systems. Anomalous zero-bias differential conductance peaks, as the signatures of the Majorana bound states, are studied in Au-InSb nanowire quantum dot-Nb hybrid device and in Nb-InSb nanowire quantum dot-Nb hybrid devices. The zero-bias conductance peaks that induced by other mechanisms are also described in comparison with the signature of Majorana bound states.

5.1   Majorana bound states in superconductor-coupled semiconductor nanowires

Majorana fermions are particles with half spins and they are their own antiparticles. The exotic fermions are first predicted by and then named after Ettore Majorana. The conception arises from a "real" version of Dirac equation. Dirac derived his relativity-style Schrödinger equation in 1928, from which Dirac developed the conception of negative energy and thereby predicted the existence of antiparticles. A few years later, antiparticles were discovered. In the terms of quantum field theory, a particle and its anti-particle can be described by a pair of conjugate complex fields. However, an imaginary part is included in Dirac equa-

tion, and therefore the quantum state of the particle is complex. As we know, a complex number is different from its conjugation and hence a particle is different from its antiparticle, for example, electron is distinct from its antiparticle– positron. In 1937, Ettore Majorana fashioned Dirac formula by making it more mathematically elegant (115). He replaced Dirac's matrices with a pure imaginary one and thus could get a real wave function eventually. Since for a real wave function Ψ, $\Psi = \Psi^{\dagger}$ holds, and an interesting deduction thereby comes out from Majorana equation: there could be some $-\frac{1}{2}$-spin fermions which are their own antiparticles.

The first candidate of Majorana fermions was (and is) the neutrino. One way to check whether the neutrino is or is not a Majorana fermion is the so-called neutrinoless $\beta\beta$-decay neutron collisions (116, 117). However, although plenty of efforts have been made over several decades, no neutrinoless $\beta\beta$-decay is observed. Another Majorana fermions hunting field is fairly larger than the size of an atom, the cosmos. To explain the conflicts between cosmology observations and calculations (118), it is suggested that our visible universe, i.e., the part composed of the Standard Model (SM) particles (119), is actuarially immersed in a giant bath of the *dark matters*. The most popular theory about the composition of the dark matters is the hypothesis of the weakly interacting massive particles (WIMP) (120). It is soon realized that the hypothetical WIMP particle could be a candidate of the Majorana neutrinos (121).

Along with the efforts made in particle physics and cosmology, a new Majorana fermions searching field is also opened up in solid state physics. It was realized that the quasi-particles in solid state systems could be engineered to materialize the Majorana fermions (122, 123, 124, 125, 126). Numerous proposals for probing Majorana fermions in solid state systems[1] have been suggested, ranging from the fraction quantum Hall effect with 5/2 filling factor (128), the p-wave superconductor (129), the topological insulator coupled to an s-wave superconductor (130), and the semiconductor with strong spin-orbit interaction (SOI) in the close proximity of an s-wave superconductor (131, 132). One of the most recent proposals is to expose a superconductor-coupled semiconductor nanowire with a strong SOI into an external magnetic field (133, 134). These proposals have stimulated a new wave of searches for Majorana fermions in solid state

---

[1]The ultra-cold ^{3}He superfluid droplet (127) is also a candidate platform for realizing Majorana bound states.

systems. The Majorana fermions in solid state systems, are also referred to as the Majorana bound states, obey a so-called non-Abelian statistics (135, 136). This makes the Majorana bound states a promising candidate of the topological quantum computer (8, 9, 137), which is robust against local noise.

The key idea of materializing the Majorana bound states in superconductor-semiconductor nanowire hybrid devices is to create a p-wave superconducting environment. Differing from the s-save superconductivity that we have discussed in previous chapters, the p-wave superconductivity is implemented by pairing the electrons with the same spins to a Cooper-pair (spin-triplet pairing). To realize p-wave superconductivity in semiconductors, two conditions have to be met: a spin-less environment near the Fermi-level and an induced superconducting energy gap in the close proximity of an s-wave superconductor.

Normally, the energy dispersion of 1D semiconductor nanowire is parabolic, with a spin degeneracy [Fig. 5.1 (a)]. However, in the presence of an SOI, the two electronic spin bands split as shown in Fig. 5.1 (b). Under an application of an external magnetic field normal to the SOI induced effective magnetic field, a gap E_z is opened up by the Zeeman splitting at $k = 0$ in the dispersion relation [Fig. 5.1 (c)]. Here, the spins at $k = \pm k_F$ are polarized by the SOI and the external magnetic field. The nanowire with a dispersion relation as shown in Fig. 5.1 (c) is usually called in a helical phase. A spin-less environment is thereby formed at the Fermi level in the helical phase. Superconducting energy gap can be also induced into the nanowire by the proximity effect, and a superconducting energy gap Δ is opened at the Fermi level. This is the superconducting phase [Fig. 5.1 (d)]. When both Zeeman gap and superconducting gap are induced, the nanowire can be driven into two different phases, depending on the relation of the Zeeman gap E_z and the superconducting energy Δ. If $E_z < \Delta$ [Figs. 5.1 (e) and (g)], the nanowire is in the trivial superconducting phase because electrons with opposite spins are involved in electron pairing. However, if $E_z > \Delta$ [Figs. 5.1 (f) and (h)], only one spin can be used to form Cooper pairs, i.e., the p-wave pairing occurs. In this case, the nanowire is called in the non-trivial superconducting phase or the so-called topological superconducting phase. According to Kitaev (8), a pair of Majorana bound states will be created at the two ends of a 1D p-wave superconducting chain.
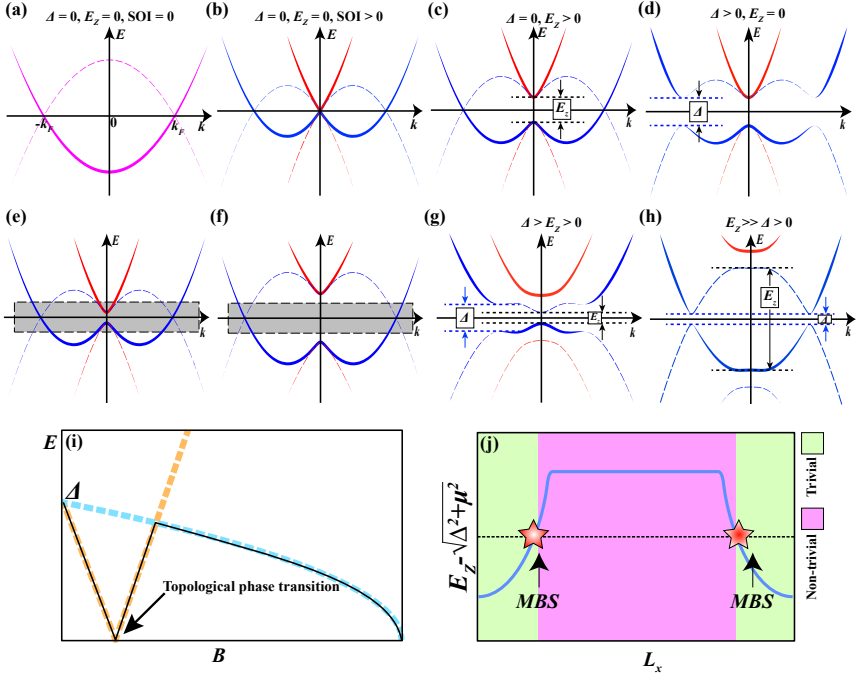
Figure 5.1: Energy dispersion of 1D semiconductor nanowires. Solid lines represent the electron-like bands, while the dashed lines represent the hole-like bands. (a) The nanowire energy dispersion of the normal phase without any SOI. The two electron spin bands are degenerate. (b) Spin bands split due to the SOI. (c) The helical phase. A Zeeman energy gap E_z opens up under the application of an external magnetic field normal to the direction of the SOI. (d) The superconducting phase. A superconducting energy gap Δ is induced into the nanowire. No magnetic field is applied here. (e-f) Two helical phases with different E_z values. The gray regions represent the superconducting energy gaps that would be induced after the nanowire being coupled to an s-wave superconductors. A spineless environment is formed in the gray region of the helical phase dispersion in (f). (g) The trivial superconducting phase with $\Delta > E_z$. (h) The non-trivial superconducting phase with $\Delta < E_z$. (i) The field evolution of $E(k_F)$ (the light-blue line) and $E(0)$ (the brown line). The black line shows the field evolution of the overall energy gap. (j) Two Majorana bound states (indicated by the ★) are formed at the two boundaries of the trivial superconducting phase and the non-trivial superconducting phase. Panels (a-h) are reproduced by courtesy of Guang-yao Huang.

5.2 Anomalous zero-bias conductance peaks in superconductor coupled InSb nanowire quantum devices

Semiconductor InSb nanowires, with strong Rashba SOIs (138, 139, 140), giant effective g-factors (20) and good couplings to s-wave superconductors (66), are expected to provide an excellent material platform for the study of Majorana bound state in solid state systems (51, 98, 141, 142, 143). In this section, we will introduce the measured zero-bias differential conductance peaks as the signatures of the Majorana bound states in the InSb nanowire-based hybrid devices.

Devices with two different geometries are fabricated and measured, as shown in Fig. 5.2. The first geometry is a normal metal-InSb nanowire-superconductor structure [Fig. 5.2 (a)], with a quantum dot in between the normal metal and the superconductor. This structure is referred to as the N-QD-S structure. With an external magnetic field of moderate strength, the InSb nanowire segment that is covered by the superconductor can be driven into a topological superconducting phase. As we discussed earlier, a pair of Majorana bound states will be formed at the ends of the topological superconductor nanowire segment. The wave function probability distributions in non-trivial superconducting phase, along the nanowire segment that is covered by the superconductor in Fig. 5.2 (a) is shown in Fig. 5.2 (c). We can see that a pair of zero-energy bound states emerge in the superconducting energy gap, at the ends of the topological superconducting nanowire segment. The second geometry is a superconductor-InSb nanowire-superconductor structure [Fig. 5.2 (b)], again, with a quantum dot formed in between the two contacts. This structure is referred to as the S-QD-S structure. Since there are two InSb nanowire segments are covered by superconductors, two pairs of Majorana bound states can be held in the nanowire in a moderate magnetic field, separated by the quantum dot. However, the two inner Majorana bound states (near the quantum dot) can hybridize into a pair of quasi-particles with finite energies, if the coupling between them is strong. The wave function probability distributions in non-trivial superconducting phase, along the nanowire in Fig. 5.2 (b) is shown in Fig. 5.2 (d). We can see that there are two pairs of low-energy bound states emerging in the superconducting energy gap. The two outer bound states are zero-energy states, while the two inner bound states have non-zero energies due to the wave function hybridization.

To drive the Nb-contacted InSb nanowire segments of the device from a triv-
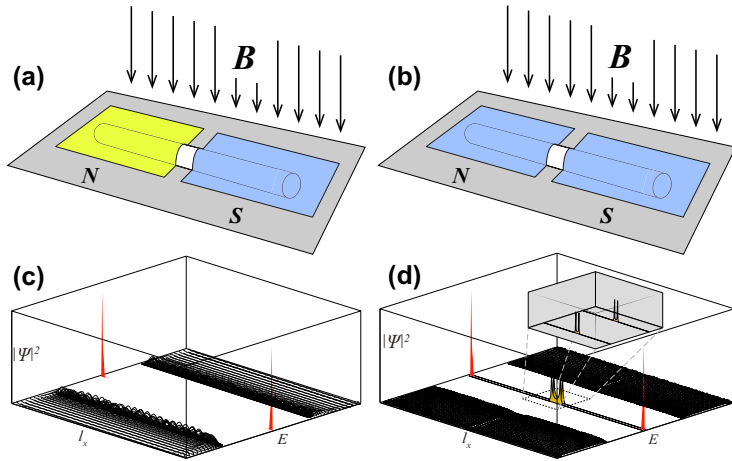
Figure 5.2: Two devices for creating and detecting Majorana bound states. (a) The schematic layout of the normal metal-InSb nanowire-superconductor hybrid device. (b) The schematic of the superconductor-InSb nanowire-superconductor hybrid device. (c) Wave function probability distributions in a non-trivial superconducting phase, along the nanowire segment that is covered by the superconductor in (a). (d) Wave function probability distributions in a non-trivial superconducting phase along the nanowire in (b). Panels (c) and (d) are reproduced by courtesy of Guang-yao Huang.

ial superconducting phase to a nontrivial topological superconducting phase, an application of an external magnetic field B, perpendicular to the Rashba SOI-induced effective magnetic field B_{SO}, is needed. The magnetic field introduces a Zeeman energy $E_z = \frac{1}{2}|g^*|\mu_B\tilde{B}$, where $\mu_B = e\hbar/2m_e$ is the Bohr magneton, g^* is the effective g-factor, and $\tilde{B}$ is the magnetic field actually applied on the Nb-contacted InSb nanowire segments, which is greatly different from B due to the Meissner effect. The topological phase transition occurs at $E_z = \sqrt{\Delta_{InSb}^2 + \mu^2}$ (131, 133, 134). In general, it is difficult to accurately determine the strength of the externally applied magnetic field B_T at which the phase transition in the Nb-contacted InSb nanowire segments occurs. In a single band transport case, according to the measured properties of the Nb trilayer thin film measured in Chapt. 4, the value of B_T (at $\mu = 0$) is estimated to be in the range of $0.33 - 0.78$ T.

5.2.1   Anomalous ZBP in Au-InSb nanowire-Nb quantum devices

In this subsection, we discuss the anomalous zero-bias conductance peak (ZBP) arising from an N-QD-S device in finite magnetic fields. An SEM image of the fabricated and measured N-QD-S device, Dev. *AuInSbNb*, is shown in Fig. 5.3(a). The device was made from the InSb nanowire segment of an InAs/InSb heterostructure nanowire. One of its two contacts was made from superconducting Nb (in a 3 nm Ti/80 nm Nb/5 nm Ti triple layer form) and the other one was made from normal Au (in a 4 nm Ti/80 nm Au double layer form). The spacing between the two contacts is about 210 nm. Mourik et al. and Churchill et al. have studied devices with similar geometries as Dev. *AuInSbNb* (98, 143). Differing from those devices, an InSb nanowire quantum dot was formed in the junction between the two contacts in this device.

Figure 5.3(b) shows the differential conductance of the device measured at $B = 0$ T as a function of V_{bg} and V_{sd}. Coulomb diamond structures can be identified in the diagram with the addition energy E_{add} is about $1.5 - 2$ meV. At small source-drain bias voltages, we see the existence of a gap of low conductance over the entire measured back gate voltages in the figure. This low conductance gap arises from the proximity effect induced superconducting energy gap of the InSb nanowire. Figure 5.3(c) shows a trace taken from Fig. 5.3(b) at $V_{bg} = 0.835$ V. The low conductance gap in the low bias voltage region can be easily identified. At the edges of the gap, two conductance peaks appear located symmetrically around
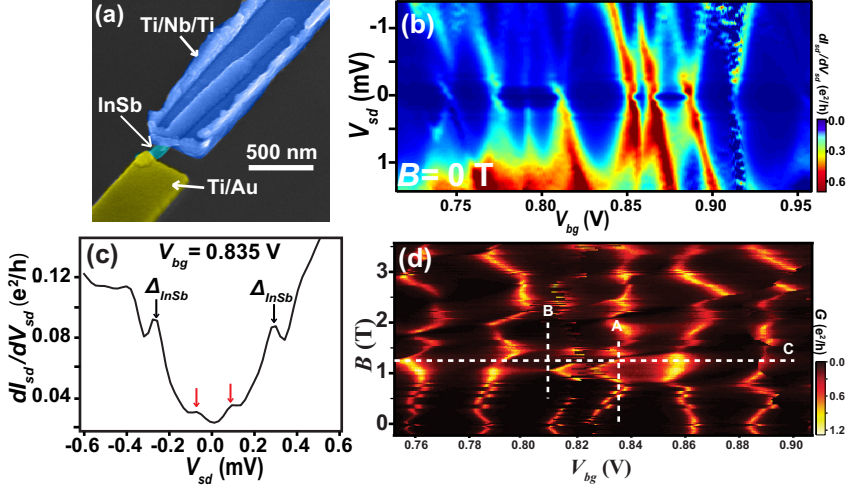
Figure 5.3: N-QD-S device. (a) SEM image of the fabricated Au-InSb nanowire quantum dot-Nb device, Dev. *AuInSbNb*. (b) Differential conductance on a color scale as a function of V_{bg} and V_{sd} (charge stability diagram) measured at $B = 0$ T. Here, no ZBP is visible. (c) A differential conductance trace of the device at $V_{bg} = 0.835$ V. The two conductance peaks indicated by the two black arrows can be attributed to the quasi-particle tunneling through the singularities in the DOS of the superconducting InSb nanowire. The two conductance peaks indicated by red arrows are most likely caused by the Andreev bound states in the junction region. (d) Linear conductance on a color scale measured for the device as a function of V_{bg} and B.

$V_{sd} = 0$ V. These peaks arise from quasi-particle tunneling through the singularity points in the DOS in the superconductor InSb nanowire and the distance between the two peaks is given by $2\Delta_{InSb}/e$, where Δ_{InSb} is the proximity effect induced superconducting energy gap in the InSb nanowire. From the measurements, we can deduce a value of $\Delta_{InSb} \sim 0.27$ meV. We also note that the measurements also show two weak subgap differential conductance peaks as indicated by red arrows in Fig. 5.3(c). These two subgap peaks are most likely due to Andreev bound states located symmetrically around zero energy in the dot, as we described in the previous chapter. Figure 5.3(d) shows the linear conductance on a color scale measured for the device as a function of V_{bg} and B. The field-evolution of the quantum levels can be seen.

No ZBP can be seen in Fig. 5.3(b). However, ZBP emerges in the charge stability diagram shown in Fig. 5.4(a), which is measured at the same gate voltage region as in Fig. 5.3(b) but at $B = 1.25$ T [along the dashed-line C in Fig. 5.3 (d)]. A weak ZBP is visible in the whole gate voltage range. For a better visualization of the ZBP, Figs. 5.4(b) to 5.4(d) show three traces of the differential conductance measured at back gate voltages $V_{bg} = 0.9$, 0.84 and 0.78 V, i.e., along the three dashed lines in Fig. 5.4(a). A ZBP is clearly seen in each of the three traces regardless of differences in the back ground conductance. Several 3D colormap charge stability diagrams for different V_{bg} regions are also illustrated in Figs .5.4(e)-(h). A continuous zero-bias peak can be seen in each of these 3D plots, no matter the quantum dot is in on/off-resonance status.

Figure 5.5(a) shows the differential conductance measured for the device at a fixed back gate voltage $V_{bg} = 0.835$ V [along the dashed-line A in Fig. 5.3 (d)] as a function of V_{sd} and B. In these measurements, no ZBP features are found at magnetic fields $B < 0.8$ T. However, at $B \sim 0.8$ T, two weak conductance peaks appear in the close vicinity of $V_{sd} = 0$ V. As the magnetic field iincreases further, the two conductance peaks gradually merge into a single ZBP at $B \sim 1.2$ T. The ZBP remains visible until $B \sim 1.5$ T. Figure 5.5(b) shows the same measurements of differential conductance as a function of V_{sd} and B but for the device at $V_{bg} = 0.81$ V [along the dashed-line B in Fig. 5.3 (d)]. In this figure, a few line-cuts of the differential conductance taken at different V_{bg}, as indicated by horizontal solid lines are shown. Here, again, we see no ZBP at low magnetic fields, but it is clearly visible at magnetic fields $B \sim 0.9 - 1.8$ T.

Consequently, the ZBP only emerges in a finite magnetic field $B > 0.8$ T
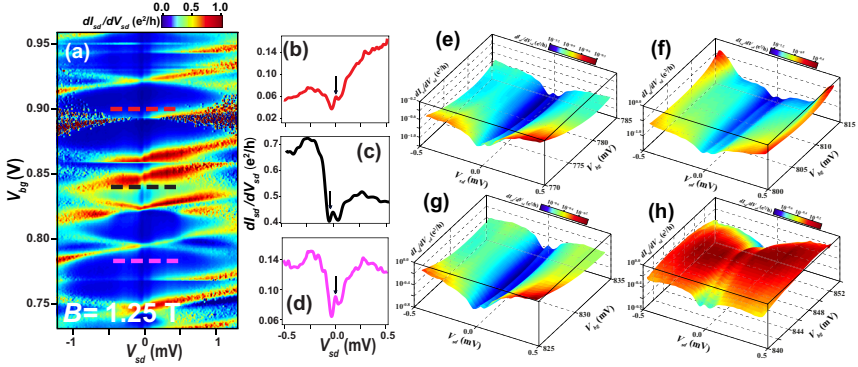
Figure 5.4: N-NW-S2. (a) Differential conductance on a color scale as a function of V_{bg} and V_{sd} measured at $B = 1.25$ T for Dev. *AuInSbNb*. A weak ZBP is visible over the measured V_{bg} region in the figure. (b)-(d) Traces of the differential conductance of the device taken from (a), at three different values of V_{bg} indicated by the dashed lines in (a). A ZBP is clearly seen in each trace. (e)-(g) 3D colormaps of charge stability diagrams for different V_{bg} regions, where a continuous ZBP goes through all the diagrams.

and it is not dependent on the on/off-resonance status of the quantum dot. It cannot be attributed to the Kondo effect as discussed in Chapt.3, or the field-induced QPT as discussed in Chapt.4 either. Similar as in Ref. (98), the ZBP here is a signature of the Majorana bound states in the InSb nanowire segment covered by the superconductor Nb contact. However, differing from Ref. (98), the zero-energy state is probed by the Au contact via the quantum dot (144).

5.2.2 Zero-bias conductance peaks in Nb-InSb nanowire-Nb quantum devices

Besides in the N-QD-S structure device, we also observed anomalous ZBPs in S-QD-S structure devices.

Figure 5.6 (a) displays the charge stability diagram of Dev. *NbInSbNb#2* measured at a magnetic field of $B = 0$ T. Here, a clear quasi-particle Coulomb blockade diamond structure is seen, indicating the formation of a quasi-particle quantum dot in the InSb nanowire junction region between the two superconductor contacts. From the Coulomb diamond structure, we can determine that the quasi-particle addition energy of the quantum dot is $E_{add} \sim 7$ meV, which is much larger than the superconducting energy gap Δ_{Nb} of Nb. Inside the Coulomb
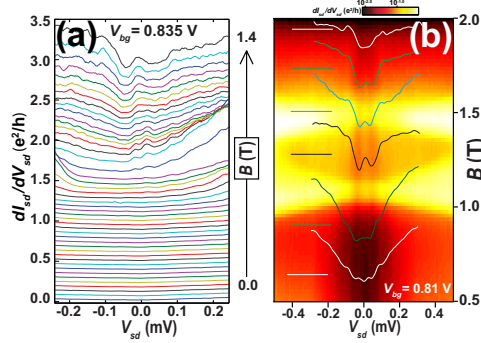
Figure 5.5: (a) Differential conductance as a function of V_{sd}, at $V_{bg} = 0.835$ V and at different B in the region of $B \sim 0 - 1.4$ T, measured for Dev. *AuInSbNb*. The measured curves are successively offset by $0.06 e^2/h$ for clarity. A ZBP is present at magnetic fields $B \sim 1.2 - 1.5$ T. (b) The same measurements as in (a) but for $V_{bg} = 0.81$ V. Superimposed on the Fig. are the traces of the differential conductance taken at different B values indicated by horizontal lines in the figure. A ZBP is clearly seen in the magnetic field region between $B \sim 0.9 - 1.8$ T.

blockade region, vertical stripe features of high conductance can be identified. These high conductance stripe features are due to the MARs associated with the superconducting energy gap Δ_{Nb} of Nb and the MARs associated with the induced superconducting energy gap Δ_{InSb} of InSb nanowire.

The magnetic field dependent measurements of the differential conductance for Dev. *NbInSbNb#2* at $V_{bg} = -11.1$ V, for which the device is in a quasi-particle Coulomb blockade region. Figure 5.6 (b) shows the results of the measurements on a color scale and Fig. 5.6 (c) shows the ranctangled region in Fig. 5.6 (b) in a line-cuts plot. The main observation is the emergence of a pronounced high ZBP structure as the magnetic field exceeds ~ 1 T. The ZBP lasts to $B \sim 2.5$ T and locates symmetrically with respect to zero magnetic field. A similar ZBP also emerges in the magnetic field dependent measurements for the same device at $V_{bg} = -15$ V, as shown in Fig. 5.6 (d). Figure 5.6 (e) shows the high-resolution measurements of the charge stability diagram in the center of the quasi-particle Coulomb blockade region at $B = 1.8$ T for which the measurements show a strong ZBP. It can be seen clearly that the ZBP runs through the whole blockade region. Figure 5.6 (f) shows the temperature dependence measurements of the ZBP. The differential conductance are measured at $B = 1.8$ T and $V_{bg} = -11.1$
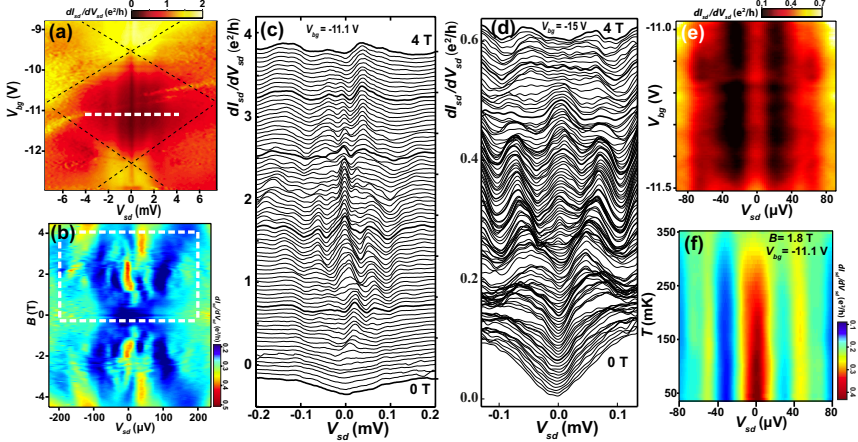
Figure 5.6: Anomalous ZBP in Dev. *NbInSbNb#2*. (a) The charge stability diagram measured for Dev. *NbInSbNb#2* at $B = 0$ T. The measurements show a quasi-particle Coulomb blockade diamond structure with a quasi-particle addition energy $E_{add} \sim 7$ meV to the InSb nanowire quantum dot. The weak vertical stripes of high conductance seen in the Coulomb blockade region arise from MARs with the superconducting energy gaps, Δ_{Nb} and Δ_{InSb}, related, respectively, to the two Nb-based contacts and the two proximity-effect-induced superconducting InSb nanowire segments covered by the Nb based contacts. (b) Differential conductance on a color scale as a function of source-drain bias voltage V_{sd} and magnetic field B applied perpendicularly to the substrate and to the InSb nanowire measured for the Dev. *NbInSbNb#2* at $V_{bg} = -11.1$ V [corresponding to the dashed line in (a)]. A pronounced zero bias conductance peak is seen to emerge when the magnetic field exceeds ~ 1 T, in both the positive and the negative magnetic field directions. (c) Same measurements as in (b), but the differential conductance traces measured in the region marked by the dashed square in part (b) are shown. Here, the measured curves are successively offset by 0.05 e^2/h for clarity. In this figure, in addition to the ZBP, two side differential conductance peaks are seen to appear at finite V_{sd}. (d) The same with (c) but measured for the device at $V_{bg} = -15$ V. (e) High-resolution measurements of the charge stability diagram for the device at $B = 1.8$ T, for which the device shows a strong ZBP. Here, only the measurements in the center of the Coulomb blockade region are shown. (f) Differential conductance on a color scale as a function of V_{sd} and temperature T measured for the device at $B = 1.8$ T and $V_{bg} = -11.1$ V. Here, it is seen that the ZBP becomes hardly visible when the temperature goes above 350 mK.

V, as a function of V_{sd} and temperature T. Here, we find that the ZBP decreases gradually as the temperature is increased and becomes to be hardly visible at a temperature $T \sim 350$ mK (which corresponds to an energy scale of 32 μeV) and above.

Now we check what the possible mechanism(s) of the ZBP is here. In a Josephson junction device, there are several mechanisms that can cause a ZBP, such as the Kondo effect, YSR/ABS bound states at QPT point, the Josephson current, and the high-order MARs. For the Kondo effect, irrespective of half or integer spin Kondo effect, an associated ZBP should split and move to finite bias voltage positions with an increasing magnetic field. However, in our measurements, the ZBP appears at much stronger magnetic fields (about 1.2-2.7 T) and it does not show splitting over about a 1.5 T range of magnetic fields. Therefore, the ZBP we have observed in here could not be a feature of the Kondo effect. As we discussed in Chapt. 4, field induced QPT can also lead to a ZBP. However, the QPT induced ZBP will split as the magnetic further increases. The Josephson current and high-order MARs can also give a ZBP. In both cases, the ZBP will decrease with an increasing magnetic field. This is clearly not consistent with our observations, and therefore, all these superconductivity effects cannot be considered as the physical origin of the ZBP that we have observed. One may also argue that an applied perpendicular magnetic field could change the energy level positions in the InSb nanowire quantum dot, leading to level shifting, due to, e.g., the Zeeman effect and thus occasionally turn the device to resonant conduction even if the device is in a Coulomb blockade region at $B = 0$ T (i.e., the B-FET effect, as we mentioned in Chapt. 4). However, in Fig. 5.6 (e), we see that the ZBP runs through the whole blockade diamond, even with the quantum dot is in the off-resonance status. It should also be noted that in a recent theoretical work (145), it was predicted that weak antilocalization could induce a ZBP in a disordered Majorana nanowire. However, due to the inclusion of a quantum dot in our Nb-InSb nanowire-Nb device, the weak antilocalization induced ZBP should be suppressed by the Coulomb blockade effect.

In the point of view of Majorana bound states, when there is no coupling between the two Nb-covered InSb nanowire segments in the device, each of the two nanowire segments in a topological superconductor phase should support a pair of Majorana fermions located at the two ends of the segment. When the two topological superconducting InSb nanowire segments are coherently connected

via a quasi-particle quantum object, e.g., quantum dot, the interaction between a pair of nearby zero-energy Majorana fermions leads to the creation of a pair of normal fermion states at finite energies. The entire nanowire will then behave as a topological superconductor, supporting the pair of the remaining zero-energy Majorana modes [see Fig. 5.2 (d)], which are located at the two ends of the entire nanowire and are therefore strongly coupled to the Nb contacts. Cooper pairs can move between the two Nb contacts via the Majorana bound states, leading to an enhancement in the zero-bias conductance. Therefore, the ZBP observed in this device could be a signature of Majorana bound states.

A more interesting question is how the even-odd parity of the the intermedia quantum dot influence the ZBP emerging in a finite magnetic field. In Figs. 5.7 and 5.8, we investigate the evolution of the ZBP with the change of the even-odd parity of the quantum dot.

Figure 5.7 displays the charge stability diagram of Dev. *NbInSbNb#1* at $B = 0$ T, with the differential conductance in a logarithmic color scale. Here, clear Coulomb blockade diamond structures can be seen, indicating the formation of the QD between the two superconductor contacts. The quasi-particle addition energy E_{add} to the QD at $B = 0$ T is in the range of $2.7 - 5.6$ meV, which is much larger than Δ^*. E_{add} also shows a regular odd-even oscillations behavior which indicates the alternation in the odd-even parity of the quasi-particle occupation number in the QD. No ZBP features can be identified in the diagram. Figure 5.7 (b) shows the charge stability diagram measured for the device at $B = 1.2$ T. Figures 5.7 (c) and 5.7 (d) are the corresponding line-cut plots of the differential conductance on the linear scale at small source-drain bias voltages. For clarity, these line-cut plots are presented in such a way that their differential conductance values at $V_{sd} = 0$ μV are successively offset by 0.005 e^2/h in each figure, while their actual zero-bias conductance values are represented by their colors in a gray scale. Here, Coulomb diamond structures remains to be clearly seen in the charge stability diagram plot of Fig. 5.7 (b), indicating the survival of the QD in the device in the presence of a 1.2 T magnetic field. In the line-cut plots of Fig. 5.7 (c) and 5.7 (d), we can see a global conductance gap structure in the small source-drain bias voltage region of $V_{sd} \sim -0.35$ meV to $V_{sd} \sim 0.35$ meV, showing that the Nb-contacted InSb nanowire segments are still in a superconducting state with an energy gap $\Delta_{InSb} \sim 0.17$ meV. Strikingly, a pronounced conductance peak appears at zero-bias voltage and goes through almost the whole V_{bg} region
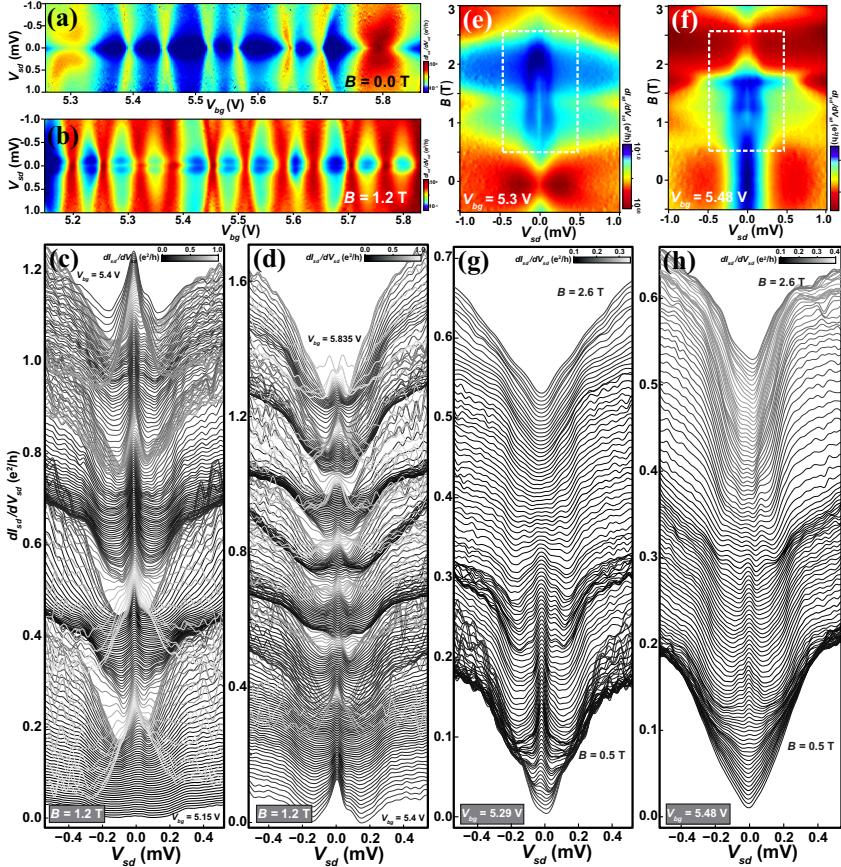
Figure 5.7: ZBP in Dev. *NbInSbNb#1*. (a) The charge stability diagram measured for
Dev. *NbInSbNb#1* at $B = 0$ T. (b) The same with (a) but measured at $B = 1.2$ T. (c)
and (d) show the differential conductance line-cut plot at low-bias voltage as a function of
V_{bg}, corresponding to the conductance color map in (b). V_{bg} ranges from 5.15 V to 5.4 V
in panel (c), and 5.4 V to 5.835 V in panel (d). For clarity, these line-cuts are shifted in
such a way that the differential conductance at $V_{sd} = 0\mu$V are linearly offset by $0.005e^2/h$,
while their real zero-bias conductance values are represented by their color in a gray scale.
A ZBP almost going through the whole stability diagram is clearly visible in panels (b-d)
and (d). The ZBP appears in each of the CB diamond structures, irrespective of the QD
occupation number is even or odd. (e) and (f): The differential conductance measured for
the device as a function of V_{sd} and B, at $V_{bg} = 5.29$ V and $V_{bg} = 5.48$ V, respectively.
(g) and (h): Differential conductance line-cut plots at low bias voltage as a function of B,
corresponding to the rectangled regions in panels (e) and (f). For clarity, these line-cuts are
shifted in the same way as in (c) and (d). In the panels (d-g), ZBPs emerge at $B = 0.5 - 0.6$
T and last more than 1 T before their disappearing.

133

shown here, including both the Coulomb blockade regions and quantum resonance regions. This zero-bias conductance peak feature is seen in Fig. 5.7 (b), and is even more remarkably seen in Figs. 5.7 (c) and 5.7 (d). The zero-bias conductance peak has a height up to $\sim 0.2\ e^2/h$ at the quantum resonance points and $\sim 0.06\ e^2/h$ at the electron-hole symmetry points (centers of the Coulomb blockade regions). Moreover, appearance of the zero-bias conductance peak is independent of the even-odd parity of the quasi-particle number in the QD, i.e., the ZBP appears in all the Coulomb blockade regions, irrespective of even or odd the quasi-particle occupation number in the QD is.

Figures 5.7 (e-h) shows the magnetic field dependent measurements of the differential conductance for the device. Figures 5.7 (e) and 5.7 (f) display the differential conductance in a logarithmic color scale measured for the device as a function of V_{sd} and magnetic field B perpendicularly applied to the substrate at $V_{bg} = 5.29$ V and $V_{bg} = 5.48$ V. The corresponding line-cut plots of the differential conductance in the linear scale are shown in Figs. 5.7 (g) and 5.7 (h). For clarity, these line-cut curves are offset in the same way as in Figs. 5.7(c) and 5.7 (d), with their actual zero-bias conductance values represented again in a gray scale color. The B-evolution measurements of the differential conductance in Figs. 5.7 (e) and 5.7 (g) starts from the CB region of an odd-occupied diamond at $B = 0$ T, while it starts from an even-occupied CB region at $B = 0$ T for Figs. 5.7 (f) and 5.7 (h). Again, from these figures, we can see Δ_{InSb}-induced low-conductance gap, and it shows a tendency of gradually decreasing as B increases. Within both odd and even occupied CB regions, there are no ZBP structures when the applied magnetic field is small. However, as the magnetic field increases over a certain value, ZBP structures emerge in both odd and even occupied CB regions. The ZBP structures insist for a long range of magnetic field before they finally disappearing at high magnetic field region. The ZBP in Figs. 5.7 (e) and 5.7 (g) emerges at $B =\sim 0.6$ T and disappears at $B =\sim 1.8$ T, while the ZBP exists in the range of $B = 0.75 - 2.1$ T in Figs. 5.7 (f) and 5.7 (h).

The measurements results represented in Fig. 5.7 are consistent with the measurements in Fig. 5.6. With more Coulomb diamonds, the ZBP feature in this device shows a clear robustness against even-odd parity of quasi-particle numbers in the QD. In the same argument mentioned earlier, the parity-independent ZBP cannot be explained by the Kondo effect, ABS, the Josephson current, the high-order MAR, or the weak anti localization. It could be a signature of Majorana
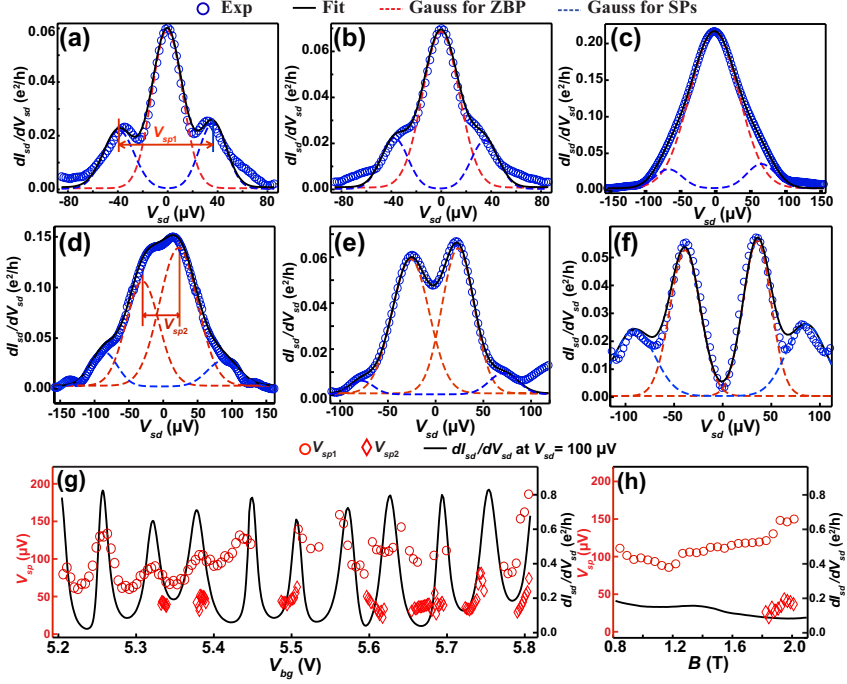
Figure 5.8: (a)-(f) : Differential conductance as a function of V_{sd} at $V_{bg} = 5.385$ V, 5.395 V, 5.445 V, 5.765 V, 5.815 V and 5.835 V, respectively, measured for Dev. *NbInSbNb#1* at $B = 1.2$ T. Experimental data, Gaussian-fitting for ZBPs and Gaussian-fitting for side structures are represented by blue dots curves, red dashed lines, and blue dashed lines, respectively. The summary of ZBP fitting and side structure fitting in each of these panels is represented by black solid line. (g) Side structure separations in bias voltage V_{sp1}, V_{sp2}[see definitions in panel (a) and (d)], and dI_{sd}/dV_{sd} at $V_{sd} = 100$ μV, as a function of V_{bg}. V_{sp2} values are only extracted for the curves whose ZBPs show clear splitting (split into two peaks or a plateau structures). It shows a clear synchronization between V_{sp1} values and the background conductance Coulomb oscillations. (h) The values of V_{sp1} and V_{sp2} as a function of B, extracted from Fig. 5.7(c), together with the differential conductance at $V_{sd} = 100$ μV.

bound states, as we discussed on Dev. *NbInSbNb#2*.

As we discussed previously, coherently coupled Majorana bound states will hybridize into a pair of quasi-particle with finite energies. This hybridization will lead to an energy splitting of the zero-mode Majorana bound state and can serve as an important signature of Majorana physics (146). If both of the two Nb-contacted InSb nanowire segments are driven into a non-trivial topological superconducting phase (TS), in the TS-QD-TS system, due to the inner pair of the Majorana bound states are coherently coupled via the QD and thereby they are strongly influenced by the QD [see the tight banding calculation in the SI of article III]. Moreover, since the chemical potential of the QD can be tuned more effectively by the back gate than the chemical potential of the Nb-covered InSb nanowire segments, the hybridization of the inner Majorana bound states hence should be dominated by the QD. At the same time, the outer pair Majorana bound states in the TS-QD-TS system will remain at zero-energy mode since the QD influence to the outer pair Majorana bound states is much weaker than to the inner pair Majorana bound states. Then if the measurement resolution is high enough and the peak-broadening is weak, a conductance fine structure is expected in the measurements, resulting from the hybridized Majorana bound states and the zero-mode Majorana bound states.

In fact, in a close view, each ZBP structure in Figs. 5.7 shows a fine structure. In Fig. 5.8 (a)-(f), we summarized several typical fine structures chosen from Fig. 5.7 (c). Most ZBP structures in Figs. 5.7 (c) and (d) show line-shapes similar to the ones displayed in Fig. 5.8 (a)-(b) (the open-circles), i.e., a high ZBP accompanied by two small side-peaks/side-plateaus structures. In these figures, the red-dashed lines and blue-dashed lines are the Gaussian-fitting lines for the ZBPs and the side-peaks, respectively. While the solid-black lines represent the sum of the two Gaussian-fittings. It can be seen that, for both side-peaks and side-plateaus, the tripe-peak Gaussian-fitting are well matched by the experimental data. Actually, the tripe-peak Gaussian-fitting can also be matched with single broadened ZBPs which appears at some V_{bg} values, as the one shown in Fig. 5.8 (c).

This synchronization is consistent with our hypothesis that the hybridization of the inner pair of Majorana bound states are strongly influenced by the QD. When the quantum level (ground state) is far away from the Fermi levels of the TS segments, the interaction between the inner pair of Majorana bound states is

weak due to the Coulomb blockage. However, when the quantum level is aligned to the Fermi levels of the TS segments, the interaction between the inner pair of Majorana bound states is enhanced via the resonant level. The variation of the interaction leads to a change of the energies of the hybridized Majorana bound states and therefore a change of V_{sp1}.

To investigate the conductance triple-peak structure more carefully, we define V_{sp1} as the distance between the Gaussian-fitted side-peaks in the scale of V_{sd} [see definition in Fig. 5.8 (a)]. Then we extract V_{sp1} values from Figs. 5.7 (c-d) as a function of V_{bg} and plot it in Fig. 5.8 (c) (red-circles). As a background, the differential conductance measured at $V_{sd} = 100 \ \mu V$ as a function of V_{bg} is also plotted in Fig. 5.8 (c) (black solid line), which is dominated by the Coulomb oscillation. Surprisingly, the V_{sp1} is also modulated by the background conductance Coulomb oscillation. The V_{sp1} amplitude is in the range of $50 - 150 \ \mu V$ and shows a clear synchronization with the background conductance Coulomb oscillation, especially in the region $V_{bg} = 5.2 - 5.45$ V.

In Fig. 5.8 (h), we also extract and plot V_{sp1} for the conductance curves in Fig. 5.7 (g) as a function of magnetic field, along with the background conductance at $V_{sd} = 100 \ \mu V$. Comparing to the large oscillation in Fig. 5.8 (g), V_{sp1} only shows a small change as the magnetic field increases.

As shown the Figs. 5.8(d-e), at some V_{bg} values, the ZBP splits into two peaks (or a plateau structure due to the peak-broadening) and shows a quadruple-peak structure together with the side-peaks. The quadruple-peak structure is also well fitted by a Gaussian-fitting, indicated by the dashed lines in Figs. 5.8(d-e). Similar to V_{sp1}, we define V_{sp2} as the distance between the Gaussian-fitted peaks that split from the ZBP [see definition in Fig. 5.8 (d)]. The values of V_{sp2} are extracted (only for the curves with clear quadruple-peak conductance structures) and plotted in Figs. 5.8 (g) (diamonds) as a function of V_{bg}, and are plotted in Figs. 5.8 (h) (diamonds) as a function of B. As indicated by Fig. 5.8 (g), the amplitude of V_{sp2} does not show a clear synchronization with the background Coulomb oscillation. The splitting of ZBP occurs around the Coulomb conductance peaks at $V_{bg} = 5.32, 5.38, 5.51$ V. However, it does not occur at all of the resonant points, and it either does not only occur at the resonant points. The ZBP splitting even happens in the CB regions of the last four Coulomb oscillation periods in Fig. 5.8 (g). In the magnetic field dependent measurements, the splitting of ZBP occurs at the high magnetic field in Fig. 5.8

(h), while it does not show clear ZBP splitting at any magnetic field in Fig. 5.7 (h).

The splitting of ZBP, with back gate and magnetic field irregularities, can be attributed to the outer pair Majorana bound states related hybridizations. Similar to the inner pair Majorana bound state, the interaction between the outer pair of Majorana bound states is influenced by chemical potentials, Zeeman energies and the intermediary QD. Among these parameters, however, the QD is not the dominating one anymore, due to the relatively long distance between the QD and the outer pair Majorana bound states. Thus, in the conductance measurements, the splitting of the ZBP is not synchronous to the Coulomb oscillations.

In summary, the ZBPs emerging in the superconductor-semiconductor nanowire are observed as a signature of Majorana bound states. As pointed by Churchill et al. (143), other interesting transport features in an N-InSb nanowire-S structure are also observed, with both consistence and inconsistence with the interpretation of the Majorana bound states. In addition, according to the theoretical prediction, the ideal ZBP induced by Majorana bound states in tunneling experiments should have a quantized conductance of $2e^2/h$ at zero temperature (147, 148) and with a gap-closing feature (149). Finite temperature, disorders (150), multi-subbands (151), and the soft induced gap (152) in the system can all make the Majorana bound state induced ZBP much lower than $2e^2/h$. To confirm the existence of the Majorana bound states in the nanowire-superconductor hybrid devices, more systemic tests are needed, including the detection of the fractional Josephson current and the validation of the non-Abelian statistics.

5.3 Zero-bias conductance peaks without Majorana bound states

In this section, we introduce several mechanisms that can lead to the emergence of a ZBP in a finite magnetic field, or mechanisms that can lead to an enhancement of the zero-bias conductance in a finite magnetic field, in a Josephson quantum dot devices without Majorana bound states.

In Chapt. 4, we already mentioned about the field induced QPT which will lead to an emergence of ZBP in a finite magnetic field. We have also shown the magnetic field could enhance the Josephson current by increasing the ratio $T_K/\Delta(B)$ in some cases. And in the last part of Chapt. 4, we demonstrated an

anomalous low-field suppression of Josephson current (i.e., a high-field enhancement).

Besides the above mechanisms, the Kondo effect in a finite magnetic field can also lead to an emergence of ZBP. As we discussed in Chapt. 3 and Chapt. 4, the Kondo effect manifests itself as a spin-flip process, in which two spin-degenerate quantum levels are needed. In addition to the intrinsic spin-degeneracy of the quantum dot at a zero magnetic field, a quasi spin-degeneracy can be gained from different orbital states in the presence of Zeeman effect, similar to the cases shown in Figs. 3.11 (a) and 3.15 (b). Although there is an anti-crossing induced by the spin-orbit interaction, a spin-flip process can still be established if the coupling is strong. In Fig. 5.9 (a), we show the linear-conductance on a color scale as a function of V_{bg} and B, measured for Dev. *NbInSbNb#1*. At the lower-right corner, there are several horizontal high conductance stripes induced by the Kondo effect formed in the finite magnetic field. The inset of Fig. 5.9 (a) shows the differential conductance as a function of V_{sd} and B, measured at the V_{bg} position indicated by the dashed line in Fig. 5.9 (a). The dashed line crosses two Kondo resonance regimes, with one at the zero magnetic field and the other one at $B \approx 0.5$ T. It can be seen that a ZBP emerges at $B \approx 0.5$ T(as indicated by a superposed differential conductance line-cut in the inset). This ZBP can be attributed to the Kondo effect formed in a finite magnetic field. It splits quickly as the magnetic field further increases.

Figure 5.9 (b) displays the linear conductance measurements performed for another device, Dev. *NbInSbNb#3*, as a function of V_{bg} and B. We can see that due to the giant effective g-factor of the InSb quantum dot, the quantum levels shift dramatically in the magnetic field. And due to the strong dot-leads coupling, horizontal high conductance stripes that are induced by Kondo effects can be seen. Here, we fix the V_{bg} to the position indicated by the dashed line, and we measured and plotted the differential conductance as a function of V_{sd} and B in the inset of Fig. 5.9 (b). A ZBP can be identified in the range of $B \approx 0.1 - 0.35$ T in the inset. This ZBP could be attributed to the B-FET effect since a quantum resonant level gets closer to the dashed line in the finite magnetic field. However, the ZBP could also results from the field induced QPT. The quantum dot is a "0"-junction at $B = 0$ T, and it will evolve toward a magnetic doublet "π"-junction in the presence of the Zeeman effect. Therefore, the field-induced QPT could occur and lead to a ZBP (80). Figures 5.9 (c) and
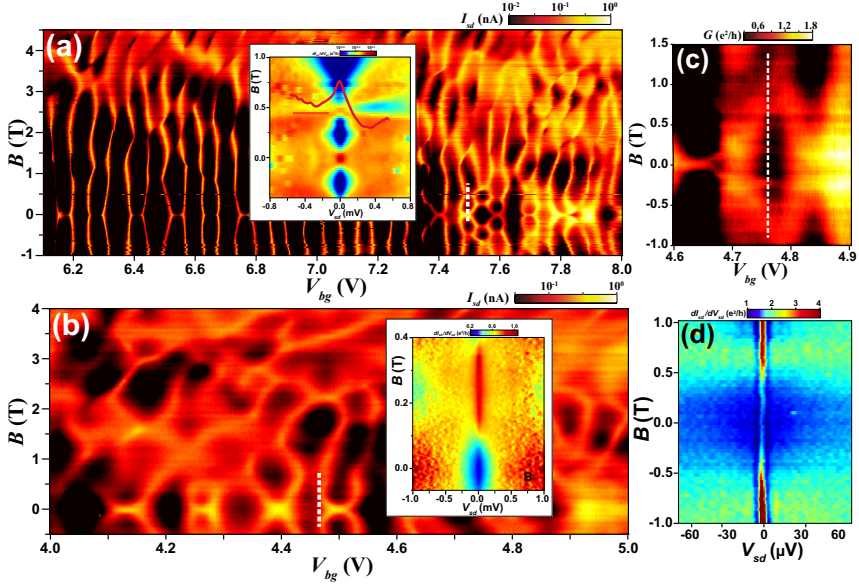
Figure 5.9: ZBP emerging in a finite magnetic field without Majorana bound state. (a) The linear-conductance on a color scale as a function of V_{bg} and B, measured for Dev. *NbInSbNb#1*. The inset shows the differential conductance as a function of V_{sd} and B, measured at the V_{bg} position indicated by the dashed line. A ZBP emerges at $B \approx 0.5$ T, as indicated by a superposed differential conductance line-cut. The ZBP is attributed to the Kondo effect formed in a finite magnetic field. (b) The same with (a) but measured for another device, Dev. *NbInSbNb#3*. The inset shows the differential conductance as a function of V_{sd} and B, measured at the V_{bg} position indicated by the dashed line. A ZBP can be clearly identified in the range of $B \approx 0.1 - 0.35$ T. This ZBP could be attributed to a B-FET effect or a field-induced QPT. (c) The same with (a) and (b), but measured for *NbInSbNb#4*. (d) The differential conductance as a function of V_{sd} and B, measured at the V_{bg} position indicated by the dashed line in (c). We can see that there is a Josephson current induced ZBP in (d), with the height peaks at $B \approx 0.7$ T. This field-enhanced ZBP clearly results from the level shifting in the magnetic field, i.e., the B-FET effect.

(d) show the similar measurements as in Fig. 5.9 (b), but measured for a different device, *NbInSbNb#4*, which has a stronger coupling. Figure 5.9(d) displays the differential conductance as a function of V_{sd} and B, measured at the V_{bg} position indicated by the dashed line in Fig. 5.9 (c). We can see that there is a Josephson current induced ZBP in Fig. 5.9 (d), with the height peaks at $B \approx 0.7$ T. This field-enhanced ZBP clearly results from the level shifting in the magnetic field, i.e., the B-FET effect.

Moreover, there are some anomalous ZBPs in Josephson quantum dot devices without Majorana bound state (76), which have not been clearly understood. As an example, Fig. 5.10 shows an anomalous ZBP that arises from Dev. *AlInSbAl#3*. Fig. 5.10 (a) shows a charge stability diagram which has been already shown in Fig. 4.32 (d). Figure 5.10 (b) displays the differential conductance as a function of V_{sd} and B, measured at the V_{bg} position indicated by the dashed line in Fig. 5.10 (a). Figure 5.10 (c) shows the differential conductance as a function of V_{sd} and B in a line-cut plot, corresponded to the rectangled region in Fig. 5.10 (b). It is evident that a ZBP appears at $B \approx 18$ mT. We are not clear about its physical origin.

Consequently, there are a several mechanisms could result in ZBPs in a finite magnetic field without Majorana bound state. Special attentions should be paid on these ZBP in the search for Majorana fermions in semiconductor nanowire-superconductor hybrid devices.
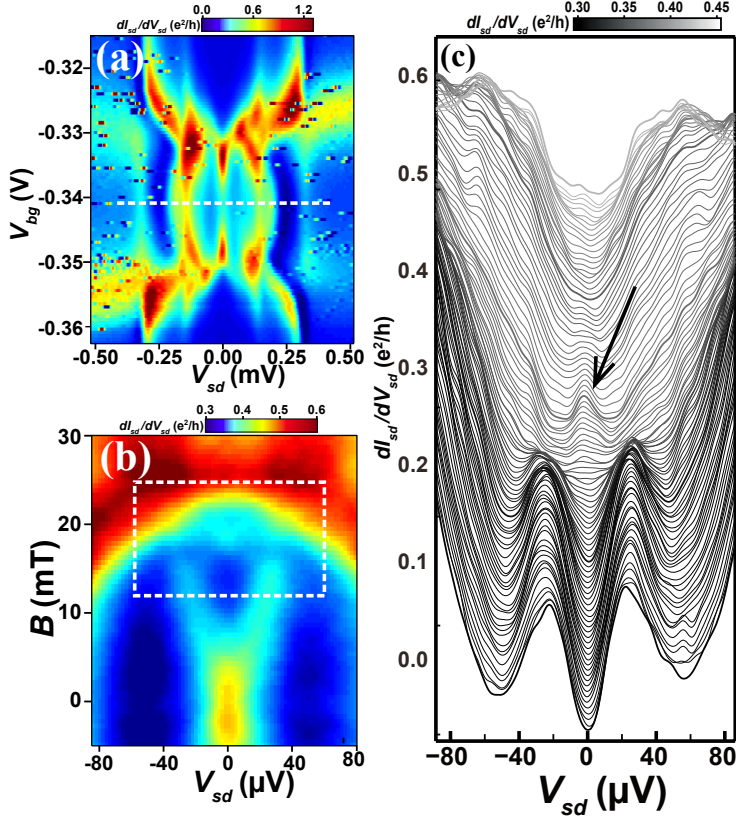
Figure 5.10: An anomalous ZBP emerging in a finite magnetic field in Dev. *AlInSbAl#3*. (a) The charge stability diagram which has been already shown in Fig. 4.32 (d). (b) The differential conductance as a function of V_{sd} and B, measured at the V_{bg} position indicated by the dashed line in (a). (c) The differential conductance as a function of V_{sd} and B in a line-cut plot, corresponded to the rectangled region in (b). It is evident that a ZBP appears at $B \approx 18$ mT.

Bibliography

[1] L. P. Kouwenhoven, C. Marcus, P. L. McEuen, S. Tarucha, R. M. Westervelt, and N. S. Wingreen, "Electron transport in quantum dots," *NATO ASI Series E Applied Sciences-Advanced Study Institute*, vol. 345, pp. 105–214, 1997. 2, 15

[2] D. K. Ferry, S. M. Goodnick, and J. P. Bird, *Transport in nanostructures*. Cambridge University Press, 2009. 2, 15

[3] G. E. Moore *et al.*, "Cramming more components onto integrated circuits," 1965. 2

[4] M. A. Kastner, "The single-electron transistor," *Rev. Mod. Phys.*, vol. 64, pp. 849–858, Jul 1992. 3

[5] M. A. Nielsen and I. L. Chuang, *Quantum computation and quantum information*. Cambridge university press, 2010. 3

[6] Y. Makhlin, G. Schön, and A. Shnirman, "Quantum-state engineering with josephson-junction devices," *Reviews of modern physics*, vol. 73, no. 2, p. 357, 2001. 3, 74

[7] S. Shafranjuk, I. Nevirkovets, and J. Ketterson, "A qubit device based on manipulations of andreev bound states in double-barrier josephson junctions," *Solid state communications*, vol. 121, no. 9, pp. 457–460, 2002. 3

[8] A. Y. Kitaev, "Unpaired majorana fermions in quantum wires," *Physics-Uspekhi*, vol. 44, no. 10S, p. 131, 2001. 3, 121

[9] C. Nayak, S. H. Simon, A. Stern, M. Freedman, and S. D. Sarma, "Non-abelian anyons and topological quantum computation," *Reviews of Modern Physics*, vol. 80, no. 3, p. 1083, 2008. 3, 74, 121

[10] P. Caroff, J. B. Wagner, K. A. Dick, H. A. Nilsson, M. Jeppsson, K. Deppert, L. Samuelson, L. Wallenberg, and L.-E. Wernersson, "High-quality inas/insb nanowire heterostructures grown by metal–organic vapor-phase epitaxy," *Small*, vol. 4, no. 7, pp. 878–882, 2008. 7

[11] P. Caroff, M. E. Messing, B. M. Borg, K. A. Dick, K. Deppert, and L.-E. Wernersson, "Insb heterostructure nanowires: Movpe growth under extreme lattice mismatch," *Nanotechnology*, vol. 20, no. 49, p. 495606, 2009. 7

[12] C. Thelander, P. Caroff, S. Plissard, and K. A. Dick, "Electrical properties of inas$_{1-x}$sb$_x$ and insb nanowires grown by molecular beam epitaxy," *Applied Physics Letters*, vol. 100, no. 23, pp. 232105–232105, 2012. 7

[13] D. Suyatin, C. Thelander, M. Björk, I. Maximov, and L. Samuelson, "Sulfur passivation for ohmic contact formation to inas nanowires," *Nanotechnology*, vol. 18, no. 10, p. 105307, 2007. 13

[14] I. Vurgaftman, J. Meyer, and L. Ram-Mohan, "Band parameters for iii–v compound semiconductors and their alloys," *Journal of applied physics*, vol. 89, no. 11, pp. 5815–5875, 2001. 27, 30

[15] C. R. Pidgeon and R. N. Brown, "Interband magneto-absorption and faraday rotation in insb," *Phys. Rev.*, vol. 146, pp. 575–583, Jun 1966. 30

[16] V. Pribiag, S. Nadj-Perge, S. Frolov, J. van den Berg, I. van Weperen, S. Plissard, E. Bakkers, and L. Kouwenhoven, "Electrical control of single hole spins in nanowire quantum dots," *Nature nanotechnology*, vol. 8, no. 3, pp. 170–174, 2013. 32, 50

[17] S. Roddaro, A. Fuhrer, P. Brusheim, C. Fasth, H. Xu, L. Samuelson, J. Xiang, and C. Lieber, "Spin states of holes in ge/si nanowire quantum dots," *Physical review letters*, vol. 101, no. 18, p. 186802, 2008. 32

[18] T. Fujisawa, G. Shinkai, and T. Hayashi, "Zeeman splitting in single-electron transport through a few-electron quantum dot," *Physical Review B*, vol. 76, no. 4, p. 041302, 2007. 32

[19] H. Kosaka, A. A. Kiselev, F. A. Baron, K. W. Kim, and E. Yablonovitch, "Electron g factor engineering in ili-v semiconductors for quantum communications," *Electronics Letters*, vol. 37, no. 7, pp. 464–465, 2001. 33

[20] H. A. Nilsson, P. Caroff, C. Thelander, M. Larsson, J. B. Wagner, L.-E. Wernersson, L. Samuelson, and H. Xu, "Giant, level-dependent g factors in insb nanowire quantum dots," *Nano letters*, vol. 9, no. 9, pp. 3151–3156, 2009. 33, 123

[21] R. Lai, H. Churchill, and C. Marcus, "g-tensor control in bent carbon nanotube quantum dots," *arXiv preprint arXiv:1210.6402*, 2012. 33

[22] S. Csonka, L. Hofstetter, F. Freitag, S. Oberholzer, C. Schonenberger, T. S. Jespersen, M. Aagesen, and J. Nygård, "Giant fluctuations and gate control of the g-factor in inas nanowire quantum dots," *Nano letters*, vol. 8, no. 11, pp. 3932–3935, 2008. 33

[23] R. A. Isaacson, "Electron spin resonance in *n*-type insb," *Phys. Rev.*, vol. 169, pp. 312–314, May 1968. 33

[24] S. De Franceschi and W. G. Wiel, "Kondo effect in quantum dots," *Handbook of Nanophysics: Nanoparticles and Quantum Dots*, pp. 646–664, 2010. 35

[25] S. De Franceschi, S. Sasaki, J. Elzerman, W. Van Der Wiel, S. Tarucha, and L. P. Kouwenhoven, "Electron cotunneling in a semiconductor quantum dot," *Physical review letters*, vol. 86, no. 5, p. 878, 2001. 35

[26] R. Schleser, T. Ihn, E. Ruh, K. Ensslin, M. Tews, D. Pfannkuche, D. C. Driscoll, and A. C. Gossard, "Cotunneling-mediated transport through excited states in the coulomb-blockade regime," *Phys. Rev. Lett.*, vol. 94, p. 206805, May 2005. 36

[27] J. Aghassi, M. H. Hettler, and G. Schon, "Cotunneling assisted sequential tunneling in multilevel quantum dots," *Applied Physics Letters*, vol. 92, no. 20, pp. 202101–202101, 2008. 36

[28] C. Fasth, A. Fuhrer, L. Samuelson, V. N. Golovach, and D. Loss, "Direct measurement of the spin-orbit interaction in a two-electron inas nanowire quantum dot," *Phys. Rev. Lett.*, vol. 98, p. 266801, Jun 2007. 40

[29] V. N. Golovach, A. Khaetskii, and D. Loss, "Spin relaxation at the singlet-triplet crossing in a quantum dot," *Phys. Rev. B*, vol. 77, p. 045328, Jan 2008. 40

[30] J. Kondo, "Resistance minimum in dilute magnetic alloys," *Progress of theoretical physics*, vol. 32, no. 1, pp. 37–49, 1964. 40

[31] Y. Meir, N. S. Wingreen, and P. A. Lee, "Low-temperature transport through a quantum dot: The anderson model out of equilibrium," *Phys. Rev. Lett.*, vol. 70, pp. 2601–2604, Apr 1993. 40

[32] D. Goldhaber-Gordon, H. Shtrikman, D. Mahalu, D. Abusch-Magder, U. Meirav, and M. Kastner, "Kondo effect in a single-electron transistor," *Nature*, vol. 391, no. 6663, pp. 156–159, 1998. 42

[33] S. M. Cronenwett, T. H. Oosterkamp, and L. P. Kouwenhoven, "A tunable kondo effect in quantum dots," *Science*, vol. 281, no. 5376, pp. 540–544, 1998. 42

[34] L. Kouwenhoven and L. Glazman, "Revival of the kondo effect," *Physics World*, p. 33, 2001. 42

[35] N. S. Wingreen and Y. Meir, "Anderson model out of equilibrium: Noncrossing-approximation approach to transport through a quantum dot," *Phys. Rev. B*, vol. 49, pp. 11040–11052, Apr 1994. 46

[36] A. Kogan, S. Amasha, D. Goldhaber-Gordon, G. Granger, M. A. Kastner, and H. Shtrikman, "Measurements of kondo and spin splitting in single-electron transistors," *Phys. Rev. Lett.*, vol. 93, p. 166602, Oct 2004. 46, 110

[37] T. A. Costi, "Kondo effect in a magnetic field and the magnetoresistivity of kondo alloys," *Phys. Rev. Lett.*, vol. 85, pp. 1504–1507, Aug 2000. 49, 102, 110

[38] J. E. Moore and X.-G. Wen, "Anomalous magnetic splitting of the kondo resonance," *Phys. Rev. Lett.*, vol. 85, pp. 1722–1725, Aug 2000. 49

[39] C. H. L. Quay, J. Cumings, S. J. Gamble, R. d. Picciotto, H. Kataura, and D. Goldhaber-Gordon, "Magnetic field dependence of the spin-$\frac{1}{2}$ and spin-1 kondo effects in a quantum dot," *Phys. Rev. B*, vol. 76, p. 245311, Dec 2007. 49

[40] C. Escott, F. Zwanenburg, and A. Morello, "Resonant tunnelling features in quantum dots," *Nanotechnology*, vol. 21, no. 27, p. 274018, 2010. 50

[41] H. K. Onnes, "Resistance measurements of mercury at liquid helium temperature," *Commun. Phys. Lab. Univ. Leiden*, vol. 119b, 120b, 122b, 123a, 1911. 55

[42] "High-tc superconductivity record reaches 38°C." `http://www.superconductors.org/38C_rec.htm`. Accessed: 2013-07-29. 56

[43] W. Meissner and R. Ochsenfeld, "Ein neuer effekt bei eintritt der supraleitfähigkeit," *Naturwissenschaften*, vol. 21, no. 44, pp. 787–788, 1933. 56

[44] J. Bardeen, L. N. Cooper, and J. R. Schrieffer, "Theory of superconductivity," *Phys. Rev.*, vol. 108, pp. 1175–1204, Dec 1957. 56

[45] M. Tinkham, *Introduction to Superconductivity: (Dover Books on Physics)(Vol i)*. Dover publications, 2004. 58, 62, 72

[46] A. A. Abrikosov, "Magnetic properties of superconductors of the second group," *Sov. Phys.-JETP (Engl. Transl.);(United States)*, vol. 5, no. 6, 1957. 59

[47] T. Matsushita, *Flux pinning in superconductors*. Springer London, Limited, 2007. 59

[48] D. Dew-Hughes, "The critical current of superconductors: an historical review," *Low Temperature Physics*, vol. 27, p. 713, 2001. 60

[49] M. Tinkham, J. U. Free, C. N. Lau, and N. Markovic, "Hysteretic $i - v$ curves of superconducting nanowires," *Phys. Rev. B*, vol. 68, p. 134515, Oct 2003. 60

[50] S. Bose, P. Raychaudhuri, R. Banerjee, P. Vasa, and P. Ayyub, "Mechanism of the size dependence of the superconducting transition of nanostructured nb," *Physical review letters*, vol. 95, no. 14, p. 147003, 2005. 62

[51] M. Deng, C. Yu, G. Huang, M. Larsson, P. Caroff, and H. Xu, "Anomalous zero-bias conductance peak in a nb–insb nanowire–nb hybrid device," *Nano letters*, vol. 12, no. 12, pp. 6414–6419, 2012. 62, 70, 123

[52] M. Deng, C. Yu, G. Huang, M. Larsson, P. Caroff, and H. Xu, "Parity independence of the anomalous zero-bias conductance peak in a superconductor-coupled nanowire quantum device," *To be submitted*, 2013. 62

[53] D. Ralph, C. Black, and M. Tinkham, "Spectroscopic measurements of discrete electronic states in single metal particles," *Physical review letters*, vol. 74, no. 16, p. 3241, 1995. 63

[54] Y.-J. Doh, S. D. Franceschi, E. P. Bakkers, and L. P. Kouwenhoven, "Andreev reflection versus coulomb blockade in hybrid semiconductor nanowire devices," *Nano letters*, vol. 8, no. 12, pp. 4098–4102, 2008. 63

[55] J. Rodrigo, H. Suderow, and S. Vieira, "On the use of stm superconducting tips at very low temperatures," *The European Physical Journal B-Condensed Matter and Complex Systems*, vol. 40, no. 4, pp. 483–488, 2004. 65

[56] F. Reinert, G. Nicolay, B. Eltner, D. Ehm, S. Schmidt, S. Hüfner, U. Probst, and E. Bucher, "Observation of a bcs spectral function in a conventional superconductor by photoelectron spectroscopy," *Physical Review Letters*, vol. 85, no. 18, p. 3930, 2000. 65, 68

[57] C. B. Whan and T. P. Orlando, "Transport properties of a quantum dot with superconducting leads," *Phys. Rev. B*, vol. 54, pp. R5255–R5258, Aug 1996. 68

[58] R. C. Dynes, J. P. Garno, G. B. Hertel, and T. P. Orlando, "Tunneling study of superconductivity near the metal-insulator transition," *Phys. Rev. Lett.*, vol. 53, pp. 2437–2440, Dec 1984. 68, 86

[59] S. Datta, *Quantum transport: atom to transistor*. Cambridge University Press, 2005. 68

[60] B. D. Josephson, "Possible new effects in superconductive tunnelling," *Physics Letters*, vol. 1, no. 7, pp. 251–253, 1962. 69

[61] R. Holm and W. Meissner, "Kontaktwiderstand zwischen supraleitern und nichtsupraleitern," *Z. Physik*, vol. 74, p. 715, 1932. 69

[62] H. Meissner, "Superconductivity of contacts with interposed barriers," *Phys. Rev.*, vol. 117, pp. 672–680, Feb 1960. 69

[63] Y.-J. Doh, J. A. van Dam, A. L. Roest, E. P. Bakkers, L. P. Kouwenhoven, and S. De Franceschi, "Tunable supercurrent through semiconductor nanowires," *science*, vol. 309, no. 5732, pp. 272–275, 2005. 70, 72, 74

[64] A. Y. Kasumov, R. Deblock, M. Kociak, B. Reulet, H. Bouchiat, I. Khodos, Y. B. Gorbatov, V. Volkov, C. Journet, and M. Burghard, "Supercurrents through single-walled carbon nanotubes," *Science*, vol. 284, no. 5419, pp. 1508–1511, 1999. 70

[65] S. Abay, D. Persson, H. Nilsson, H. Xu, M. Fogelström, V. Shumeiko, and P. Delsing, "Quantized conductance and its correlation to the supercurrent in a nanowire connected to superconductors," *arXiv preprint arXiv:1306.0396*, 2013. 70

[66] H. Nilsson, P. Samuelsson, P. Caroff, and H. Xu, "Supercurrent and multiple andreev reflections in an insb nanowire josephson junction," *Nano letters*, vol. 12, no. 1, pp. 228–233, 2011. 70, 72, 74, 123

[67] Y. Makhlin, G. Scöhn, and A. Shnirman, "Josephson-junction qubits with controlled couplings," *nature*, vol. 398, no. 6725, pp. 305–307, 1999. 74

[68] R. C. Jaklevic, J. Lambe, A. H. Silver, and J. E. Mercereau, "Quantum interference effects in josephson tunneling," *Phys. Rev. Lett.*, vol. 12, pp. 159–160, Feb 1964. 74

[69] Y. Aharonov and D. Bohm, "Significance of electromagnetic potentials in the quantum theory," *Phys. Rev.*, vol. 115, pp. 485–491, Aug 1959. 75

[70] J. Clarke and A. I. Braginski, *The SQUID handbook*. Wiley Online Library, 2004. 75

[71] J.-P. Cleuziou, W. Wernsdorfer, V. Bouchiat, T. Ondarçuhu, and M. Monthioux, "Carbon nanotube superconducting quantum interference device," *Nature nanotechnology*, vol. 1, no. 1, pp. 53–59, 2006. 75

[72] R. Maurand, T. Meng, E. Bonet, S. Florens, L. Marty, and W. Wernsdorfer, "First-order 0-π quantum phase transition in the kondo regime of a superconducting carbon-nanotube quantum dot," *Physical Review X*, vol. 2, no. 1, p. 011009, 2012. 75

[73] G. Hernández, *Fabry-Perot Interferometers*, vol. 3. Cambridge University Press, 1988. 78

[74] H. van Houten and C. Beenakker, "Andreev reflection and the josephson effect in a quantum point contact: An analogy with phase-conjugating resonators," *Physica B: Condensed Matter*, vol. 175, no. 1, pp. 187–197, 1991. 78

[75] J. Pillet, C. Quay, P. Morfin, C. Bena, A. L. Yeyati, and P. Joyez, "Andreev bound states in supercurrent-carrying carbon nanotubes revealed," *Nature Physics*, vol. 6, no. 12, pp. 965–969, 2010. 79

[76] W. Chang, V. E. Manucharyan, T. S. Jespersen, J. Nygård, and C. M. Marcus, "Tunneling spectroscopy of quasiparticle bound states in a spinful josephson junction," *Phys. Rev. Lett.*, vol. 110, p. 217005, May 2013. 79, 141

[77] R. Deacon, Y. Tanaka, A. Oiwa, R. Sakano, K. Yoshida, K. Shibata, K. Hirakawa, and S. Tarucha, "Tunneling spectroscopy of andreev energy levels in a quantum dot coupled to a superconductor," *Physical review letters*, vol. 104, no. 7, p. 076805, 2010. 79

[78] R. Deacon, Y. Tanaka, A. Oiwa, R. Sakano, K. Yoshida, K. Shibata, K. Hirakawa, and S. Tarucha, "Kondo-enhanced andreev transport in single self-assembled inas quantum dots contacted with normal and superconducting leads," *Physical Review B*, vol. 81, no. 12, p. 121308, 2010. 79

[79] T. Dirks, T. L. Hughes, S. Lal, B. Uchoa, Y.-F. Chen, C. Chialvo, P. M. Goldbart, and N. Mason, "Transport through andreev bound states in a graphene quantum dot," *Nature Physics*, vol. 7, no. 5, pp. 386–390, 2011. 79

[80] E. J. Lee, X. Jiang, M. Houzet, R. Aguado, C. M. Lieber, and S. De Franceschi, "Spin-resolved andreev levels in hybrid superconductor-semiconductor nanostructures," *arXiv preprint arXiv:1302.2611*, 2013. 79, 89, 108, 114, 139

[81] J.-D. Pillet, P. Joyez, R. Žitko, and M. F. Goffman, "Tunneling spectroscopy of a single quantum dot coupled to a superconductor: From kondo ridge to andreev bound states," *Phys. Rev. B*, vol. 88, p. 045101, Jul 2013. 79

[82] M. Octavio, M. Tinkham, G. E. Blonder, and T. M. Klapwijk, "Subharmonic energy-gap structure in superconducting constrictions," *Phys. Rev. B*, vol. 27, pp. 6739–6746, Jun 1983. 79

[83] K. Grove-Rasmussen, H. I. Jørgensen, B. M. Andersen, J. Paaske, T. S. Jespersen, J. Nygård, K. Flensberg, and P. E. Lindelof, "Superconductivity-enhanced bias spectroscopy in carbon nanotube quantum dots," *Physical Review B*, vol. 79, no. 13, p. 134518, 2009. 82

[84] T. D. Stanescu and S. Das Sarma, "Superconducting proximity effect in semiconductor nanowires," *Phys. Rev. B*, vol. 87, p. 180504, May 2013. 86

[85] S. Takei, B. M. Fregoso, H.-Y. Hui, A. M. Lobos, and S. Das Sarma, "Soft superconducting gap in semiconductor majorana nanowires," *Phys. Rev. Lett.*, vol. 110, p. 186803, Apr 2013. 86

[86] A. Kumar, M. Gaim, D. Steininger, A. L. Yeyati, A. Martin-Rodero, A. Huettel, and C. Strunk, "Temperature dependence of andreev spectra in a superconducting carbon nanotube quantum dot," *arXiv preprint arXiv:1308.1020*, 2013. 86

[87] C. Buizert, A. Oiwa, K. Shibata, K. Hirakawa, and S. Tarucha, "Kondo universal scaling for a quantum dot coupled to superconducting leads," *Phys. Rev. Lett.*, vol. 99, p. 136806, Sep 2007. 95, 98

[88] A. Eichler, M. Weiss, S. Oberholzer, C. Schönenberger, A. Levy Yeyati, J. C. Cuevas, and A. Martin-Rodero, "Even-odd effect in andreev transport through a carbon nanotube quantum dot," *Phys. Rev. Lett.*, vol. 99, p. 126602, Sep 2007. 95

[89] T. Sand-Jespersen, J. Paaske, B. M. Andersen, K. Grove-Rasmussen, H. I. Jørgensen, M. Aagesen, C. B. Sørensen, P. E. Lindelof, K. Flensberg, and J. Nygård, "Kondo-enhanced andreev tunneling in inas nanowire quantum dots," *Phys. Rev. Lett.*, vol. 99, p. 126603, Sep 2007. 95

[90] Y. Kanai, R. Deacon, A. Oiwa, K. Yoshida, K. Shibata, K. Hirakawa, and S. Tarucha, "Electrical control of kondo effect and superconducting transport in a side-gated inas quantum dot josephson junction," *Physical Review B*, vol. 82, no. 5, p. 054512, 2010. 95

[91] B. M. Andersen, K. Flensberg, V. Koerting, and J. Paaske, "Nonequilibrium transport through a spinful quantum dot with superconducting leads," *Physical review letters*, vol. 107, no. 25, p. 256802, 2011. 95

[92] V. Koerting, B. M. Andersen, K. Flensberg, and J. Paaske, "Nonequilibrium transport via spin-induced subgap states in superconductor/quantum dot/normal metal cotunnel junctions," *Physical Review B*, vol. 82, no. 24, p. 245108, 2010. 95

[93] L. Yu, "Bound state in superconductors with paramagnetic impurities," *Acta physica sinica*, vol. 21, no. 1, p. 75, 1965. 97

[94] H. Shiba, "Classical spins in superconductors," *Progress of theoretical Physics*, vol. 40, no. 3, pp. 435–451, 1968. 97

[95] A. Rusinov, "Theory of gapless superconductivity in alloys containing paramagnetic impurities," *Sov. Phys. JETP*, vol. 29, no. 6, pp. 1101–1106, 1969. 97

[96] A. Yazdani, B. Jones, C. Lutz, M. Crommie, and D. Eigler, "Probing the local effects of magnetic impurities on superconductivity," *Science*, vol. 275, no. 5307, pp. 1767–1770, 1997. 97

[97] K. Franke, G. Schulze, and J. Pascual, "Competition of superconducting phenomena and kondo screening at the nanoscale," *Science*, vol. 332, no. 6032, pp. 940–944, 2011. 98

[98] V. Mourik, K. Zuo, S. Frolov, S. Plissard, E. Bakkers, and L. Kouwenhoven, "Signatures of majorana fermions in hybrid superconductor-semiconductor nanowire devices," *Science*, vol. 336, no. 6084, pp. 1003–1007, 2012. 99, 123, 125, 128

[99] L. Glazman and K. Matveev, "Resonant josephson current through kondo impurities in a tunnel barrier," *JETP Lett*, vol. 49, no. 10, pp. 659–662, 1989. 99

[100] F. Siano and R. Egger, "Josephson current through a nanoscale magnetic quantum dot," *Phys. Rev. Lett.*, vol. 93, p. 047002, Jul 2004. 99

[101] M.-S. Choi, M. Lee, K. Kang, and W. Belzig, "Kondo effect and josephson current through a quantum dot between two superconductors," *Phys. Rev. B*, vol. 70, p. 020502, Jul 2004. 99

[102] M. R. Buitelaar, T. Nussbaumer, and C. Schönenberger, "Quantum dot in the kondo regime coupled to superconductors," *Phys. Rev. Lett.*, vol. 89, p. 256801, Dec 2002. 99

[103] K. Grove-Rasmussen, H. I. Jørgensen, and P. E. Lindelof, "Kondo resonance enhanced supercurrent in single wall carbon nanotube josephson junctions," *New Journal of Physics*, vol. 9, no. 5, p. 124, 2007. 99

[104] H. I. Jørgensen, T. Novotnỳ, K. Grove-Rasmussen, K. Flensberg, and P. E. Lindelof, "Critical current 0-π transition in designed josephson quantum dot junctions," *Nano letters*, vol. 7, no. 8, pp. 2441–2445, 2007. 99, 113

[105] P. Jarillo-Herrero, J. A. Van Dam, and L. P. Kouwenhoven, "Quantum supercurrent transistors in carbon nanotubes," *Nature*, vol. 439, no. 7079, pp. 953–956, 2006. 100, 113

[106] M. Buitelaar, W. Belzig, T. Nussbaumer, B. Babić, C. Bruder, and C. Schönenberger, "Multiple andreev reflections in a carbon nanotube quantum dot.," *Phys Rev Lett*, vol. 91, no. 5, p. 057005, 2003. 100, 104

[107] F. Deon, V. Pellegrini, F. Giazotto, G. Biasiol, L. Sorba, and F. Beltram, "Proximity effect in a two-dimensional electron gas probed with a lateral quantum dot," *Physical Review B*, vol. 84, no. 10, p. 100506, 2011. 106

[108] E. J. Lee, X. Jiang, R. Aguado, G. Katsaros, C. M. Lieber, and S. De Franceschi, "Zero-bias anomaly in a nanowire quantum dot coupled to superconductors," *Physical review letters*, vol. 109, no. 18, p. 186802, 2012. 110

[109] Y. M. I. ANCHENKO and L. Zil'Berman, "The josephson effect in small tunnel contacts," *Soviet Physics JETP*, vol. 28, no. 6, 1969. 113

[110] A. Steinbach, P. Joyez, A. Cottet, D. Esteve, M. Devoret, M. Huber, and J. Martinis, "Direct measurement of the josephson supercurrent in an ultrasmall josephson junction.," *Physical review letters*, vol. 87, no. 13, pp. 137003–137003, 2001. 113

[111] H. I. Jørgensen, K. Grove-Rasmussen, T. Novotný, K. Flensberg, and P. E. Lindelof, "Electron transport in single-wall carbon nanotube weak links in the fabry-perot regime," *Phys. Rev. Lett.*, vol. 96, p. 207003, May 2006. 116

[112] M. Tian, N. Kumar, S. Xu, J. Wang, J. S. Kurtz, and M. H. W. Chan, "Suppression of superconductivity in zinc nanowires by bulk superconductors," *Phys. Rev. Lett.*, vol. 95, p. 076802, Aug 2005. 118

[113] A. Rogachev, T.-C. Wei, D. Pekker, A. T. Bollinger, P. M. Goldbart, and A. Bezryadin, "Magnetic-field enhancement of superconductivity in ultranarrow wires," *Phys. Rev. Lett.*, vol. 97, p. 137001, Sep 2006. 118

[114] H. J. Gardner, A. Kumar, L. Yu, P. Xiong, M. P. Warusawithana, L. Wang, O. Vafek, and D. G. Schlom, "Enhancement of superconductivity by a parallel magnetic field in two-dimensional superconductors," *Nature physics*, vol. 7, no. 11, pp. 895–900, 2011. 118

[115] E. Majorana, "eoria simmetrica dellelettrone e del positrone," *Nuovo Cimento*, vol. 14, no. 1, p. 171, 1937. 120

[116] M. Moe and P. Vogel, "Double beta decay," *Annual review of Nuclear and Particle science*, vol. 44, no. 1, pp. 247–283, 1994. 120

[117] S. R. Elliott and P. Vogel, "Double beta decay," *Annual review of Nuclear and Particle science*, vol. 52, no. 1, pp. 115–151, 2002. 120

[118] S. Faber and R. E. Jackson, "Velocity dispersions and mass-to-light ratios for elliptical galaxies," *The Astrophysical Journal*, vol. 204, pp. 668–683, 1976. 120

[119] R. Oerter, *The theory of almost everything: The standard model, the unsung triumph of modern physics*. Penguin. com, 2006. 120

[120] G. Steigman and M. S. Turner, "Cosmological constraints on the properties of weakly interacting massive particles," *Nuclear Physics B*, vol. 253, pp. 375–386, 1985. 120

[121] G. Jungman, M. Kamionkowski, and K. Griest, "Supersymmetric dark matter," *Physics Reports*, vol. 267, no. 5, pp. 195–373, 1996. 120

[122] F. Wilczek, "Majorana returns," *Nature Physics*, vol. 5, no. 9, pp. 614–618, 2009. 120

[123] M. Franz, "Race for majorana fermions," *Physics*, vol. 3, p. 24, 2010. 120

[124] C. Beenakker, "Search for majorana fermions in superconductors," *Annual Review of Condensed Matter Physics*, vol. 4, pp. 113–136, 2013. 120

[125] M. Leijnse and K. Flensberg, "Introduction to topological superconductivity and majorana fermions," *Semiconductor Science and Technology*, vol. 27, no. 12, p. 124003, 2012. 120

[126] J. Alicea, "New directions in the pursuit of majorana fermions in solid state systems," *Reports on Progress in Physics*, vol. 75, no. 7, p. 076501, 2012. 120

[127] X.-L. Qi, T. L. Hughes, S. Raghu, and S.-C. Zhang, "Time-reversal-invariant topological superconductors and superfluids in two and three dimensions," *Physical review letters*, vol. 102, no. 18, p. 187001, 2009. 120

[128] G. Moore and N. Read, "Nonabelions in the fractional quantum hall effect," *Nuclear Physics B*, vol. 360, no. 2, pp. 362–396, 1991. 120

[129] N. Read and D. Green, "Paired states of fermions in two dimensions with breaking of parity and time-reversal symmetries and the fractional quantum hall effect," *Physical Review B*, vol. 61, no. 15, p. 10267, 2000. 120

[130] L. Fu and C. L. Kane, "Superconducting proximity effect and majorana fermions at the surface of a topological insulator," *Physical review letters*, vol. 100, no. 9, p. 096407, 2008. 120

[131] J. D. Sau, R. M. Lutchyn, S. Tewari, and S. D. Sarma, "Generic new platform for topological quantum computation using semiconductor heterostructures," *Physical review letters*, vol. 104, no. 4, p. 040502, 2010. 120, 125

[132] J. Alicea, "Majorana fermions in a tunable semiconductor device," *Physical Review B*, vol. 81, no. 12, p. 125318, 2010. 120

[133] R. M. Lutchyn, J. D. Sau, and S. D. Sarma, "Majorana fermions and a topological phase transition in semiconductor-superconductor heterostructures," *Physical review letters*, vol. 105, no. 7, p. 077001, 2010. 120, 125

[134] Y. Oreg, G. Refael, and F. von Oppen, "Helical liquids and majorana bound states in quantum wires," *Physical review letters*, vol. 105, no. 17, p. 177002, 2010. 120, 125

[135] X. Wen, "Non-abelian statistics in the fractional quantum hall states," *Physical review letters*, vol. 66, no. 6, pp. 802–805, 1991. 121

[136] A. Stern, "Non-abelian states of matter," *Nature*, vol. 464, no. 7286, pp. 187–193, 2010. 121

[137] J. Alicea, Y. Oreg, G. Refael, F. von Oppen, and M. P. Fisher, "Non-abelian statistics and topological quantum information processing in 1d wire networks," *Nature Physics*, vol. 7, no. 5, pp. 412–417, 2011. 121

[138] J. P. Stanley, N. Pattinson, C. J. Lambert, and J. H. Jefferson, "Rashba spin-splitting in narrow gap iii–v semiconductor quantum wells," *Physica E: Low-dimensional Systems and Nanostructures*, vol. 20, no. 3, pp. 433–435, 2004. 123

[139] M. Leontiadou, K. Litvinenko, A. Gilbertson, C. Pidgeon, W. Branford, L. Cohen, M. Fearn, T. Ashley, M. Emeny, B. Murdin, *et al.*, "Experimental determination of the rashba coefficient in insb/inalsb quantum wells at zero magnetic field and elevated temperatures," *Journal of Physics: Condensed Matter*, vol. 23, no. 3, p. 035801, 2011. 123

[140] G. Khodaparast, R. Doezema, S. Chung, K. Goldammer, and M. Santos, "Spectroscopy of rashba spin splitting in insb quantum wells," *Physical Review B*, vol. 70, no. 15, p. 155322, 2004. 123

[141] L. P. Rokhinson, X. Liu, and J. K. Furdyna, "The fractional ac josephson effect in a semiconductor-superconductor nanowire as a signature of majorana particles," *Nature Physics*, vol. 8, no. 11, pp. 795–799, 2012. 123

[142] M. Deng, C. Yu, G. Huang, M. Larsson, P. Caroff, and H. Xu, "Observation of majorana fermions in a nb-insb nanowire-nb hybrid quantum device," *arXiv preprint arXiv:1204.4130*, 2012. 123

[143] H. O. H. Churchill, V. Fatemi, K. Grove-Rasmussen, M. T. Deng, P. Caroff, H. Q. Xu, and C. M. Marcus, "Superconductor-nanowire devices from tunneling to the multichannel regime: Zero-bias oscillations and magnetoconductance crossover," *Phys. Rev. B*, vol. 87, p. 241401, Jun 2013. 123, 125, 138

[144] M. Leijnse and K. Flensberg, "Scheme to measure majorana fermion lifetimes using a quantum dot," *Phys. Rev. B*, vol. 84, p. 140501, Oct 2011. 128

[145] D. Pikulin, J. Dahlhaus, M. Wimmer, H. Schomerus, and C. Beenakker, "A zero-voltage conductance peak from weak antilocalization in a majorana nanowire," *New Journal of Physics*, vol. 14, no. 12, p. 125011, 2012. 131

[146] S. D. Sarma, J. D. Sau, and T. D. Stanescu, "Splitting of the zero-bias conductance peak as smoking gun evidence for the existence of the majorana mode in a superconductor-semiconductor nanowire," *Physical Review B*, vol. 86, no. 22, p. 220506, 2012. 136

[147] K. T. Law, P. A. Lee, and T. Ng, "Majorana fermion induced resonant andreev reflection," *Physical review letters*, vol. 103, no. 23, p. 237001, 2009. 138

[148] J. D. Sau, S. Tewari, R. M. Lutchyn, T. D. Stanescu, and S. D. Sarma, "Non-abelian quantum order in spin-orbit-coupled semiconductors: Search for topological majorana particles in solid-state systems," *Physical Review B*, vol. 82, no. 21, p. 214509, 2010. 138

[149] T. D. Stanescu, R. M. Lutchyn, and S. Das Sarma, "Majorana fermions in semiconductor nanowires," *Phys. Rev. B*, vol. 84, p. 144522, Oct 2011. 138

[150] J. D. Sau and S. Das Sarma, "Density of states of disordered topological superconductor-semiconductor hybrid nanowires," *Phys. Rev. B*, vol. 88, p. 064506, Aug 2013. 138

[151] R. M. Lutchyn, T. D. Stanescu, and S. D. Sarma, "Search for majorana fermions in multiband semiconducting nanowires," *Physical Review Letters*, vol. 106, no. 12, p. 127001, 2011. 138

[152] S. Takei, B. M. Fregoso, H.-Y. Hui, A. M. Lobos, and S. Das Sarma, "Soft superconducting gap in semiconductor majorana nanowires," *Phys. Rev. Lett.*, vol. 110, p. 186803, Apr 2013. 138